Protoplanetary Disks in Multiple Star Systems

Dissertation Advisor: Dr. Sean M. Andrews Robert J. Harris

Protoplanetary Disks in Multiple Star Systems

Abstract

Most stars are born in multiple systems, so the presence of a stellar companion may commonly influence planet formation. Theory indicates that companions may inhibit planet formation in two ways. First, dynamical interactions can tidally truncate circumstellar disks. Truncation reduces disk lifetimes and masses, leaving less time and material for planet formation. Second, these interactions might reduce grain-coagulation efficiency, slowing planet formation in its earliest stages.

I present three observational studies investigating these issues. First is a spatially resolved Submillimeter Array (SMA) census of disks in young multiple systems in the Taurus-Auriga star-forming region to study their bulk properties. With this survey, I confirmed that disk lifetimes are preferentially decreased in multiples: single stars have detectable millimeter-wave continuum emission twice as often as components of multiples. I also verified that millimeter luminosity ($\propto$ disk mass) declines with decreasing stellar separation. Furthermore, by measuring resolved-disk radii, I quantitatively tested tidal-truncation theories: results were mixed, with a few disks much larger than expected.

I then switch focus to the grain-growth properties of disks in multiple star systems. By combining SMA, Combined Array for Research in Millimeter Astronomy (CARMA), and Jansky Very Large Array (VLA) observations of the circumbinary disk in the UZ Tau quadruple system, I detected radial variations in the grain-size distribution: large

particles preferentially inhabit the inner disk. Detections of these theoretically predicted variations have been rare. I related this to models of grain coagulation in gas disks and find that our results are consistent with growth limited by radial drift.

I then present a study of grain growth in the disks of the AS 205 and UX Tau multiple systems. By combining SMA, Atacama Large Millimeter/submillimeter Array (ALMA), and VLA observations, I detected radial variations of the grain-size distribution in the AS 205 A disk, but not in the UX Tau A disk. I find that some combination of radial drift and fragmentation limits growth in the AS 205 A disk.

In the final chapter, I summarize my findings that, while multiplicity clearly influences bulk disk properties, it does not obviously inhibit grain growth. Other investigations are suggested.

Contents

List of Figures

List of Tables

First and foremost, I warmly thank my advisor, Sean Andrews, for all the help and advice he has given me over the last three years. He has helped me at literally every stage of the process, from proposal writing, to data interpretation, and, finally, to the composition of this thesis, and for all those things I literally cannot thank him enough.

As part of my thesis work, I spent three months in Socorro, NM, for a residency program with the Expanded Very Large Array, as part of the Disks@EVLA project. I gained valuable experience through my work there with Claire Chandler, whom I thank for guiding me through the intricacies of EVLA data.

Finally, I would like to thank the members of my defense committee – Sean Andrews, John Carpenter, Alyssa Goodman, Matt Holman, Jim Moran, Willie Torres, and David Wilner – for taking their time to read through this thesis, with particular thanks to those who served on my advisory committee: David, Jim, Matt, Sean, and Willie.

I would also like to thank Jim Moran, for teaching me the theory of radio interferometry in the classroom, and Lincoln Greenhill with whom I worked on a previous project, for teaching me the practice of radio interferometry. Thanks to him, I now know all the ways the relation in Equation 1.5 can break down.

The department would absolutely fall apart without the tireless efforts of Peg Herlihy, Robb Scholten, Donna Adams, Jean Collins, Carolann Barrett, and Muriel Hodges to maintain order over their respective charges. I would like to thank them for all they do for this department and the RG division.

The last six years here have been a mix of fairly high highs and fairly low lows. I have been very lucky to have good friends here among the graduate students to support me through everything. I especially thank Zach Berta, Nick Stone, Diego Muñoz, Greg

Snyder, Paul Torrey, Chris Hayward, Wen-fai Fong, Gurtina Besla, Laura Blecha, and Sarah Ballard. I particularly thank Zach and his wife Jessie for keeping me sane while I was in Socorro and for many trips with me to dollar oyster bars. I also thank Katherine Rosenfeld for providing some of the tools invaluable to this thesis.

My staying in Cambridge for graduate school ensured that I kept in touch with my old friends from the Institvte down the road. I would like to thank, in particular, Gabe Durazo for being an awesome roommate and friend, Nat Twarog and Nori Pritchard for enduring my taunts about Kansas basketball, and Dennis Wei for being my signal processing go-to guy. I would also like to thank my law-talking friend Jonathan Ursprung for asking me to do his horoscope **every single time I see him**.

My teachers from high school also deserve high praise and a good deal of credit getting me where I am today. In particular, I would like to thank John Woolley, Wanda Kuester, Becky Mann, Vicki Thorpe, Tony Miller, Tricia Gardner, and Jan Young. Each one encouraged me, taught me, and endured me during class, over four years, and they all pushed me to start on the path I am on now by heading to MIT. I do not know where I would be today without them, but I'm guessing much worse off.

Finally, I would like to thank my parents, Norris and Betty Harris, for their continued love and support throughout not only these last six years, but through the last twenty-eight. They tried to give me a sense of the value of education from an early age (somehow, my dad making twelve year old me dig a ditch for what seemed like hours was part of this), and they committed countless hours to making sure that I was prepared for anything. I cannot imagine better parents.

For my parents, who made me love learning, and for my grandfather, who loved it too.

Chapter 1

Introduction

Observations of nearby field stars have convincingly demonstrated two facts. First, most stars are components of multiple systems (Abt & Levy 1976; Duquennoy & Mayor 1991; Fischer & Marcy 1992; Raghavan et al. 2010). Second, isolated stars in the solar mass range commonly host planets (Borucki et al. 2011; Mayor et al. 2011; Batalha et al. 2013). Unfortunately, less is understood about the intersection of these two scenarios: planets in multiple stellar systems. While there is a growing census of that population (e.g. Eggenberger et al. 2007; Mugrauer & Neuhäuser 2009; Duchêne 2010; Roell et al. 2012), the frequency of planets in binaries or multiple systems of higher order remains uncertain. Most planet-finding surveys search for radial velocity variations of stars to detect planetary companions. They have selected against known multiples, since any planetary signature would be diluted significantly by the presence of the more massive stellar companion. There is hope that this selection effect will be reduced by the *Kepler* mission. The sample of stars that were surveyed by *Kepler* includes many binaries, both eclipsing and not. It may yet deliver a less biased view of planets in multiple stellar

systems (e.g., Kepler 16, 34, and 35; Doyle et al. 2011; Welsh et al. 2012).

There are other reasons to be interested in the formation of planets in these systems, aside from the high frequency of multiples. Despite the dynamical hazards inherent to that environment, the evidence suggests that planets in multiples are roughly as common as planets around single stars, at least for systems with stellar separations greater than about 40 AU (Roell et al. 2012). Furthermore, there is some evidence for a correlation between planet mass and host binary separation (Duchêne 2010; Roell et al. 2012). An explanation for these trends can be found by studying the material used to make these systems: the cool, dusty gas disks left behind after stars form.

While the details of the process that converts disk material into planets remain unclear, astronomers have offered two constraints: (1) the disk at its inception must have enough mass to form planetary systems like those we observe; and (2) the disk lifetimes must be long enough for the processes that convert disk material into planetary systems to operate. These requirements suggest that planet formation in a multiple star environment should be harder than in an isolated environment. Tidal forces should strip material away from the disks, leaving systematically less circumstellar material in a multiple system than around an isolated star (e.g., Artymowicz & Lubow 1994). Furthermore, with less mass, the disk empties sooner, so planets have less time to form.

Despite recent progress in characterizing the masses and lifetimes of circumstellar disks (Strom et al. 1989; Carpenter et al. 2005; Andrews & Williams 2005, 2007a; Cieza et al. 2009; Kraus et al. 2012), the detailed interplay between dust and gas in these disks is only beginning to be understood. The conversion of disk material into planetary systems is intimately linked to the evolution and growth of disk solids

(dust grains). Theoretical work has suggested that the presence of a stellar companion should be disruptive to this process (e.g., Zsom et al. 2011), though this is essentially unconstrained by observations at the moment.

This thesis presents observational studies that employ the techniques of (sub)millimeter and radio interferometry to learn about the role multiplicity plays in both the determination of bulk disk properties (like masses and lifetimes), and the detailed progress of grain growth to $\sim$ cm sizes. In this introductory Chapter, we first provide a basic summary of the current understanding of star and planet formation in an isolated environment (§1.1). We then present the previous theoretical and observational work that has been done on the impact of stellar companions on these disks, as well as complementary results from planet-finding surveys (§1.2). We then detail some of the theoretical problems with the theory of grain growth in an isolated disk and comment on how they may be solved and how multiplicity may play a role in determining grain evolution (§1.3). We go on to motivate and explain the observational techniques used in this thesis (§1.4). We finally conclude with a summary of the following chapters (§1.5).

1.1 Isolated Star Formation and Circumstellar Disks

Planetary systems are the by-product of circumstellar material left behind after the host star formed. This basic idea has old roots. Kant and Laplace initially theorized that the Sun and Solar System descended from a primordial rotating, collapsing gas cloud. The bulk of the cloud, they thought, formed the star, and the remainder, flattened into a disk, formed the planets. While this model is simplistic, it nonetheless survives in the now-standard theory for isolated star formation. To understand planet formation, we

must consider star formation first.

1.1.1 Isolated star formation

Stars form in clouds of molecular gas and dust. These clouds have been observed for a century as dark patches on an otherwise uniform field of (background) stars or as whispy nebulae (Barnard 1895). The most impressive of these clouds were named after the constellations around them, e.g. the *Taurus-Auriga* cloud, the *Ophiuchus* cloud, and *Orion*. Many of the stars coincident with these regions were known to have peculiar properties, such as large brightness variations and odd spectral features, as long ago as the 1800s (e.g., Knott 1891). They received little attention until the 1940s, when Alfred Joy classified a collection of stars in the Taurus-Auriga region as having peculiar spectra, brightness variations, and strong Hα emission lines, in common with the star T Tauri (Joy & van Biesbroeck 1944; Joy 1945). They were termed *T Tauri stars*. Their common associatation with O-type stars, known even then to live only $\sim$ 10 Myr, proved that these stars were young (Herbig 1950, 1957; Ambartsumian 1957).

Optical and infrared observations in the ensuing decades proved that these stars were unlike their older counterparts. Intense Hα emission – an indicator of accretion – was observed in many cases (Herbig 1962), whereas others had much fainter Hα emission (Herbig & Bell 1988). The former were termed *classical* T Tauri stars and the latter *weak-lined* T Tauri stars. The advent of sensitive infrared detectors in the 1960s through 1980s revolutionized the study of these objects. Mendoza (1966) first showed that the infrared emission from T Tauri stars often far exceeded that expected from their photospheres. Mendoza (1968) proposed that circumstellar dust heated by star

light was responsible for this *infrared excess*. Subsequent ground-based observations in the mid-infrared (Cohen 1974; Cohen & Kuhi 1979) and spaced-based observations in the far-infrared with the *Infrared Astronomy Satellite* (IRAS) supported this view (Lada & Wilking 1984; Rucinski 1985). It was soon realized that the shape and overall similarity of the infrared spectra constrained the geometry of the emitting material to be a flattened disk (Rucinski 1985; Beall 1987; Kenyon & Hartmann 1987; Adams et al. 1988; Beckwith et al. 1990). A cartoon illustrating the interpretation of the emission is shown in Figure 1.1. At the same time, other near and mid-infrared surveys uncovered an optically invisible population of objects associated with the same dark clouds inhabited by T Tauri stars (Grasdalen et al. 1973; Vrba et al. 1975; Elias 1978; Lada & Wilking 1984).

Lada & Wilking (1984) first constructed a classification scheme for the objects associated with regions of active star formation. They divided them into three classes based on the slope of the *spectral energy distribution* (SED) within the infrared bands,

$$\alpha = \frac{d \log \lambda F_\lambda}{d \log \lambda}. \tag{1.1}$$

This classification was subsequently refined and extended to a fourth spectral class by Greene et al. (1994). This remains the standard classification scheme for the *young stellar objects* that are found in these regions:

Class I sources have $\alpha \gtrsim 0.3$;

Flat Spectrum sources have α between -0.3 and 0.3;

Class II sources have α between -0.3 and -1.6; and,

Class III sources have $\alpha \lesssim -1.6$.

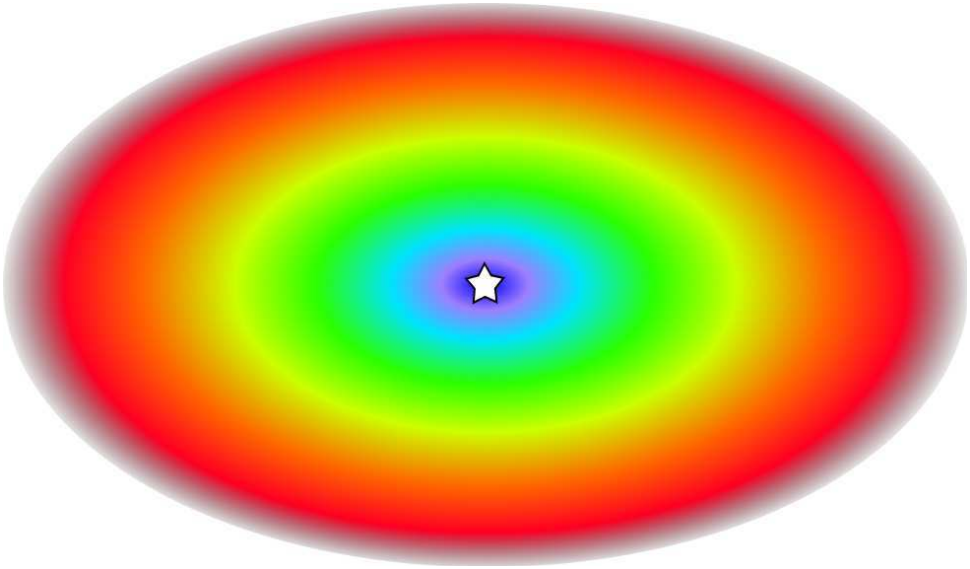

Figure 1.1: A cartoon illustration of a young disk-bearing star. The colors represent the wavelengths at which the local dust preferentially emits. Dust near the star is hot, so it emits in the near-infrared, represented here as blue. As distance to the star increases, the dust becomes cooler, so the emission peaks at longer wavelengths, represented here as a gradual reddening of the emission.

The value of -1.6 is chosen because it is close to the infrared spectral index of a stellar photosphere, indicating little contribution from dusty material surrounding the star.

The theoretical unification of the optical and infrared observations came with the review by Shu et al. (1987). In this view, the classification schemes of Lada & Wilking (1984) and Greene et al. (1994) reflect the evolution of circumstellar material. Within large clouds of molecular gas and dust, individual clumps of overdense rotating gas become gravitationally unstable and start to collapse; the initial rotation is due to random turbulent motions in the gas. After sufficient infall, the temperatures, densities, and pressures in the central regions of the clump have climbed high enough for nuclear

reactions to begin, and a star is born. At this early stage, the star is completely enshrouded by a natal envelope that is dusty enough to prevent detection at visual wavelengths. Because of the presence of rotation, the material does not accrete directly onto the star. Absent an efficient way to shed angular momentum, the infalling material will approach the center, but miss it by an amount determined by the angular momentum of the gas. This leads to the formation of a *circumstellar disk* from the infalling material. At this stage, these star+disk+envelope systems are the *Class I* sources.

After the material from the envelope has totally drained into the star+disk system, the disk alone remains as a reminder of the birth of the star. These *Class II* sources are the progenitors of planetary systems. The *Flat Spectrum* sources are thought to represent either a transition between the Class I and Class II stage or Class II sources viewed nearly edge-on (e.g., Beck 2007).

The disks of Class II systems evolve, accrete onto the star, and dissipate through the action of disk viscosity, potentially aided by dynamical clearing caused by planet formation. After disk dispersal, we are left with the final stage of young star evolution, that corresponding to *Class III* sources.

The evolution of disks through the Class II phase has become the subject of considerable research, principally because it is now evident that these disks are broadly similar to the early Solar System. The first direct evidence of stars hosting dusty disks with Solar System size-scales came from spatially resolved observations of HL Tau and R Mon (Beckwith et al. 1984; Grasdalen et al. 1984). Evidence for the gas content of the disks came later. While most of the gas content of the Solar System is locked up in molecular hydrogen, the emission from H_2 at the temperatures obtained

in disks is practically non-existent, due to the lack of a permanent dipole moment. So, despite CO being much less common than H_2, interferometric observations of 115 GHz $^{12}CO(J = 1 - 0)$ line emission from both stars (Beckwith et al. 1986) proved that these disks hosted gas. The detection of Keplerian rotation of the gas proved that disks orbit their host stars (for GM Aurigae; Koerner et al. 1993).

1.1.2 Planet formation in an isolated environment

The gas and dust in these disks must somehow get converted into planets. The details of this conversion are still unresolved, but the currently preferred picture starts with the growth of disk solids from sizes of $\lesssim 1\mu$m to $\gtrsim 1000$ km. During the Class I phase, the disk is populated with sub-micron sized grains (Beckwith & Sargent 1991; Bianchi et al. 2003; Kessler-Silacci et al. 2005). Once these particles inhabit the dense disk environment, solids grow through hit-and-stick collisions (e.g., Dominik & Tielens 1997, and references therein). The relative velocities that are required for collisions – and growth – of these solids are generated by the interactions of the dust with the gas. Small dust particles acquire relative velocities through Brownian motion (Weidenschilling & Cuzzi 1993). As they collide, they grow from simple monomers into larger, highly porous structures (e.g., Wurm & Blum 1998). Their growth in size causes them to sediment from the disk atmosphere into the midplane, where they continue to grow through similar collisions (D'Alessio et al. 2006). Growth progresses in this fashion until particles reach a disk-radius dependent sizes (~ 1 m at 1 AU), at which point relative velocities become so high as to shatter these rocks into smaller grains (Brauer et al. 2008a). If any manage to survive this fragmentation, some other process, currently unknown, then grows them

until they reach $\sim$ km sizes. At that size, gravity dominates, and mutual gravitational interactions grow them into "cores" of $\sim$ a few Earth masses. At this point, if gas is still in the disk, these cores accrete it to form giant planets. If the disk is gas-depleted, the cores are terrestrial planets.

There is a hard limit to the time allotted for this formation process. Observations indicate that the disks accrete, so mass is continuously being dumped onto the star (Herbig 1962; Gullbring et al. 1998; Muzerolle et al. 1998). The accretion rate is determined by the strength of the disk viscosity and the surface density of the disk (e.g., Shakura & Sunyaev 1973). Measurements of the mass accretion rate and estimates of the disk surface density indicate that the ordinary molecular viscosity provided by the gas is insufficient to drive accretion (Pringle 1981), so other mechanisms must be invoked. The currently preferred theory employs ambient magnetic fields that thread the disk. Because the disk is thought to be partially ionized by the star and cosmic rays, the magnetic field couples with the gas, and it can drive a fluid instability that leads to turbulence (Balbus & Hawley 1991). This turbulence creates a higher effective viscosity, roughly in line with that determined from observations (e.g., Hughes et al. 2011; Flock et al. 2012, although see Bai 2011). The evolution of the gas, driven by this viscosity, causes the disk to spread out (Shakura & Sunyaev 1973) and dissipate on a timescale of $\sim$ 1 - 10 Myr (Strom et al. 1989; Mamajek et al. 2004; Carpenter et al. 2005). It is in this time-sensitive environment that growth of disk solids over 14 orders of magnitude in radius (from sub-micron to planetary sizes) must happen. The initial steps of planet formation, growth to $\sim$ cm sizes, are among the most interesting, as the particles growing to these sizes are among the most impacted by the presence of the gas.

In the process of grain growth, the gas-dust coupling is crucial, since it can both

promote (Johansen et al. 2006; Pinilla et al. 2012a,b; Dittrich et al. 2013) and inhibit (Whipple 1972; Okuzumi 2009; Zsom et al. 2010) planetesimal growth. The coupling strength depends on the dust size: small particles (e.g., sub-micron sizes) couple almost perfectly with the gas, leading to a dust distribution for small particles that mirrors the gas distribution. Larger particles less effectively trace the gas. Thermal pressure gives the disk thickness according to its balance with local gravity, while disk turbulence acts to keep the particles stirred and differentially settled. Consequently, small particles populate the disk atmosphere above the midplane, while large particles preferentially lie in the midplane (Weidenschilling 1980; Mizuno et al. 1988). This concentration of large particles can promote planetesimal growth through enhanced collision rates. This stratification has been observed in a few systems (Duchêne et al. 2003b, 2010; McCabe et al. 2011). While the gas-dust interaction can promote grain growth, it also poses several barriers to growth that will be discussed in §1.3.

Environmental effects can modify this process. The effects of the radiation field of both the host star (Clarke et al. 2001) and the external environment (e.g., Mann & Williams 2010) in the determination of disk masses has been noted before. Another key environmental factor that has not been typically included in studies of planet formation is the presence of a close stellar companion. This may be a key oversight, as most stars are born with at least one companion. Whether or not a stellar companion changes the overall picture of planet formation as described here or not is unclear, and it is the subject of this thesis.

1.2 Stellar Multiplicity and Disks

Stellar multiples are common. It is estimated that approximately 50% of field stars with spectral types ranging from G to M (i.e., solar analogues and stars of lower mass) have companions (Abt & Levy 1976; Duquennoy & Mayor 1991; Fischer & Marcy 1992; Raghavan et al. 2010). This fraction is even higher in young star forming regions like Taurus and Ophiuchus ($\gtrsim 80\%$; Simon et al. 1992; Ghez et al. 1993; Leinert et al. 1993; Kraus et al. 2011). Field star binaries have a projected separation (a_p) distribution that peaks at $a_p \sim 30$ - 50 AU (Raghavan et al. 2010). Because the typical circumstellar disk around an isolated star has an extent of ~ 100 AU (e.g., Kitamura et al. 2002; Andrews et al. 2009, 2010), stellar companions should have dramatic effects on circumstellar disks. However, the exact details of how this interaction occurs and what effects it has have remained both theoretically and observationally unclear.

1.2.1 Summary of disk-companion interaction theory

Theory indicates that the structure of disks around stars should be affected by the presence of a body in orbit around the star (e.g., Papaloizou & Pringle 1977; Lin & Papaloizou 1979b; Goldreich & Tremaine 1979, 1980; Artymowicz & Lubow 1994; Pichardo et al. 2005, 2008). These studies have typically focused on the effects companions have on the outer radius of circumstellar disks or planetary rings, and they agree that more closely orbiting companions truncate a disk closer to its host star than a more widely separated companion. We show the basic geometry of two stars, both bearing disks, orbiting each other in Figure 1.2. The orbit of two bodies in three-dimensional space is completely specified by 6 parameters. Five of these describe

the relative orbit of the two bodies: the semi-major axis a, eccentricity e, orbital plane inclination i, and two angles that describe the orientation of the elliptical orbit in space, the longitude of periastron ω and the longitude of the ascending node Ω. The sixth parameter that completes the specification of the absolute orbit is the mass ratio $q = M_2/M_1$, where the companion mass is M_2 and the primary mass is M_1. In principle, the response of the disk orbiting the mass M_1 to the perturbation of the companion of mass M_2 can be expressed in terms of any combination of the set $\{a, e, i, \omega, \Omega, q\}$.

The first analytical studies of disks in binary systems came in the 1970s. Many of these early works were restricted to systems with circular orbits and low q (e.g., the interaction of a star+disk system with a planetary body, or the interaction of the rings of Saturn with one of the Saturnian moons). These first studies (e.g., Papaloizou & Pringle 1977; Lin & Papaloizou 1979b) examined analytically the process of angular momentum exchange between the binary and the disk. Papaloizou & Pringle (1977) were the first to analytically incorporate viscous forces, as well as energy and entropy flow into the disk. They studied a satellite in a circular orbit around a central, disk-bearing object, with the disk co-planar with respect to the binary orbit. By directly evaluating the rate of dissipation of angular momentum in the disk, they computed that tidal interactions would remove disk material down to an equilibrium outer disk radius of $\sim a/3$.

Lin & Papaloizou (1979b) first suggested that the location of orbital resonances may be relevant to the disk response. These resonance locations are places in the disk where the orbital frequency of the material around its host star is commensurable with the orbital frequency of the companion. Lin & Papaloizou focused on low mass ratio systems with circular orbits and showed that the disk is strongly truncated at the site of the 2:1 resonance. Goldreich & Tremaine (1979, 1980) extended this work by suggesting

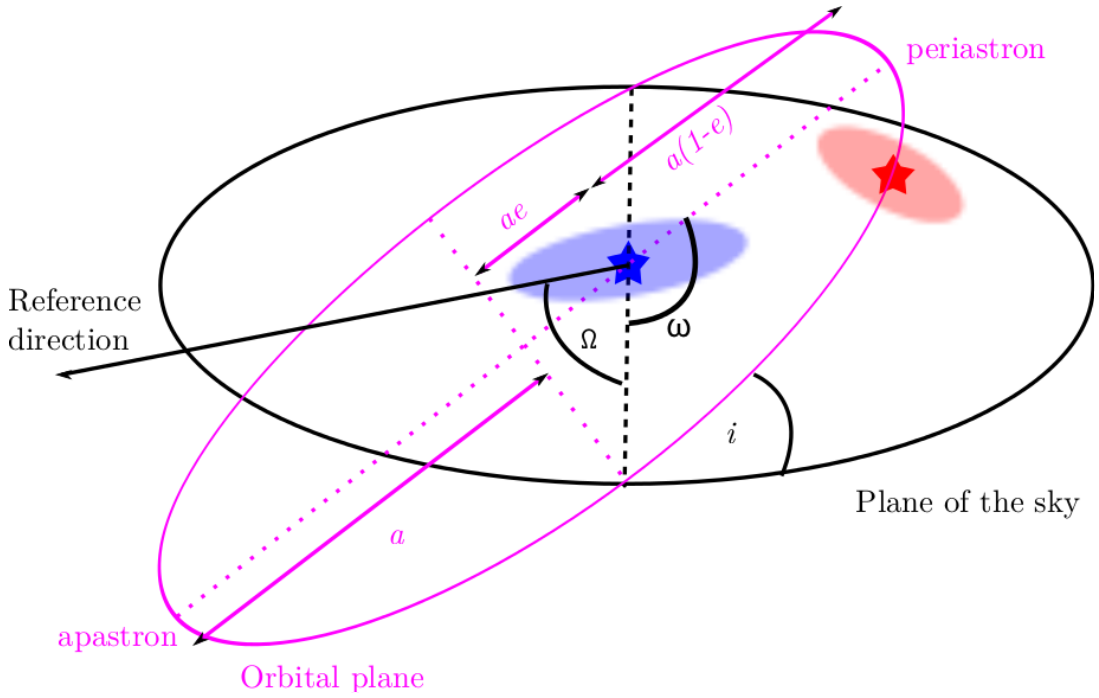

Figure 1.2: The geometry of two disk-bearing stars orbiting each other. The orbit has semi-major axis a and eccentricity e. The inclination of the orbit with respect to the tangent plane of the sky, i, is shown, as are the longitude of periastron ω and the longitude of the ascending node Ω. The primary and its associated disk are shown in blue, while the secondary and its disk are shown in red. We have made the assumption that q is small, so one focus of the ellipse is coincident with the primary. Note that the disks need not be coplanar with each other, or with the plane of the binary orbit.

that resonances may play a key role in determining the effect of satellites on disks, deriving a formula for the torque applied at these resonance locations within the disk, and, for the first time, accounting for the effects of a low, but finite, orbital eccentricity. In particular, they suggested that satellites excite density waves at the sites of Lindblad and co-orbital resonances in the disk. These density waves, once dissipated, deposit angular momentum into the disk, dispersing the disk where the waves dampen. They assumed that the dissipation was strong and local. Because of this, the disk would be truncated at the location, $R_{\rm tidal}$, of the innermost resonance at which the resonant torque delivered to the disk by the companion is greater than or equal to the viscous torque produced by the natural spreading of the disk via viscosity. This radius then depends on a, e, the disk viscosity, and weakly on q. Artymowicz & Lubow (1994) generalized this work by by allowing for both arbitrary q and e. They also included for the first time numerical simulations using smoothed particle hydrodynamics that followed the evolution of *both* circumprimary *and* circumsecondary disks in a binary system, as well as that of a circumbinary disk. Their numerical simulations explicitly demonstrated that all these disks would be truncated at radii consistent with their analytical calculations. In particular, they showed that the truncation principally depends on a and e, with only a weak dependence on q. Further studies employing complementary methods (e.g., Pichardo et al. 2005, 2008) have found results consistent with the previous studies. Despite the fact that wide binaries can have disks with high mutual inclinations (Jensen et al. 2004) the effects of the mutual inclination between the orbital plane and the disk have not been extensively considered (although see, e.g., Xiang-Gruess & Papaloizou 2013).

The results of the theoretical work on star-disk interactions can be summarized by

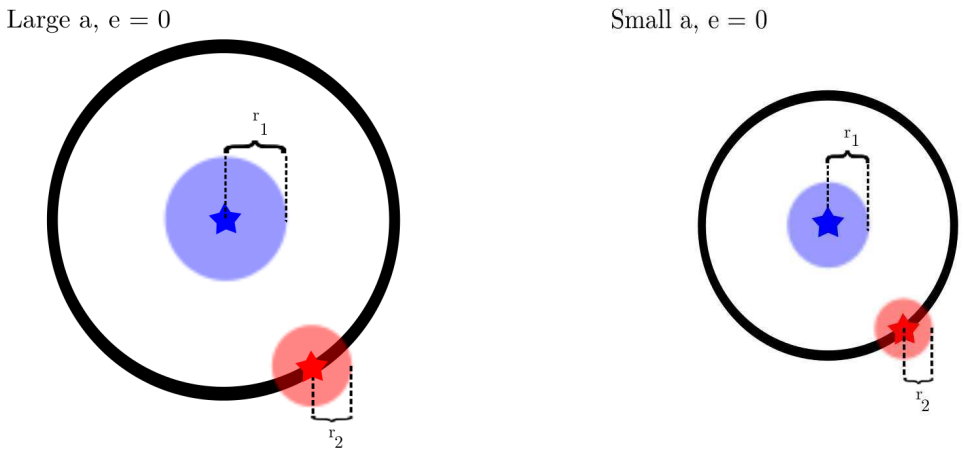

Figure 1.3: (*Left*): Face-on view of the orbit of two stars with disks with a large semi-major axis and $e = 0$. *(Right)*: The same stars with $e = 0$ but a smaller semi-major axis. Note the stronger outward truncation of both circumstellar disks.

two seemingly obvious statements: (1) more massive companions truncate disks more efficiently than less massive ones, and (2) close orbits truncate disks more efficiently than wide ones. The last statement can be interpreted as a statement about either a or e: given e, if a is lowered, disks will be more strongly truncated, while if a is fixed and e is raised, disks will be more strongly truncated. This is summarized in Figures 1.3 and 1.4.

Dynamical studies have proven invaluable, in particular for highlighting the importance of disk-satellite interactions in determining the evolution of protoplanets within their natal disks. The theory of how planets may migrate in their disks, leading to the current locations of the gas and ice giants in the Solar System, ultimately derives from the theoretical developments mentioned above (Ward 1986; Tanaka et al. 2002). Migration should play a key role in determining the architecture of planetary systems, so understanding disk-satellite interactions is crucial for understanding the assembly of planetary systems. Observations of the disks in young multiple systems,

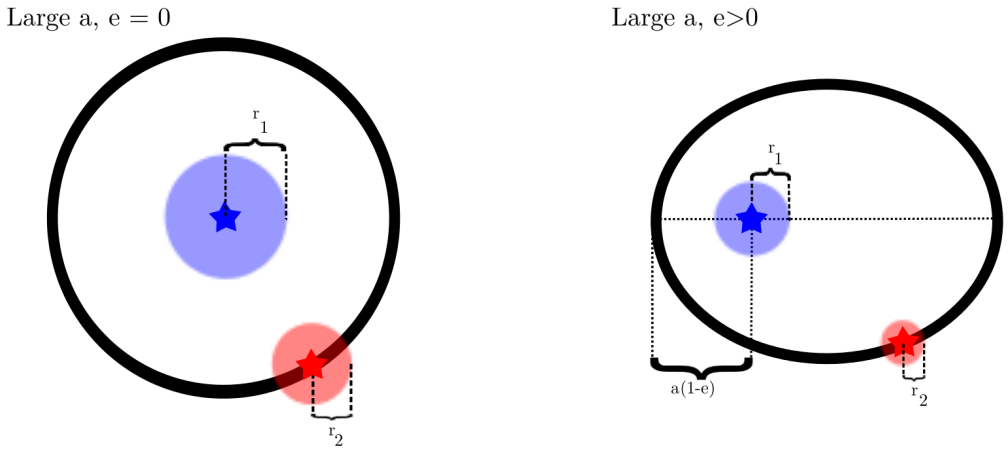

Figure 1.4: (*Left*): Face-on view of the orbit of two stars with disks with a large semi-major axis and $e = 0$. *(Right)*: The same stars orbiting with the same semi-major axis but a larger eccentricity. The truncation can be viewed as stronger either because (a) the periastron passage is closer or because (b) eccentric Lindblad resonances in the disk, lying closer to the star than the corresponding non-eccentric ones, are excited by the orbit.

both circumstellar and circumbinary, provide a first glimpse into these interactions in the high-mass ratio regime.

1.2.2 Observations of disks in young multiple systems

Observationally, the connection between disks and their companions was appreciated early on. The initial millimeter-wave continuum surveys showed evidence that bright emission was less likely to be seen in Taurus systems known to have stellar companions with projected separation a_p closer than about $\sim$ 100 AU (e.g., Beckwith et al. 1990; Osterloh & Beckwith 1995). Jensen et al. (1994, 1996b) presented the first robust evidence for a general separation / (sub)millimeter luminosity correlation by combining

new 800 μm observations of systems in Taurus and Scorpius-Ophiuchus with previous 1.3 mm surveys (from Beckwith et al. 1990; Osterloh & Beckwith 1995; Andre & Montmerle 1994). In particular, they found that systems with $a_p \lesssim 50 - 100$ AU were systematically underluminous in the submillimeter as compared to systems with companions at $a_p \gtrsim$ 50 - 100 AU. Jensen et al. (1994) considered two possible explanations for this trend. First, a close companion could cause a reduction in the disk surface density *at all radii* for close binaries, as compared to either wide binaries or their isolated counterparts, due to some unknown effect that occurs during binary star formation. The second possibility was dynamical clearing by the companion. Jensen et al. (1996b) concluded, based on an improved sample and supporting *IRAS* 60 μm observations that provided a normalization on the surface density of the disk at $\sim$ 10 AU, that dynamical clearing of material in the outer disk by the presence of a companion was the more likely scenario. Subsequent photometry by Andrews & Williams (2005) supported this conclusion.

Infrared work has largely supported the view that companions have a detrimental effect on the circumstellar material in multiple systems. Observations by Jensen & Mathieu (1997) of a handful of Class II spectroscopic binaries showed that many of them have a mid- or far-infrared excess, but no near-infrared excess. The most natural interpretation is that these systems have circumbinary disks with central regions cleared by the dynamical interaction between the central binary and the surrounding disk material. Furthermore, while early infrared observations (Mathieu 1994; Simon et al. 1995; Simon & Prato 1995) showed an overall similarity in the infrared detection rates of *inner* disks in multiples as compared to their isolated counterparts, subsequent work with improved samples has shown this to be spurious. In particular, Cieza et al. (2009) observed a large sample of young multiples with the *Spitzer Space Telescope*. They found

that multiples with a *Spitzer* excess were systematically more widely separated than those without such an excess, suggesting the relative importance of a in determining infrared disk signatures. Furthermore, Kraus et al. (2012) analyzed the infrared excesses of both single and multiple stars in star forming regions of various ages and found that the presence of a stellar companion at close ($\lesssim$ 40 AU) separations caused a dramatic decline in the lifetime of the inner disk.

While most observations have not had the requisite resolution to study the *component-resolved* properties of disks in multiple systems, there are a few exceptions. White & Ghez (2001) conducted the first large scale study of multiple systems known to host at least one classical T Tauri star in Taurus-Auriga with the *Hubble Space Telescope*, substantially increasing the number of multiples that had been resolved at visual and infrared wavelengths. They found the first significant evidence that disk properties vary depending on which component of the system the disk orbits. Although most of the stars in their sample have both inner circumprimary and circumsecondary disks, of the systems that only bore one disk, circumprimary disks were much more common than circumsecondary disks. This suggests that circumsecondary disks are shorter-lived than circumprimary ones. Millimeter-wave interferometric observations of small samples of multiples by Jensen & Akeson (2003) and Patience et al. (2008) found evidence of this trend in the continuum emission: circumprimary disks tend to dominate the emission budget. Broadly consistent results have been found in the accretion signatures of binaries in the Chamaeleon (Daemgen et al. 2013) and Orion (Daemgen et al. 2012) star forming regions; accretion signatures are typically absent or much weaker for secondaries in these systems.

1.2.3 The planet view

Observations of the incidence and properties of planets in multiple star systems give us clues about their formation. Despite the systematic de-selection of (known) multiples from radial velocity surveys, there are quite a number of planets known in multiple systems, typically because the stellar companion to the planet host star was discovered after the planet. Searches of known multiples for planets have basically only just begun (e.g., Mugrauer & Neuhäuser 2009; Eggenberger et al. 2007). Mugrauer & Neuhäuser (2009),za Duchêne (2010), and Roell et al. (2012) have compiled the census of planets in multiple systems. In their review, Roell et al. listed (then-known) planets in multiples with S-type (i.e., circumstellar) orbits. They confirmed a trend first suggested by Duchêne that there is a dependence of the minimum mass of the planetary companion in the system and the projected physical separation of the *stellar* components: closer stellar orbits were correlated with higher minimum planet masses. Duchêne had suggested that this trend could be due to a separation-dependent planet formation mechanism, although it may be due purely to the tendency of a companion in a closer orbit to preferentially strip away lower mass bodies.

Other clues about the formation of planets in multiple systems include the facts that no planet has been found orbiting a single component of a stellar pairing with a stellar separation of less than 10 AU, and that multiple planet systems have, to date, only been found in more widely-separated ($\gtrsim$ 100 AU) stellar multiples (Roell et al. 2012). Whether these statements about planets tell us more about the disks that formed them or about the dynamics of these systems after planet formation had already occurred is unclear. One final potential clue about planet formation in multiples may lie in where

they are found in these systems. More than 90 % of the known planets in binaries in S-type orbits are found around the primary (Roell et al. 2012). Whether or not this is merely a selection effect is unknown.

1.3 Grain Growth and Transport

Dust grains in protoplanetary disks are the progenitors of planetesimals, the building blocks of terrestrial planets and the cores of gas and ice giants. At the beginning of the star formation process, the dust grains should resemble those of the interstellar medium: relatively unevolved, with a maximium size of about 1 μm (Mathis et al. 1977). However, during the process of star and planet formation, the dust grains grow in size through collisions (Weidenschilling & Cuzzi 1993). The collisions are typically thought to build dust from single monomers of silicates, ices, and carbon into large, fluffy aggregates with complicated geometries (Dominik & Tielens 1997). The aggregates are then compacted by further collisions, due to their decreased structural integrity (Dominik & Tielens 1997; Paszun & Dominik 2009).

While this picture of planetesimal formation in a disk is intuitive, it was appreciated very early on (Safronov 1969; Whipple 1972) that the growth process must be more complicated. This is because the dust and gas "feel" different things. Gas pressure provides support for the gas against the stellar gravity, but not for the dust. So, the dust travels at the Keplerian speed while the gas orbits more slowly. The resulting headwind on the dust, while only $\sim 0.1\%$ of the Keplerian speed, is sufficient to cause the dust to lose angular momentum and spiral in towards the central star very quickly (Weidenschilling 1977). The characteristic time for a 1 meter planetesimal to inspiral to

the inner disk edge from an orbital radius of 1 AU is approximately 1 year. Furthermore, this process is roughly self-similar, so the corresponding time for a 1 mm particle at 100 AU is 10^5 years, much less than the observed lifetime of the disks. The resulting depletion of large particles from the disk represents a barrier to growth to large sizes that has been termed the *radial drift barrier*. Because the radial drift speed peaks for particles with size $\sim$ 1 m at 1 AU (1 mm at 100 AU), it is conceivable that the growth of particles while they drift towards the star could allow them to "out grow" the drift barrier. However, the migration timescale into the star is short compared to the growth timescale for particles in this size range (Brauer et al. 2008a).

Another barrier lies in the fact that growth is not the only possible outcome of collisions: the particles can also bounce off of each other without mass exchange (Zsom et al. 2010) or even fragment into smaller particles (Brauer et al. 2008a). For typical disk parameters, these barriers could inhibit growth past $\sim$ 0.5 mm to centimeter sizes.

There have been a few suggestions about how to overcome these obstacles. In particular, hydrodynamic effects that can lead to differing directions of gas flow depending on the height above the midplane (zonal flows; Urpin 1984) and their analogues in the azimuthal direction (meridional flows; Johansen et al. 2006) have been suggested as potential ways to bypass growth barriers. Furthermore, pressure effects – the same physics responsible for the radial drift barrier – can lead to particle traps within disks. There is no need for a gaseous disk to have a pressure profile monotonically declining with radius. The effects of the magneto-rotational instability (Balbus & Hawley 1991) can lead to complicated and long-lived structure in the pressure field of the disk (e.g., Johansen et al. 2009; Uribe et al. 2011). Stellar (or planetary) companions can induce "pressure bumps" that lead to large concentrations of dust particles (Pinilla et al.

2012a). These concentrations could lead to substantial and fast growth, overcoming all the barriers to growth presented by the gas (Pinilla et al. 2012a; Birnstiel et al. 2013).

Despite the uncertainty in what mechanisms permit grain growth past the nominal "centimeter barrier" in the outer disk, observations have indicated that large particles are present within ~ 1 Myr of disk formation. Serious numerical work over the last few years has helped to clarify the nature of these growth barriers. The physics of fragmentation and radial drift are not very sensitive to the details of the particles. This fact has permitted extensive investigation of these barriers in simulations of grain growth. One of the first detailed numerical studies on the subject included grain growth and fragmentation in a static disk environment (Dullemond & Dominik 2005). It was found that fragmentation was *necessary* to explain the lifetime of infrared excesses observed in T Tauri stars. When fragmentation was neglected in these models, grain growth was too quick and small particles would be rapidly exhausted from the disk, in stark contrast with observations. Subsequent efforts improved on this work by allowing for a time-dependent gas density in the disk and by permitting simultaneous tracking of the evolution of the gas *and* the dust properties (Birnstiel et al. 2010a, 2011). These studies show promise in determining how the dust-gas interaction proceeds to allow grain growth to $\gtrsim$ meter sizes. Observations of disks, particularly in the submillimeter and radio bands that trace the population of large particles most sensitive to these barriers, are needed to calibrate these models.

The importance of multiplicity in this process has only recently been suggested. Zsom et al. (2011) used numerical simulations following both the gas and dust to show that the extent of grain growth in close binaries may be suppressed by as much as an order of magnitude in grain size. Observationally, this is only beginning to be

investigated. Pascucci et al. (2008) have shown that grain growth to ~ 10 μm sizes in disks is not impeded by a stellar companion. However, there has been no study of the progress of grain growth to $\sim$ cm sizes in any appreciable sample of multiples.

1.4 The Roles of (Sub)millimeter and Radio Observations

Observations at long (sub)millimeter and radio wavelengths play a significant role in the study of disks for two reasons. First, these observations probe the population of large dust particles in disks. This has several important observational consequences that favor the use of submillimeter and radio observations in studying protoplanetary disks. Because small particles preferentially inhabit regions high above the midplane, infrared observations effectively probe dust in the disk *atmosphere*. So, while infrared observations are useful for assessing the *presence* of dust at different radii from the host star, they usually only inform us about the temperature of the material at the vertical location in the disk where the optical depth reaches unity, and not its density (Chiang & Goldreich 1997). On the other hand, observations at longer wavelengths, in the submillimeter and radio bands, probe the larger particles inhabiting the midplane. Because these particles have much lower opacity per unit mass than the smaller particles, the emission is optically thin, so it provides an indirect measure of the total mass content of the disk through the relation of the flux density F_ν to the disk parameters, i.e.:

$$F_\nu = \int I_\nu d\Omega \propto \int B_\nu(T)(1 - e^{\tau_\nu})d\Omega \propto \kappa_\nu \nu^2 T M_{\rm disk}, \tag{1.2}$$

where κ_ν is the total (i.e., gas and dust) disk opacity, $M_{\rm disk}$ is the total disk mass, and T is the average disk temperature (e.g., Beckwith et al. 1990; Osterloh & Beckwith 1995; Andrews & Williams 2005).

Second, the spectrum of this emission traces the extent of grain growth in the disk. The absorption opacity per unit mass for radiation in the disk, κ_ν, is set by the dust. While the emission spectrum of individual dust grains depends on composition and shape, it is primarily set by the dust size distribution (e.g., Miyake & Nakagawa 1993; Draine 2006). Grains of size a radiate very inefficiently at wavelengths $\lambda \gg a$, and Rayleigh scattering causes a $\kappa_\nu \propto \lambda^{-2}$ dependence. For $\lambda \ll a$, the geometric optics limit applies, so κ_ν is roughly constant. In the intermediate regime, where $a \sim \lambda$, photon-particle interactions become complex due to resonant effects. These resonances drive κ_ν to large values, so particles of size a effectively block and emit radiation at $\lambda \sim a$. Because of the dependence of κ_ν on particle size, the shape of the (sub)millimeter/radio spectrum informs us about the particle size distribution (Beckwith & Sargent 1991; Miyake & Nakagawa 1993). Theoretical calculations of dust opacities indicate that in the submillimeter/radio bands, κ_ν is adequately described by a power law in frequency, $\kappa_\nu \propto \nu^\beta$, and that, for a given composition and shape, there is a correspondence between the maximum size of grains present and the value of β (Miyake & Nakagawa 1993; Draine 2006). So, with the same approximations used in Equation 1.2, dual frequency observations allow us to compute the shape of the opacity spectrum,

$$\frac{F_{\nu_1}}{F_{\nu_2}} = \frac{\kappa_{\nu_1}\nu_1^2}{\kappa_{\nu_2}\nu_2^2} = \left(\frac{\nu_1}{\nu_2}\right)^{2+\beta}. \tag{1.3}$$

By employing multi-frequency submillimeter and radio surveys, we can study the evolution of grains to large $\sim$ cm sizes.

The development of sensitive submillimeter instrumentation in the 1980s through 2000s has allowed large-scale disk surveys. The results of numerous submillimeter and radio surveys (Beckwith et al. 1990; Osterloh & Beckwith 1995; Andrews & Williams 2005, 2007a) indicate that the average disk of a Class II object has at least a few Jupiter masses of material and that these disks lose their submillimeter emission before an age of ~ 10 Myr. Furthermore, multi-band observations have found that the values of the β index for young T Tauri stars often lie in the range $0 \lesssim \beta \lesssim 1$ (Beckwith & Sargent 1991; Wilner et al. 2005; Andrews & Williams 2005; Ricci et al. 2010a,b, 2011a), lower than the values found for the interstellar medium ($\sim$ 1.7-2.0; Finkbeiner et al. 1999; Li & Draine 2001). This suggests that dust grains in the disks around T Tauri stars have grown significantly larger since the birth of the disk.

Finally, submillimeter and radio wavelengths are useful to study disks because they allow interferometry to be used to achieve high angular resolution. Circumstellar disks tend to have sizes on the order of ~ 100 AU (e.g., Andrews et al. 2009). Placed at the distance of the nearest regions of star formation, this physical scale corresponds to a projected radius of less than an arcsecond on the sky. Because single-dish telescopes operating at (sub)millimeter bands have a typical resolution of ~ 15 arcseconds, interferometry is required to spatially resolve disks.

In interferometry, rather than a single radio telescope receiving an astronomical signal and being limited to a resolution set by its diameter, multiple telescopes are used. Using this technique, the resulting resolution of the array of telescopes is then

$$\theta_{\rm res} \approx C\frac{\lambda}{B_{\rm max}} \approx 0.2 \cdot C \left(\frac{\lambda}{1\ {\rm mm}}\right)\left(\frac{B_{\rm max}}{1\ {\rm km}}\right)^{-1}\ {\rm arcsec} \tag{1.4}$$

where $B_{\rm max}$ is the maximum distance between any two of the antennas, λ is the observing

wavelength, and C is a constant of order unity that depends principally on the array geometry. Interferometry permits a substantial increase in the resolution achieveable at millimeter and radio bands. Each antenna receives a signal, and pairs of these signals are cross-correlated to produce a correlation coefficient that is related to the distribution of brightness on the sky. The values of the correlation coefficients, termed *visibilities*, are functions of the displacement between the pair of telescopes, $\langle u, v \rangle$, typically defined as the physical separation of the telescopes in the two cardinal directions North and East, as normalized by the observing wavelength λ. If one makes reasonable assumptions about the telescope and the emission being studied, then the relation between the sky brightness as a function of the two angular coordinates on the sky $I_\nu(x, y)$ and the visibilities $V_\nu(u, v)$ is given by a Fourier transform relation,

$$V_\nu(u, v) = \int I_\nu(x, y) \exp\left(2\pi i(ux + vy)\right) dxdy. \tag{1.5}$$

In other words, the visibilities are samples of the Fourier transform of the two-dimensional sky brightness distribution at discrete spatial frequencies given by u and v. By performing a Fourier inversion, an estimate of the sky brightness distribution $I_\nu(x, y)$ can be made. The imaging process, however, is complicated by the fact that measurements of the visibilities are only made at a finite number of discrete places in the Fourier domain. Because of this, special non-linear deconvolution techniques must be used to produce informative images.

Observations of a given source taken with different interferometers, or even with the same interferometer but at different times, often do not sample the same spatial frequencies. Because of the differences in sampling in the visibility plane, the point spread functions of different observations are different. The image constructed from a

given observation via Fourier inversion is the convolution of the point spread function with the true intensity distribution. While non-linear deconvolution techniques can mitigate some of this source of confusion, directly comparing images produced with data from different observations is still difficult. Because of this, in this thesis, while we present the images produced from our data and use them as a guide, we do not use them directly for analysis unless it is clear that the effects of sampling in the Fourier domain are negligible. When this is not the case, we directly fit the visibility data to physically motivated parametric models. We discuss this in more detail in the subsequent chapters.

1.5 This Thesis

In this thesis, we use the tools of (sub)millimeter and radio interferometry to explore the role that stellar multiplicity plays in determining the properties of circumstellar disks. The remaining chapters are organized as follows:

Chapter 2 presents an extensive, high angular resolution, high sensitivity Submillimeter Array survey of the thermal dust continuum emission from the disks in 23 young multiple star systems in the Taurus-Auriga star-forming region. Results from this survey are collated with those of previous studies to make several statements about the disks in these systems, in particular their lifetimes relative to the dust disks around isolated stars, the trends of luminosities / masses with both orbital separation and location within the system, as well as a detailed analysis of the radii inferred for several of these disks and how they compare to expectations from tidal truncation theory.

Chapter 3 presents multi-wavelength, high angular resolution and high sensitivity Submillimeter Array, Combined Array for Research in Millimeter Astronomy, and Karl G. Jansky Very Large Array observations of the thermal dust continuum emission from the disks in the UZ Tau quadruple system. These observations are used to place constraints on the radial variation of dust properties in the UZ Tau E circumbinary disk. The spatially resolved distribution of dust sizes is then compared with recent theoretical work seeking to compare the importance of various processes in the determination of the sizes of disk solids.

Chapter 4 presents multi-wavelength, high angular resolution and high sensitivity Submillimeter Array, Atacama Large Millimeter/submillimeter Array, and Karl G. Jansky Very Large Array obeservations of the thermal dust continuum emission from the disks around the stars in the AS 205 and UX Tau multiple systems. These observations are used to place constraints on the radial variation of dust properties in the disks. The spatially resolved distribution of dust sizes is then compared with recent theoretical work seeking to compare the importance of various processes in the determination of the sizes of disk solids.

Chapter 5 concludes this thesis, summarizing the key results and presenting several possible lines of further investigation.

Chapter 2

A Resolved Census of Millimeter Emission from Taurus Multiple Star Systems

This thesis chapter originally appeared in the literature as

R. J. Harris, S. M. Andrews, D. J. Wilner, & A. L. Kraus, *The Astrophysical Journal*, 751, 115, 2012

Abstract

We present a high angular resolution millimeter-wave dust continuum imaging survey of circumstellar material associated with the individual components of 23 multiple star systems in the Taurus-Auriga young cluster. Combined with previous measurements in the literature, these new data permit a comprehensive look at how the millimeter

luminosity (a rough tracer of disk mass) relates to the separation and mass of a stellar companion. Approximately one third (28-37%) of the individual stars in multiple systems have detectable millimeter emission, an incidence rate half that for single stars ($\sim$62%) which does not depend on the number of companions. There is a strong, positive correlation between the luminosity and projected separation (a_p) of a stellar pair. Wide pairs ($a_p > 300$ AU) have a similar luminosity distribution as single stars, medium pairs ($a_p \approx$ 30-300 AU) are a factor of 5 fainter, and close pairs ($a_p < 30$ AU) are $\sim$5$\times$ fainter yet (aside from a small, but notable population of bright circumbinary disks). In most cases, the emission is dominated by a disk around the primary (or a wide tertiary in hierarchical triples), but there is no clear relationship between luminosity and stellar mass ratio. A direct comparison of resolved disk sizes with predictions from tidal truncation models yields mixed results; some disks are much larger than expected given the projected distances of their companions. We suggest that the presence of a stellar companion impacts disk properties at a level comparable to the internal evolution mechanisms that operate in an isolated system, with both the multiple star formation process itself and star-disk tidal interactions likely playing important roles in the evolution of circumstellar material. From the perspective of the mass content of the disk reservoir, we expect that (giant) planet formation is inhibited around the components of close pairs or secondaries, but should be as likely as for single stars around the primaries (or wide tertiaries in hierarchical triples) in more widely-separated multiple star systems.

2.1 Introduction

Many, if not most, stars are born with close companions (Abt & Levy 1976; Duquennoy & Mayor 1991; Fischer & Marcy 1992; Raghavan et al. 2010, but see Lada 2006). Depending on their orbits, tidal interactions between individual stellar components in these multiple systems can dominate the evolution of their natal circumstellar material and potentially have drastic consequences for the planet formation process (e.g., Papaloizou & Pringle 1977; Lin & Papaloizou 1979a,b; Artymowicz & Lubow 1994). But even in these hazardous dynamical environments, many young multiples harbor long-lived circumstellar material (see Duchêne et al. 2007), and a growing number of their more mature counterparts are being identified as exoplanet hosts (e.g., Patience et al. 2002; Raghavan et al. 2006; Desidera & Barbieri 2007; Doyle et al. 2011). Given the prevalence of stellar multiplicity, an improved empirical understanding of the dynamical interplay between the stars and disks in these systems – including effects like tidal truncation, stripping, and the orbital evolution of companions – is fundamental for the development of a comprehensive model for the formation of stars and planetary systems. Moreover, constraints on these dynamical processes in multiple star systems can be used as high mass-ratio touchstones for theoretical work on analogous disk-planet interactions, particularly the creation of tidal gaps and subsequent planet migration.

A wealth of theoretical work suggests that the fate of the circumstellar material in a young multiple star system is primarily dependent on the separation (a) and mass ratio (q) of the individual components, as well as the orbital eccentricity (e) (e.g., Artymowicz & Lubow 1994). Systems with eccentric orbits have an enhanced likelihood of star-disk tidal interactions. For a given orbit, a near equal-mass companion ($q \sim 1$) should have

a more destructive impact on disk material than a low-mass companion. But in most cases, the effects of $\{e, q\}$ on the circumstellar material are secondary to the orbital separation. Systems with large separations ($a \sim$ hundreds of AU) should impart little or no dynamical effects on their circumstellar material, leaving disks around each stellar component that are similar to those around single stars. Conversely, individual disks in a small-separation ($a \sim$ a few AU or less) system will likely not survive. Instead, these systems can host a circum-multiple disk with a dynamically cleared central cavity out to a radius comparable to the stellar separation ($\sim$2-3a). However, most multiple systems both in the field and in young clusters have intermediate separations ($a \sim$ tens of AU; Mathieu et al. 2000). The disks in these systems may suffer the most dramatic effects of star-disk interactions, resulting in their external truncation at a fraction of the component separation ($\sim$0.2-0.5a), or their complete dispersal.

Qualitatively, these theoretical predictions find some observational support. Statistical analyses of warm gas and dust diagnostics (accretion signatures and/or a near-infrared excess) indicate that the presence of a companion with separation $\lesssim$40 AU may significantly hasten disk dispersal near the stars (on $\sim$1-10 AU scales; Cieza et al. 2009; Kraus et al. 2012). This diminished frequency of disk signatures for "close" multiples was first noted at (sub)millimeter wavelengths by Jensen et al. (1994), and later confirmed in surveys of increasing size and sensitivity to dust emission (Osterloh & Beckwith 1995; Jensen et al. 1996b; Andrews & Williams 2005). Since the continuum emission at such long wavelengths is primarily optically thin (e.g., Beckwith et al. 1990), the systematically lower millimeter-wave luminosities from close multiples compared to systems with wider separations or single stars were taken as compelling evidence for decreased disk masses due to tidal truncation or disruption. However, that evidence is

indirect: those observations relied on single-dish photometers that do not resolve the individual stellar components nor their disks. A quantitative investigation of the theory of star-disk interactions requires observations that can address how disk masses and sizes depend on the properties of the stellar system (particularly a and q). With the right combination of angular resolution and mass sensitivity, interferometric measurements of the optically-thin millimeter continuum emission from the dusty disks in these systems are uniquely qualified for that task. Aside from a small collection of systems (e.g., Jensen et al. 1996a; Akeson et al. 1998; Jensen & Akeson 2003; Patience et al. 2008), such data are rare.

In this Chapter, we present a Submillimeter Array (SMA) survey of the millimeter-wave continuum emission from 23 young multiple star systems in the Taurus-Auriga star formation region. These data represent the most comprehensive resolved census of cool dust emission from the disks that reside in young multiple systems to date. The motivation for the survey sample is introduced in §2.2, and the observations and data calibration are reviewed in §2.3. A simple modeling analysis of these data is conducted in §2.4, with a focus on retrieving luminosities and sizes from individual disks whenever possible. The results of this imaging survey are synthesized with other information in the literature in §2.5 to extract a statistically representative view of circumstellar material in multiple star systems. Based on that analysis, we attempt to reconcile the observations with theoretical predictions from tidal interaction models in §2.6. Finally, our key conclusions are summarized in §2.7.

2.2 The Sample

Multiplicity searches in the Taurus molecular clouds have a long history of success with a variety of techniques, ranging from straightforward direct imaging (Reipurth & Zinnecker 1993; White & Ghez 2001; Correia et al. 2006; Kraus & Hillenbrand 2009b) and radial velocity monitoring (e.g., Mathieu et al. 1997) to more specialized methods like lunar occultations (Simon et al. 1992, 1995; Richichi et al. 1999), speckle interferometry (Ghez et al. 1993; Leinert et al. 1993), and most recently aperture-mask interferometry (Kraus et al. 2011). There is now a reasonably complete census of Taurus multiple systems that have angular separations $\rho \approx 0.03$-$30''$, K-band contrast ratios of $\leq$6 magnitudes ($\leq$4 mags for the systems with the smallest separations), and primary spectral types between F0 and M4. Assuming a mean distance of 145 pc (Loinard et al. 2007; Torres et al. 2007, 2009) and a crude estimation of stellar masses (see Kraus et al. 2011), this region of multiplicity parameter-space corresponds to projected separations $a_p \approx 5$-5000 AU, stellar mass ratios $q \approx 0.1$-1.0 (well into the brown dwarf regime), and primary star masses $M_p \sim 0.2$-$2\,M_\odot$. There are currently 71 such multiple "systems" known in Taurus, consisting of 111 "pairs" of 179 individual stars. For the sake of clarity, we adopt a simple nomenclature in this Chapter such that a "system" refers to any group of associated stars and a "pair" is meant as any subset of the system that could potentially interact dynamically. A simple binary (2 stars) counts as 1 system and 1 pair. In a higher-order hierarchical multiple like UZ Tau, we consider the 4 stars UZ Tau Ea, Eb, Wa, and Wb to comprise 1 system of 3 pairs based on their relative projected separations: Ea−Eb, Wa−Wb, and Eab−Wab (i.e., this phenomenological scheme implicitly assumes that pairs like Ea−Wa are unlikely to interact directly: all such pairs are listed in §2.5).

The selection criteria for our resolved millimeter-wave imaging survey were motivated by practical observational limitations and consist of two requirements: (1) a composite system flux density of $\geq$20 mJy at 880 μm, and (2) an angular separation of $\geq$0.″3 for at least one pair in the system. The first criterion is a sensitivity restriction that would ensure that our observations could firmly detect (3-5 σ) two equivalent disks around individual stellar components with the typical expected RMS sensitivity of $\sim$2-3 mJy beam^{-1} (see §2.3). Flux density estimates for unresolved systems were compiled from the single-dish survey of Andrews & Williams (2005). If no suitable 880 μm flux density was available, the 1.3 mm measurements of Beckwith et al. (1990) or Osterloh & Beckwith (1995) were scaled up by a conservative factor of $(1.3/0.88)^2 \approx 2.2$ based on the median emission ratio at those wavelengths (Andrews & Williams 2005, 2007a). Note that for the standard optically thin and isothermal assumptions for converting luminosity into mass, this sensitivity threshold corresponds to $\sim$5 $M_\oplus$ of dust (or a total mass of $\sim$1.5 $M_{\rm Jup}$ for a 100:1 gas-to-dust mass ratio). The second criterion is a resolution restriction set by the longest available baselines of the SMA ($\sim$0.5 km) that ensures we would be able to resolve the individual stellar components of a given pair. Only systems where the angular separations of all its constituent pairs are $<$0.″3 were excluded. The resulting sample includes systems where some pair has a projected separation $a_p > 40$ AU.

Of the original 71 systems, 29 exceed the 880 μm luminosity selection threshold. Of those 29 systems, only 2 fail to meet the resolution criterion (IS Tau and DQ Tau; the latter is a spectroscopic binary). The resulting 27 systems are comprised of 52 pairs and a total of 77 individual stars. We elected not to observe 4 of those systems with the SMA (FS Tau/Haro 6-5B, XZ/HL Tau, FZ/FY Tau, and V807/GH Tau) because their wide-separation pairs were already resolved with single-dish telescopes and their

remaining pairs were too faint or too close to meet our selection criteria. The systems in our 880 μm flux- and resolution-limited sample are listed in Table 2.1.

Given the practical restrictions that were imposed in its construction, it is important to investigate the resulting sample for unintended biases. Since our selection criteria do not specifically address the stellar masses in these systems, the key potential biases could be related to the mass ratios of pairs (q), the "primary" masses (M_p; meaning the mass of the brighter component of a pair), or the total pair masses (the sum of the primary and secondary components of a pair, $M_{\rm pair} = M_p + M_s$). Figure 2.1 directly compares the cumulative distributions of q, M_p, and $M_{\rm pair}$ for the pairs included in our sample (*black*) against those that were excluded due to their low millimeter luminosities and/or small angular separations (*gray*). Note that masses were typically determined from the Baraffe et al. (1998) models by Kraus et al. (2011); complete references are provided in §2.5. A two-sided Kolmogorov-Smirnov (K-S) test confirms that our sample is not biased with respect to q or M_p, with probabilities that the sample multiples and other multiples are drawn from the same parent distributions of mass ratios or primary masses being $\sim$73% and 20%, respectively. However, the distribution of $M_{\rm pair}$ for the pairs in our sample are found to be drawn from a marginally different – and systematically *higher* – parent distribution than their counterparts that were not selected, with a K-S probability of only 2% (although it is worthwhile to keep in mind that these individual stellar mass estimates are crude).

Table 2.1. Selected Sample of Taurus Multiples

System	N_*	$N_{\rm pair}$	System	N_*	$N_{\rm pair}$
MHO 1/MHO 2	3	2	DD Tau	2	1
FQ Tau	2	1	T Tau	3	2
FS Tau/Haro 6-5B	3	2	FV Tau	4	3
DI Tau/DH Tau	4	3	UX Tau	4	4
FX Tau	2	1	DK Tau	2	1
XZ Tau/HL Tau	3	2	HK Tau	2	1
V710 Tau	3	2	GG Tau	4	3
FZ Tau/FY Tau	2	1	UZ Tau	4	3
JH 112	3	2	*V807 Tau/GH Tau*	5	4
GI Tau/GK Tau	2	1	HN Tau	2	1
IT Tau	2	1	HP Tau	4	4
HV Tau	3	2	Haro 6-37	3	2
UY Aur	2	1	CIDA-9	2	1
RW Aur	2	1			

Note. — Col. (1): System name. Italicized systems have not been re-observed with the SMA (see §2.2). Col (2): Number of stars in system. Col. (3): Number of "pairs" in system (see §2.2).

2.3 Observations and Data Reduction

The 23 multiple systems listed in Table 2.1 (not including the additional 4 systems in italics; see §2.2) were observed with the SMA interferometer (Ho et al. 2004) in a variety of observing configurations and receiver settings from 2005 to 2012, with most of the data obtained between 2010 and 2011. An observing log is provided in Table 2.2. All systems were observed in the compact (C) array configuration, with baseline lengths of 8-70 m. Additional measurements were made with the extended (E: 28-226 m baselines) or very extended (V: 68-509 m baselines) configurations for the systems that contain pairs with smaller angular separations. Some of these data were presented in previous work (Andrews & Williams 2007b; Andrews et al. 2011). All but 4 of these 23 systems were observed with the 345 GHz receivers: the pairs in the HP Tau, GI/GK Tau, MHO 1/2, and GG Tau systems that we aimed to probe have wide enough separations that they were instead observed with slightly lower resolution at 230 GHz. We made some additional observations of systems that were *not* in our sample, since they had not yet been observed at millimeter wavelengths (see §2.5).

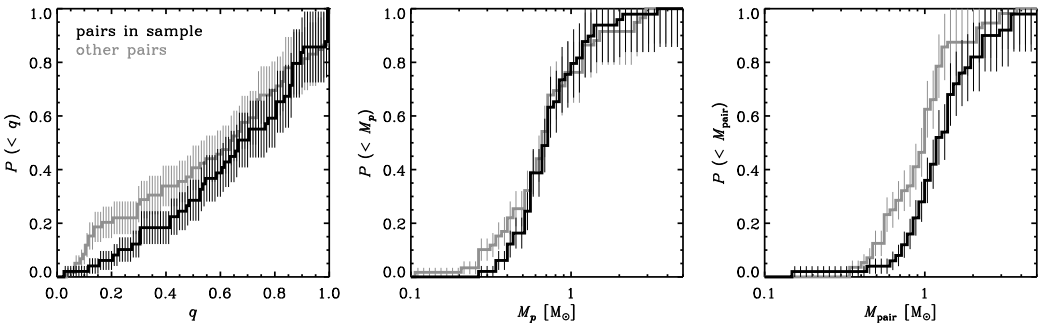

Figure 2.1: A comparison of the cumulative distributions of the stellar mass ratios (q), primary masses (M_p), and composite pair masses ($M_{\rm pair} = M_p + M_s$) between the systems that were selected (*black*) and excluded (*gray*) from our sample. While our selection criteria do not produce a significant bias in q or M_p, they tend to include pairs with marginally higher *total* stellar masses ($M_{\rm pair}$).

Table 2.2. SMA Observing Log

UT Date	Targets	Config.	ν(LO) [GHz]
2005 Dec 17	DH/DI Tau	C	340.755
2009 Oct 24	DK Tau	C	340.767
2010 Feb 11	DK Tau	V	343.277
2010 Feb 18	UZ Tau	V	341.536
2010 Feb 19	HK Tau	V	342.289
2010 Mar 2	UZ Tau	V	340.427
2010 Nov 10	IT Tau, FX Tau, HK Tau, V710 Tau, HN Tau, CIDA-9	C	340.755
2010 Nov 11	FQ Tau, IT Tau, FV Tau, HV Tau, JH 112	C	340.755
2010 Nov 12	FQ Tau, IT Tau, FV Tau, HV Tau, JH 112	C	340.755
2010 Dec 13	RW Aur, Haro 6-37, DD Tau, T Tau, UY Aur	C	340.755
2010 Dec 25	HP Tau	C	225.497
2010 Dec 27	GG Tau, GI/GK Tau, MHO 1/2	C	225.497
2011 Jan 28	FQ Tau	E	340.755
2011 Feb 3	FV Tau, FX Tau, T Tau	E	340.755
2011 Feb 17	UZ Tau, UY Aur, DD Tau	E	340.755

Table 2.2—Continued

UT Date	Targets	Config.	ν(LO) [GHz]
2011 Aug 16	DD Tau	E	341.575
2012 Jan 24	FV Tau, FX Tau, UY Aur	E	340.755
2011 Oct 13	J04080782+2807280, MHO 3	C	225.497
	J04141188+2811535, V410 X-ray 7		
2011 Oct 27	V710 Tau C, J04414565+2301580	C	222.709
	J04554757+3028077, CFHT Tau 7		

Note. — Col. (1): UT date of observations. Col. (2): Multiple systems observed. Col. (3): SMA antenna configuration (see §2.3). Col. (4): LO frequency setting. Note that the observations below the horizontal line focused on multiple systems that are *not* part of our sample: they were observed because there were no previous millimeter-wave measurements of these systems available in the literature (see §2.5.1).

In most cases, the SMA dual-sideband receivers were tuned to a local oscillator (LO) frequency of 340.755 GHz (880 μm) or 225.497 GHz (1.3 mm). Some tracks used shifted LO settings to accomodate other projects that shared one night of observing. The data obtained in 2010-2011 employs two IF bands (per sideband) spanning ±4-6 GHz and ±6-8 GHz from the LO frequency (only the lower IF band was available for the 2 observations in 2005 and 2009). Each IF band contains 24 partially overlapping 108 MHz-wide spectral chunks (per sideband). Aside from one chunk reserved for the local CO transition, each of these was coarsely divided into 32 channels to observe the continuum. A finer sampling of 256 channels per chunk was used to probe the CO emission, corresponding to a velocity resolution of 0.40 and 0.55 km s^{-1} near the J=3−2 and J=2−1 transitions, respectively. The observations cycled between various target systems and the nearby quasars 3C 111 and J0510+180 on timescales of ∼20 minutes for the compact array and 10 minutes for the longer baseline configurations. Bright quasars (3C 279 or 3C 454.3), Uranus, and satellites (Titan, Callisto) were observed as bandpass and absolute amplitude calibrators when the targets were at low elevations. Observing conditions were often excellent, with precipitable water vapor levels ranging from 1.0-1.6 mm and ∼2-3 mm for the 880 μm and 1.3 mm observations, respectively.

The data were reduced with the IDL-based `MIR` software package. The spectral response was calibrated using observations of bright quasars as references, and the central 82 MHz from the individual spectral chunks in each sideband and IF band were averaged into an effective continuum channel (excluding the chunk containing a CO transition). The antenna-based complex gain response of the system was determined using the phase calibrator nearest to the target. The absolute amplitude scale was set based on observations of Uranus or planetary satellites, and is expected to be accurate

at the level of ∼10%. For each target, the continuum channels for both IF bands and sidebands from each set of observations were combined into a composite set of calibrated visibilities. The `MIRIAD` software package was used to Fourier invert those visibilities, perform a deconvolution using the `CLEAN` algorithm, and restore the `CLEAN`ed maps with a synthesized beam. The synthesized beam dimensions and RMS noise levels for the naturally weighted datasets are provided in Table 2.3. The SMA continuum maps are shown in Figures 2.2-2.4. In most cases, the observations of a given multiple system were not sufficient to clearly detect CO emission from any circumstellar gas: the few exceptions will be discussed elsewhere.

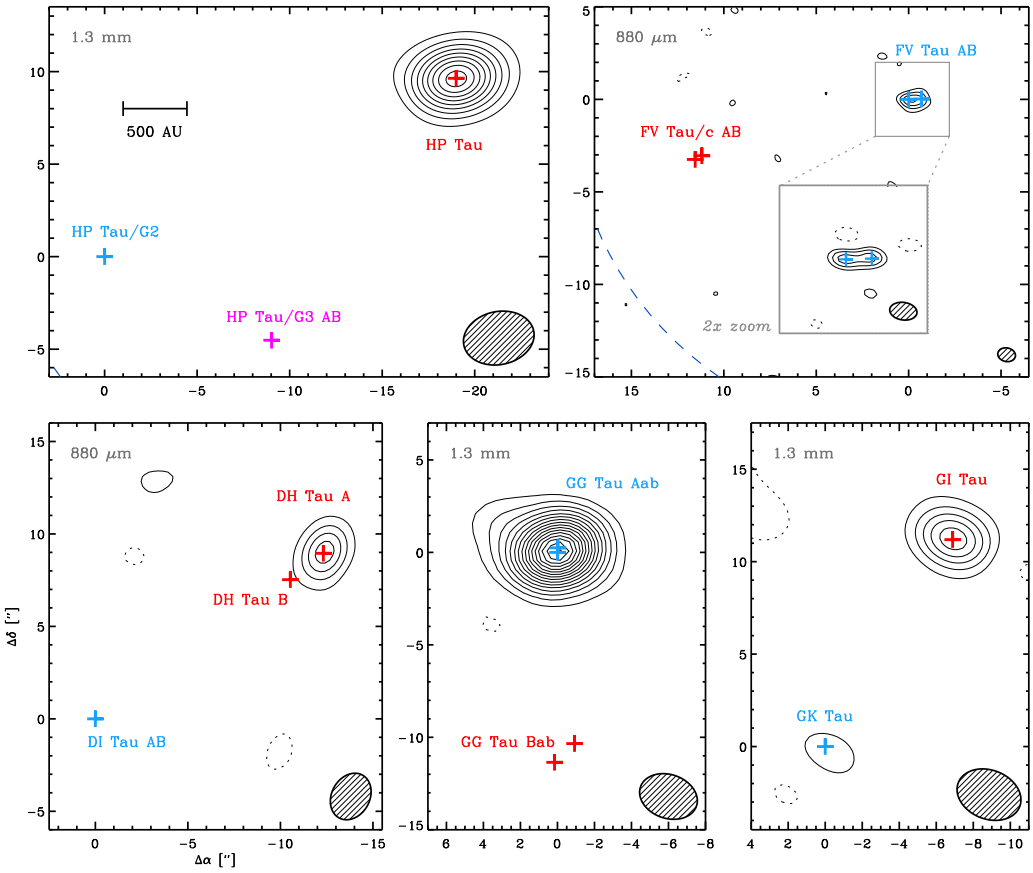

Figure 2.2: Mosaic of SMA continuum images for wide-separation multiple systems. Contours are drawn at $3\,\sigma$ intervals (see Table 2.3); hatched ellipses mark the synthesized beam dimensions. Stellar positions are marked with blue (primary), red (secondary), or purple (intermediate mass in higher-order systems) crosses. A blue dashed curve marks the SMA primary beam in the FV Tau map. The FV Tau inset shows the data synthesized at higher resolution, with a beam size of $0\farcs7 \times 0\farcs5$. The panels are drawn to scale; a 500 AU scale bar is marked in the HP Tau system panel (*top left*).

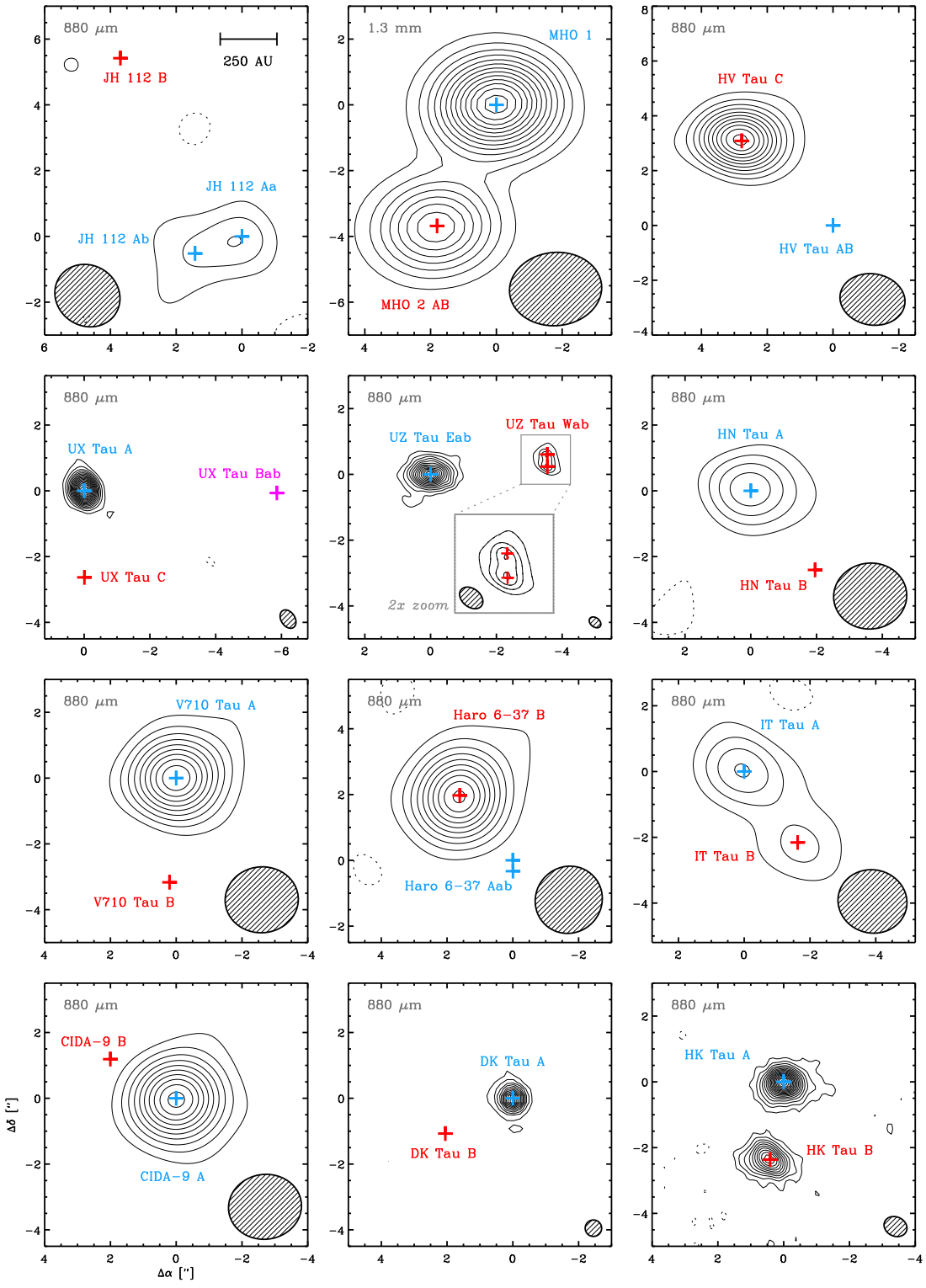

Figure 2.3: Same as Fig. 2.2, for medium separations.

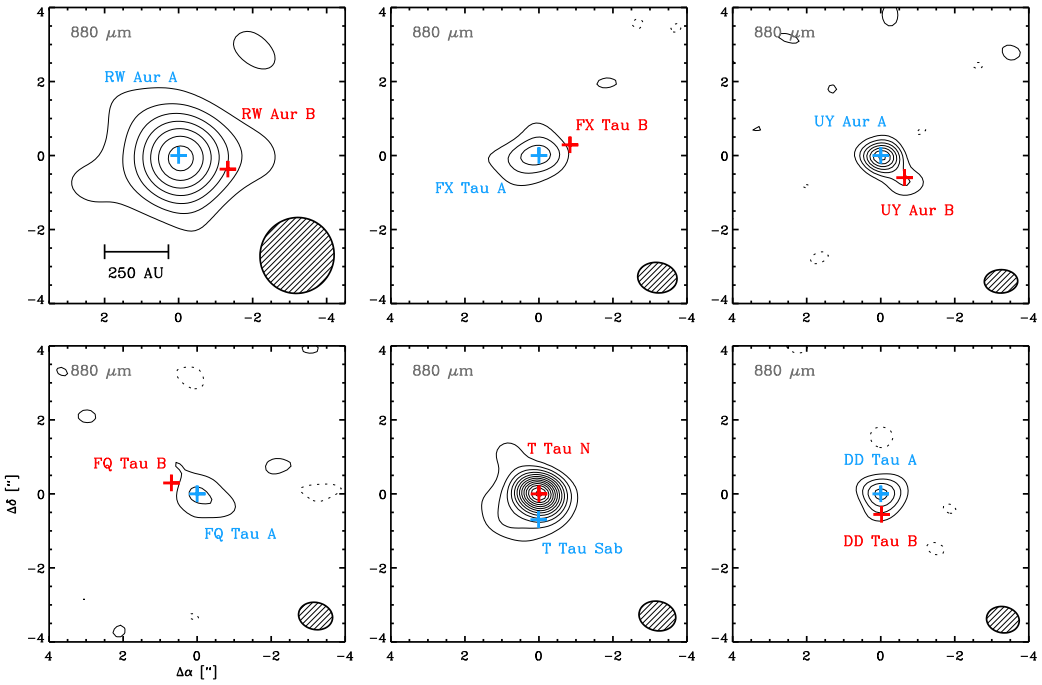

Figure 2.4: Same as Figs. 2.2 and 2.3, for small separations.

Table 2.3. Properties of Synthesized Continuum Maps

System	λ	RMS noise	beam size	beam PA	System	λ	RMS noise	beam size	beam PA
	[μm]	[mJy beam^{-1}]	[$''$]	[$^\circ$]		[μm]	[mJy beam^{-1}]	[$''$]	[$^\circ$]
(1)	(2)	(3)	(4)	(5)	(1)	(2)	(3)	(4)	(5)
MHO 1/2	1335	2.1	2.8×2.2	95	DD Tau	880	1.9	0.9×0.7	79
FQ Tau	880	1.2	0.9×0.7	77	T Tau	880	3.6	1.0×0.8	77
FV Tau	880	1.1	1.0×0.7	79	DI/DH Tau	880	3.3	2.6×2.1	151
UX Tau	880	0.9	0.6×0.4	33	FX Tau	880	1.6	1.1×0.8	82
DK Tau	880	0.7	0.5×0.5	0	HK Tau	880	1.4	0.7×0.6	65
V710 Tau	880	3.2	2.2×2.0	94	GG Tau	1335	2.2	3.2×2.4	32
UZ Tau	880	0.7	0.4×0.3	51	JH 112	880	1.9	2.0×1.8	57
GI/GK Tau	1335	0.7	3.6×2.6	68	HN Tau	880	2.1	2.2×2.0	96
IT Tau	880	1.4	2.1×1.9	78	HP Tau	1335	1.2	3.9×2.9	102
HV Tau	880	2.3	2.0×1.8	61	Haro 6-37	880	5.0	2.1×2.0	136
UY Aur	880	1.5	0.9×0.6	91	CIDA-9	880	2.4	2.2×2.0	98

Table 2.3—Continued

System	λ	RMS noise	beam size	beam PA	System	λ	RMS noise	beam size	beam PA
	[μm]	[mJy beam^{-1}]	[$''$]	[$^\circ$]		[μm]	[mJy beam^{-1}]	[$''$]	[$^\circ$]
(1)	(2)	(3)	(4)	(5)	(1)	(2)	(3)	(4)	(5)
RW Aur	880	3.6	2.1×2.0	159					

Note. — Col. (1): System name. Col. (2): Effective observing wavelength. Col. (3): RMS noise level ($1\,\sigma$) in the naturally weighted synthesis image (see Figures 2.2-2.4). Col. (4) & (5): Beam dimensions and major axis position angle.

2.4 Disk Properties from Simple Emission Models

The SMA survey observations described above comprise the largest resolved millimeter-wave census of circumstellar material in young multiple star systems to date. In this section, we aim to measure two fundamental properties from these data – luminosities (which are related to dust masses) and sizes – for the disks around the individual stellar components in each multiple system. These basic disk parameters are estimated by fitting a simple model of the continuum emission morphology directly to the observed visibilities. The 27 multiple systems in our sample contain 77 individual stars. The available data have sufficient angular resolution to associate any dust emission with 50 of those stars. The individual components in the close pairs MHO 2 AB, T Tau Sab, FS Tau AB, DI Tau AB, UX Tau Bab, XZ Tau AB, GG Tau Aab, UZ Tau Eab, V807 Tau AB, GH Tau AB, HP Tau/G3 AB, HV Tau AB, and Haro 6-37 Aab are not resolved. We treat the millimeter signal from each of these 13 pairs as if it arises from a "composite" disk (see §2.5.1).

Including two of those composites, there are 14 individual disks in this sample that are sufficiently well-resolved to provide robust estimates of their basic parameters. In these cases, we define a simple, azimuthally symmetric and geometrically flat emission model with a power-law radial surface brightness distribution, $I_\nu \propto R^{-x}$, that extends to an outer edge, R_d. The emission profile is normalized such that the total flux density $F_d = \int I_\nu d\Omega$. This parametric emission morphology is designed to mimic what would be expected from a disk structure model with power-law surface density ($\Sigma_d \propto R^{-p}$) and temperature ($T_d \propto R^{-q}$) profiles. Pressing that resemblance, the radial index x is analogous to the sum $p + q$ and the normalization F_d is a rough proxy for the product

$\kappa_d \langle T_d \rangle M_d$, where κ_d is the dust opacity, $\langle T_d \rangle$ is a characteristic temperature, and M_d is the dust mass, modulo small correction factors for any high optical depths in the disk center (Beckwith et al. 1990; Andrews & Williams 2005). Our data do not generally have enough sensitivity on long baselines to provide useful quantitative constraints on both the emission gradient and size, which are effectively degenerate at this modest resolution (see Mundy et al. 1996; Andrews & Williams 2007b). Since the key parameters of interest from the perspective of tidal interaction models are $\{F_d,\, R_d\}$, we elect to fix the gradient to a fiducial value, $x = 1.5$, motivated by the standard assumptions for irradiated accretion disks ($p = 1$, $q = 0.5$; see Hartmann et al. 1998). For reference, adjustments to the radial index of $\pm 30\%$ ($\Delta x \approx \pm 0.5$) induce systematic changes in the size estimates of $\sim$20-40%: steeper (shallower) gradients produce larger (smaller) sizes.

In addition to the two free parameters in the surface brightness model, $\{F_d,\, R_d\}$, there are formally five other parameters related to the projection of the model into the sky plane: the disk center relative to the observed phase center $\{\Delta\alpha,\, \Delta\delta\}$, the disk viewing geometry described by its apparent inclination and orientation $\{i_d,\, \mathrm{PA}_d\}$, and the distance to the observer $\{d\}$. The latter is fixed to $d = 145\,\mathrm{pc}$, with a systematic uncertainty estimated to be roughly $\pm 10\%$ (Loinard et al. 2007; Torres et al. 2007, 2009). We fix the centroid positions before estimating other parameters, typically based on an elliptical Gaussian fit to the visibilities for individual components that exhibit continuum emission. In general, that technique recovers the expected stellar positions well within the position accuracy of the SMA data ($\sim$0.″1 in an absolute sense, and considerably better in a relative sense for the few cases with multiple disk detections). For stellar components that do not exhibit any millimeter emission or may be partially blended with other components, we rely on the positions (or projected angular separations and

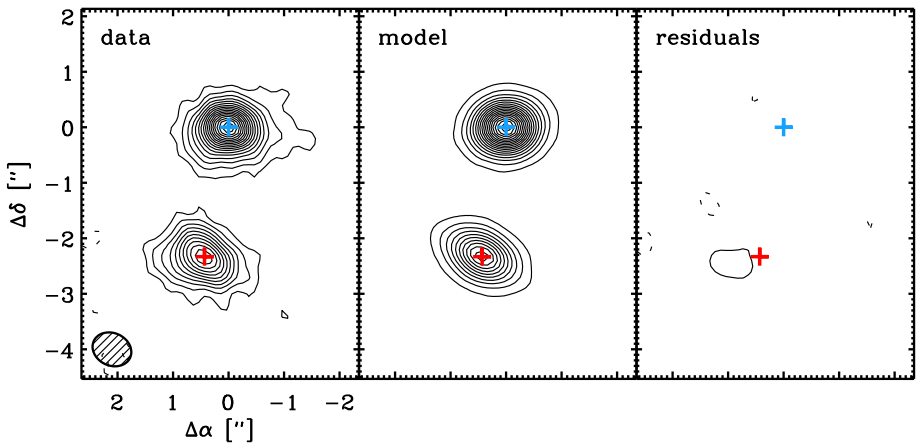

Figure 2.5: Model fit demonstration for the HK Tau binary. From left to right, the panels show the SMA 880 μm image, the best-fit model image, and the imaged residuals. Contours are drawn at 3 mJy beam^{-1} (3 σ) intervals. The synthesized beam is shown in the lower left of the data panel. The HK Tau A and B stellar positions are marked with blue and red crosses, respectively.

orientations) provided from optical/infrared measurements in the literature to assign their $\{\Delta\alpha, \Delta\delta\}$ values. In practice, we estimate the best-fit values of 4 free parameters $\{F_d, R_d, i_d, \mathrm{PA}_d\}$ and their uncertainties for each resolved disk by comparing model predictions directly with the SMA visibilities using the non-linear χ^2 minimization routine `MPFIT` (Markwardt 2009). In each case, several randomized initial parameter sets were employed to avoid trapping in local minima. The results are compiled in Table 2.4. Figure 2.5 shows an example model fit for the well-separated and resolved disks of the HK Tau binary.

Table 2.4. Resolved Disk Properties

Name	Disk Center		F_d	R_d	i_d	PA_d
	α [J2000]	δ [J2000]	[mJy]	[AU]	[°]	[°]
(1)	(2)	(3)	(4)	(5)	(6)	(7)
MHO 1	04 14 26.28	+28 06 02.90	(242 ± 3)	131 ± 28	32 ± 15	84 ± 28
T Tau N	04 21 59.44	+19 32 06.31	304 ± 3	64 ± 3	6 ± 21	90 ± 36
FV Tau A	04 26 53.53	+26 06 54.10	19 ± 3	121 ± 54	57 ± 15	119 ± 16
UX Tau A	04 30 04.00	+18 13 49.25	141 ± 1	57 ± 1	34 ± 2	174 ± 4
FX Tau A	04 30 29.64	+24 26 44.77	24 ± 3	219 ± 57	[45]	[90]
DK Tau A	04 30 44.25	+26 01 24.52	57 ± 1	76 ± 5	27 ± 9	115 ± 12
HK Tau A	04 31 50.57	+24 24 17.60	81 ± 2	102 ± 8	57 ± 4	118 ± 5
HK Tau B	04 31 50.60	+24 24 15.27	49 ± 2	164 ± 22	[84]	[40]
GG Tau Aab	04 32 30.36	+17 31 40.03	(557 ± 3)	305 ± 5	[37]	[7]
UZ Tau Eab	04 32 43.07	+25 52 30.80	367 ± 3	219 ± 3	50 ± 1	86 ± 1
UZ Tau Wa	04 32 42.83	+25 52 31.04	24 ± 2	63 ± 6	56 ± 4	40 ± 6

Table 2.4—Continued

Name	Disk Center		F_d	R_d	i_d	PA_d
	α [J2000]	δ [J2000]	[mJy]	[AU]	[°]	[°]
(1)	(2)	(3)	(4)	(5)	(6)	(7)
UZ Tau Wb	04 32 42.83	+25 52 31.41	41 ± 2	119 ± 10	[45]	[90]
HN Tau A	04 33 39.38	+17 51 52.12	34 ± 3	233 ± 63	[45]	[90]
HV Tau C	04 38 35.47	+26 10 41.24	98 ± 3	139 ± 21	[80]	99 ± 9
Haro 6-37 B	04 46 59.09	+17 02 39.87	218 ± 6	219 ± 15	[45]	[90]

Note. — Col. (1): Stellar component name. Col. (2) and (3): Adopted disk center coordinates. Col. (4): Flux density. Values in parenthesis correspond to measurements at a wavelength of 1.3 mm: all others are at 880 μm. Col. (5): Disk radius. Col. (6): Disk inclination angle, where 0° is face-on. Col. (7): Position angle (E of N) of the disk major axis projected on the sky. Values in square brackets were fixed in the modeling (see §2.4).

For 4 of the 14 disks with modeling results in Table 2.4, the emission is not sufficiently resolved to place meaningful constraints on the disk viewing geometry. In those cases (FX Tau A, UZ Tau Wb, HN Tau A, and Haro 6-37 B), we assumed a fiducial $\{i_d = 45, \mathrm{PA}_d = 90\}$ in order to calculate a reasonable estimate of $\{F_d, R_d\}$ (alternative viewing geometry selections produce the same flux densities and sizes within the quoted uncertainties). The viewing geometries for the HK Tau B, HV Tau C, and GG Tau Aab disks were fixed based on observations of their scattered light morphologies or molecular kinematics (Duchêne et al. 2010; McCabe et al. 2011; Guilloteau et al. 1999). The UX Tau A and GG Tau Aab disks were modeled as rings, with empty central regions out to radii of 25 and 185 AU based on the more sophisticated analyses of Andrews et al. (2011) and Guilloteau et al. (1999), respectively. The UZ Tau Eab circumbinary disk was also modeled as a ring, with no emission inside a radius of 15 AU: a detailed analysis of this disk will be provided elsewhere (see Chapter 3). Of the remaining 49 individual stars or close-pair composites, 27 have firmly detected – but *unresolved* – millimeter emission and 22 others do not. For simplicity, point source models were used to measure F_d for the population of detected, but unresolved, disks. After subtracting models of any emission from nearby stars, upper limits ($3\,\sigma$) on F_d were estimated for the undetected components by computing the RMS noise level in a $4'' \times 4''$ box centered on the stellar position in a synthesized residual map. The point source flux densities and upper limits for these 49 individual stellar components (or close-pair composites) are compiled in Table 2.5.

Table 2.5. Unresolved Disk Properties

Name	Disk Center		F_d	Name	Disk Center		F_d
	α [J2000]	δ [J2000]	[mJy]		α [J2000]	δ [J2000]	[mJy]
MHO 2 AB	04 14 26.47	+28 05 59.95	(138 ± 1)	GG Tau Bb	04 32 30.51	+17 31 28.68	(< 7)
DD Tau A	04 18 31.13	+28 16 28.82	24 ± 3	*FZ Tau*	04 32 31.76	+24 20 03.10	29 ± 7
DD Tau B	04 18 31.13	+28 16 28.26	9 ± 3	*FY Tau*	04 32 30.58	+24 19 57.29	< 27
FQ Tau A	04 19 12.81	+28 29 32.75	8 ± 2	JH 112 Aa	04 32 49.12	+22 53 02.52	10 ± 3
FQ Tau B	04 19 12.79	+28 29 33.44	< 5	JH 112 Ab	04 32 49.22	+22 53 03.04	5 ± 3
T Tau Sab	04 21 59.44	+19 32 05.61	< 10	JH 112 B	04 32 49.27	+22 53 07.89	< 6
FS Tau AB	04 22 02.18	+26 57 30.49	49 ± 6	*V807 Tau AB*	04 33 06.64	+24 09 54.90	20 ± 3
Haro 6-5B	04 22 00.70	+26 57 32.50	(134 ± 6)	*GH Tau AB*	04 33 06.22	+24 09 33.99	15 ± 3
FV Tau A	04 26 53.53	+26 06 54.10	15 ± 1	GK Tau	04 33 34.57	+24 21 05.64	(3 ± 1)
FV Tau B	04 26 53.47	+26 06 54.12	11 ± 1	GI Tau	04 33 34.06	+24 21 16.83	(12 ± 1)
FV Tau/c A	04 26 54.41	+26 06 50.77	< 5	HN Tau B	04 33 39.24	+17 51 49.71	< 6
FV Tau/c B	04 26 54.36	+26 06 51.03	< 5	IT Tau A	04 33 54.71	+26 13 27.36	16 ± 2
DI Tau AB	04 29 42.46	+26 32 49.38	< 10	IT Tau B	04 33 54.59	+26 13 25.21	11 ± 3
DH Tau A	04 29 41.64	+26 32 58.34	47 ± 4	HP Tau/G3 AB	04 35 53.50	+22 54 09.84	(< 4)

Table 2.5—Continued

Name	Disk Center		F_d	Name	Disk Center		F_d
	α [J2000]	δ [J2000]	[mJy]		α [J2000]	δ [J2000]	[mJy]
DH Tau B	04 29 41.74	+26 32 56.56	< 10	HP Tau/G2	04 35 54.16	+22 54 13.48	(< 4)
UX Tau Bab	04 30 03.59	+18 13 49.18	< 3	HP Tau	04 35 52.77	+22 54 23.17	(48 ± 2)
UX Tau C	04 30 04.00	+18 13 43.39	< 3	HV Tau AB	04 38 35.29	+26 10 38.16	< 7
FX Tau B	04 30 29.58	+24 26 45.06	< 5	Haro 6-37 Aab	04 46 58.98	+17 02 37.90	< 15
DK Tau B	04 30 44.39	+26 01 23.45	< 3	UY Aur A	04 51 47.39	+30 47 13.31	39 ± 3
XZ Tau AB	04 31 40.07	+18 13 57.18	(14 ± 3)	UY Aur B	04 51 47.34	+30 47 12.71	10 ± 3
HL Tau	04 31 38.44	+18 13 57.65	2360 ± 90	CIDA-9 A	05 05 22.82	+25 31 30.65	77 ± 3
V710 Tau A	04 31 57.80	+18 21 37.78	125 ± 3	CIDA-9 B	05 05 22.97	+25 31 31.84	< 7
V710 Tau B	04 31 57.81	+18 21 34.61	< 10	RW Aur A	05 06 49.57	+30 24 04.90	62 ± 6
V710 Tau C	04 31 59.68	+18 21 30.50	< 22	RW Aur B	05 06 49.47	+30 24 04.53	9 ± 5
GG Tau Ba	04 32 30.30	+17 31 29.69	(< 7)				

Note. — Col. (1): Stellar component name. Col. (2) and (3): Disk center coordinates. Col. (4): 880 μm flux density. Values in parenthesis correspond to 1.3 mm. The sources in italics have F_d values from single-dish photometry (Andrews & Williams 2005).

The emission from the individual disks in the RW Aur and DD Tau binaries is blended. In these cases, we adopted an iterative modeling strategy. First, a single disk model was fitted to the dominant emission component (the primaries) and subtracted from the data. An initial estimate of the disk model for the blended component (the secondaries) was made from the residuals. Based on those results, a composite model with both disk components was then used to fit the data and derive proper parameter estimates and uncertainties. This method naturally accounts for the blending with inflated formal parameter uncertainties for each model component. None of the disks in these pairs is spatially resolved, so the underlying model for each component disk is a point source.

2.5 Results

We aim to take advantage of this resolved millimeter-wave census to address some key aspects of disk evolution in the presence of stellar companions. To do that, we link our SMA survey results into a comprehensive compilation of stellar separations (ρ), component masses (M_p and M_s) and mass ratios (q), and millimeter luminosities (defined as the summed emission in a pair: $F_{\rm pair} = F_{d,p} + F_{d,s}$) for *all* of the known potentially interacting stellar pairs in Taurus (with spectral types F0 to M4). Those data are compiled in Table 2.6. A complementary list of *single* stars in Taurus with available millimeter-wave observations in the literature is provided in Table 2.7. We should note that there are 36 other single stars in this spectral type range in the compilation of Luhman et al. (2010) that, to our knowledge, have not yet been observed at millimeter wavelengths.

Table 2.6. Properties of Stellar Pairs in Taurus

System	Pair		ρ	q	M_p	$F_{\rm pair}$	Refs
	Primary	Secondary	[″]		[$M_\odot$]	[mJy]	
(1)	(2)	(3)	(4)	(5)	(6)	(7)	(8)
J04080782+2807280	J04080782 A	J04080782 B	0.044	0.13	0.30	(< 8)	1, 1, A
V773 Tau	V773 Tau Aa	V773 Tau Ab	0.0028	0.86	1.54	< 9	2, 2, B[a]
	V773 Tau Aab	V773 Tau B	0.14	0.29	2.87	< 9	3, 3[b], B[a]
	V773 Tau Aab	V773 Tau C	0.21	···	2.87	< 9	3, 3[b], B[a]
	V773 Tau B	V773 Tau C	0.20	···	1.33	< 9	3[c], 3[b], B[a]
	V773 Tau ABC	J0414118+2811535	23.38	∼0.03	> 4.20	(< 9)	4, 1[b], A
Anon 1	Anon 1 A	Anon 1 B	0.015	0.68	0.64	< 8	1, 1, B
MHO 1/2	MHO 1	MHO 2 AB	3.93	1.00	0.44	(380 ± 3)	4, 1, A
	MHO 2 A	MHO 2 B	0.050	0.34	0.33	(138 ± 1)	1, 1, A
MHO 3	MHO 3 A	MHO 3 B	0.031	0.81	0.72	(< 12)	1, 1, A
LkCa 3	LkCa 3 Aa	LkCa 3 Ab	0.0004	0.58	0.36	< 9	5[c], 5[b], B

Table 2.6—Continued

System	Pair		ρ	q	M_p	$F_{\rm pair}$	Refs
	Primary	Secondary	[″]		[$M_\odot$]	[mJy]	
(1)	(2)	(3)	(4)	(5)	(6)	(7)	(8)
	LkCa 3 Aab	LkCa 3 B	0.48	0.81	0.57	< 9	1, 1, B
FO Tau	FO Tau A	FO Tau B	0.15	1.00	0.33	13 ± 3	1, 1, B
LkCa 5	LkCa 5 A	LkCa 5 B	0.048	0.09	0.50	< 4	1, 1, B
V410 Tau	V410 Tau A	V410 Tau B	0.12	0.20	0.94	< 8	1, 1, B[a]
	V410 Tau AB	V410 Tau C	0.29	0.08	1.13	< 8	1, 1, B[a]
DD Tau	DD Tau A	DD Tau B	0.55	1.00	0.33	33 ± 4	1, 1, A
CZ Tau	CZ Tau A	CZ Tau B	0.32	0.50	0.54	< 9	1, 1, B
V410 Tau X-ray 7	V410 X-ray 7 A	V410 X-ray 7 B	0.032	0.65	0.60	(< 13)	1, 1, A
Hubble 4	Hubble 4 A	Hubble 4 B	0.028	0.73	0.72	< 9	1, 1, B
FQ Tau	FQ Tau A	FQ Tau B	0.75	0.83	0.40	8 ± 2	1, 1, A
LkCa 7	LkCa 7 A	LkCa 7 B	1.02	0.52	0.64	< 9	1, 1, B

Table 2.6—Continued

System	Pair		ρ	q	M_p	$F_{\rm pair}$	Refs
	Primary	Secondary	[″]		[$M_\odot$]	[mJy]	
(1)	(2)	(3)	(4)	(5)	(6)	(7)	(8)
T Tau	T Tau Sa	T Tau Sb	0.082	0.22	2.73	< 10	6, 6, A[a]
	T Tau Sab	T Tau N	0.68	0.63	3.34	304 ± 3	6[d], 6[b], A
FS Tau	FS Tau A	FS Tau B	0.23	0.52	0.64	49 ± 6	1, 1, B
	FS Tau AB	Haro 6-5B	19.88	0.85	0.97	(155 ± 7)	4, 1, B/C
LkCa 21	LkCa 21 A	LkCa 21 B	0.044	0.77	0.41	< 10	1, 1, B
J1-4872	J1-4872 Aa	J1-4872 Ab	0.17	0.86	0.64	< 8	1, 1, B
	J1-4872 Ba	J1-4872 Bb	0.10	0.67	0.59	< 8	7, 7[b], B
	J1-4872 Aab	J1-4872 Bab	3.38	0.83	1.19	< 8	4, 1, B
FV Tau	FV Tau A	FV Tau B	0.70	0.73	0.82	26 ± 2	1, 1, A
	FV Tau/c A	FV Tau/c B	0.70	0.73	0.45	< 5	1, 1, A
	FV Tau AB	FV Tau/c AB	12.29	0.55	1.42	26 ± 2	4, 1, A

Table 2.6—Continued

System	Pair		ρ	q	M_p	$F_{\rm pair}$	Refs
	Primary	Secondary	[″]		[$M_\odot$]	[mJy]	
(1)	(2)	(3)	(4)	(5)	(6)	(7)	(8)
DF Tau	DF Tau A	DF Tau B	0.073	0.90	0.50	9 ± 2	1, 1, B
J1-507	J1-507 A	J1-507 B	0.079	0.98	0.27	< 6	1, 1, B
FW Tau	FW Tau A	FW Tau B	0.15	1.00	0.27	5 ± 1	1, 1, B
DI/DH Tau	DI Tau A	DI Tau B	0.12	0.13	0.64	< 10	1, 1, A
	DH Tau A	DH Tau B	2.34	0.07	0.57	47 ± 4	8, 8[b] A
	DI Tau AB	DH Tau AB	15.23	0.85	0.72	47 ± 4	4, 1, A
UX Tau	UX Tau A	UX Tau C	2.69	0.15	1.20	141 ± 1	1, 1, A
	UX Tau A	UX Tau Bab	5.86	0.86	1.20	141 ± 1	1, 1, A
	UX Tau Ba	UX Tau Bb	0.14	0.81	0.57	< 3	1, 1, A
	UX Tau Bab	UX Tau C	6.45	0.17	1.03	< 3	1, 1, A
FX Tau	FX Tau A	FX Tau B	0.89	0.47	0.57	24 ± 3	1, 1, A

Table 2.6—Continued

System	Pair		ρ	q	M_p	$F_{\rm pair}$	Refs
	Primary	Secondary	[″]		[$M_\odot$]	[mJy]	
(1)	(2)	(3)	(4)	(5)	(6)	(7)	(8)
DK Tau	DK Tau A	DK Tau B	2.34	0.89	0.64	57 ± 1	1, 1, A
ZZ Tau	ZZ Tau A	ZZ Tau B	0.042	0.48	0.40	< 8	1, 1, B
V927 Tau	V927 Tau A	V927 Tau B	0.27	0.83	0.40	< 10	1, 1, B
XZ/HL Tau	XZ Tau A	XZ Tau B	0.29	0.66	0.50	(14 ± 3)	1, 1, C[a]
	HL Tau	XZ Tau AB	23.31	0.99	0.83	2390 ± 90	4, 1, B
HK Tau	HK Tau A	HK Tau B	2.34	1.00	0.57	130 ± 3	1, 1, A
V710 Tau	V710 Tau A	V710 Tau B	3.03	0.70	0.57	125 ± 3	4, 1, A
	V710 Tau AB	V710 Tau C	27.97	0.41	0.97	125 ± 3	4, 1, A
V827 Tau	V827 Tau A	V827 Tau B	0.093	0.63	0.72	< 6	1, 1, B
V826 Tau	V826 Tau A	V826 Tau B	0.014	1.00	0.80	< 7	9[c]; 9[c]; B
V928 Tau	V928 Tau A	V928 Tau B	0.20	0.95	0.60	< 8	1, 1, B

Table 2.6—Continued

System	Pair		ρ	q	M_p	$F_{\rm pair}$	Refs
	Primary	Secondary	[″]		[$M_\odot$]	[mJy]	
(1)	(2)	(3)	(4)	(5)	(6)	(7)	(8)
	V928 Tau AB	CFHT-Tau-7	18.25	0.10	1.17	< 8	4, 1, B
GG Tau	GG Tau Aa	GG Tau Ab	0.24	0.83	0.72	(557 ± 3)	1, 1, A
	GG Tau Ba	GG Tau Bb	1.48	0.31	0.11	(< 5)	10, 10[b], A
	GG Tau Aab	GG Tau Bab	10.38	0.14	1.32	(557 ± 3)	4, 1, A
FZ/FY Tau	FZ Tau	FY Tau	17.17	0.89	0.72	29 ± 7	4, 1, B
UZ Tau	UZ Tau Ea	UZ Tau Eb	0.0009	0.30	1.05	367 ± 3	11[c], 11[c], A
	UZ Tau Wa	UZ Tau Wb	0.37	0.80	0.50	65 ± 3	12, 12, A
	UZ Tau Eab	UZ Tau Wab	3.56	0.66	1.36	432 ± 4	4, 1, A
JH 112	JH 112 Aa	JH 112 Ab	1.52	0.02	0.82	15 ± 4	1, 1, A
	JH 112 Aab	JH 112 B	6.56	0.31	0.83	15 ± 4	4, 1, A
V807/GH Tau	V807 Tau A	V807 Tau Bab	0.28	0.62	0.72	20 ± 3	13, 13, B

Table 2.6—Continued

System	Pair		ρ	q	M_p	$F_{\rm pair}$	Refs
	Primary	Secondary	[″]		[$M_\odot$]	[mJy]	
(1)	(2)	(3)	(4)	(5)	(6)	(7)	(8)
	V807 Tau Ba	V807 Tau Bb	0.037	···	< 0.45	···	13, 13
	GH Tau A	GH Tau B	0.30	1.00	0.50	15 ± 3	1, 1, B
	V807 Tau AB	GH Tau AB	21.77	0.53	1.89	35 ± 4	4, 1, B
GI/GK Tau	GI Tau	GK Tau	13.14	1.00	0.72	(15 ± 1)	4, 1, A
IS Tau	IS Tau A	IS Tau B	0.22	0.52	0.64	30 ± 3	1, 1, B
HN Tau	HN Tau A	HN Tau B	3.10	0.27	0.82	34 ± 3	4, 1, A
IT Tau	IT Tau A	IT Tau B	2.41	0.29	0.94	27 ± 4	1, 1, A
J2-2041	J2-2041 A	J2-2041 B	0.42	0.41	0.33	< 19	1, 1, B
HBC 407	HBC 407 A	HBC 407 B	0.14	0.44	2.08	< 14	1, 1, B
FF Tau	FF Tau A	FF Tau B	0.037	0.44	0.72	< 4	1, 1, B
HBC 412	HBC 412 A	HBC 412 B	0.70	1.00	0.50	< 9	1, 1, B

Table 2.6—Continued

System	Pair		ρ	q	M_p	$F_{\rm pair}$	Refs
	Primary	Secondary	[″]		[$M_\odot$]	[mJy]	
(1)	(2)	(3)	(4)	(5)	(6)	(7)	(8)
CoKu Tau/3	CoKu Tau/3 A	CoKu Tau/3 B	2.07	0.17	0.57	< 8	1, 1, B
HP Tau	HP Tau/G2	HP Tau/G3 AB	10.09	0.38	2.49	(< 4)	4, 1, A
	HP Tau/G2	HP Tau	21.30	0.38	2.49	(48 ± 2)	4, 1, A
	HP Tau	HP Tau/G3 AB	16.70	1.00	0.95	(48 ± 2)	4, 1, A
	HP Tau/G3 A	HP Tau/G3 B	0.030	0.31	0.72	(< 4)	1, 1, A
Haro 6-28	Haro 6-28 A	Haro 6-28 B	0.65	0.66	0.50	11 ± 3	1, 1, B
HV Tau	HV Tau A	HV Tau B	0.036	0.61	0.57	< 7	4, 1, A
	HV Tau AB	HV Tau C	3.98	0.78	0.92	98 ± 3	4, 1, A
VY Tau	VY Tau A	VY Tau B	0.66	0.29	0.64	< 10	1, 1, B
GN Tau	GN Tau A	GN Tau B	0.34	0.87	0.45	12 ± 3	1, 1, B
JH 223	JH 223 A	JH 223 B	2.07	0.11	0.50	< 7	1, 1, B

Table 2.6—Continued

System	Pair		ρ	q	M_p	$F_{\rm pair}$	Refs
	Primary	Secondary	[″]		[$M_\odot$]	[mJy]	
(1)	(2)	(3)	(4)	(5)	(6)	(7)	(8)
IW Tau	IW Tau A	IW Tau B	0.29	0.93	0.72	< 9	1, 1, B
CoKu Tau/4	CoKu Tau/4 A	CoKu Tau/4 B	0.054	0.82	0.54	9 ± 3	1, 1, B
J04414565+2301580	J04414565 Aa	J04414565 Ab	0.22	0.10	0.40	< 24	1, 1, A
	J04414565 Aab	J04414565 B	12.37	0.06	0.44	< 24	4, 1, A
LkHα 332	LkHα 332/G2 A	LkHα 332/G2 B	0.23	0.64	0.72	< 9	1, 1, B
	LkHα 332/G1 A	LkHα 332/G1 B	0.24	0.55	0.57	12 ± 3	1, 1, B
	V955 Tau A	V955 Tau B	0.32	0.63	0.72	14 ± 2	1, 1, B
	LkHα 332/G2 AB	V955 Tau AB	10.51	0.99	1.18	14 ± 2	4, 1, B
	LkHα 332/G2 AB	LkHα 332/G1 AB	25.88	0.75	1.18	12 ± 3	4, 1, B
DP Tau	DP Tau A	DP Tau B	0.11	0.74	0.64	< 10	1, 1, B
RX J0446.7+2459	RX J0446 A	RX J0446 B	0.051	0.47	0.27	(< 5)	1, 1, D

Table 2.6—Continued

System	Pair		ρ	q	M_p	$F_{\rm pair}$	Refs
	Primary	Secondary	[″]		[$M_\odot$]	[mJy]	
(1)	(2)	(3)	(4)	(5)	(6)	(7)	(8)
DQ Tau	DQ Tau A	DQ Tau B	0.0004	0.97	0.65	208 ± 8	14[c], 14, B
Haro 6-37	Haro 6-37 Aa	Haro 6-37 Ab	0.33	0.11	0.72	< 15	1, 1, A
	Haro 6-37 Aab	Haro 6-37 B	2.62	0.90	0.80	218 ± 6	1, 1, A
UY Aur	UY Aur A	UY Aur B	0.88	0.70	0.64	49 ± 4	1, 1, A
St 34	St 34 Aa	St 34 Ab	< 0.01	1.00	0.40	< 11	15, 15, B
	St 34 Aab	St 34 B	1.18	0.20	0.80	< 11	1, 1, B
J04554757/J04554801	J04554757+3028077	J04554801+3028050	6.31	0.70	0.20	< 23	4, 1, A
HBC 427	HBC 427 A	HBC 427 B	0.032	0.49	1.45	< 14	1, 1, B
CIDA-9	CIDA-9 A	CIDA-9 B	2.34	0.58	0.72	77 ± 3	1, 1, A
CIDA-10	CIDA-10 A	CIDA-10 B	0.083	0.99	0.27	< 11	1, 1, B
CIDA-11	CIDA-11 A	CIDA-11 B	0.097	0.76	0.27	< 8	1, 1, B

Table 2.6—Continued

System	Pair		ρ	q	M_p	$F_{\rm pair}$	Refs
	Primary	Secondary	[″]		[$M_\odot$]	[mJy]	
(1)	(2)	(3)	(4)	(5)	(6)	(7)	(8)
RW Aur	RW Aur A	RW Aur B	1.38	0.60	1.20	71 ± 8	1, 1, A

Notes to Table 2.6: Col. (1): System name. Col (2): Primary designation of specified pair (note that this can consist of more than one star; see §2.2). Col. (3): Secondary designation of specified pair. Col. (4): Angular separation of the pair. Col. (5): Mass ratio of the pair ($q = M_s/M_p$). Col. (6): Estimated stellar mass of the primary component of the pair. Col. (7): Composite 880 μm flux density or upper limit for the pair. Values in parenthesis were measured instead at 1.3 mm: the analysis in §2.5 assumes a conservative scaling by a factor $(1.3/0.88)^2 \approx 2.2$. Col. (8): References for ρ, q, and $F_{\rm pair}$: [1] = Kraus et al. (2011), [2] = Boden et al. (2007), [3] = Duchêne et al. (2003a), [4] = Kraus & Hillenbrand (2009b), [5] = Mathieu (1994), [6] = Duchêne et al. (2006), [7] = Correia et al. (2006), [8] = Itoh et al. (2005), [9] = Massarotti et al. (2005), [10] = White et al. (1999), [11] = Jensen et al. (2007), [12] = Kraus & Hillenbrand (2009a), [13] = Schaefer et al. (2006), [14] = Mathieu et al. (1997), [15] = White & Hillenbrand (2005), and [A] = this article, [B] = Andrews & Williams (2005), [C] = Osterloh & Beckwith (1995), [D] = Schaefer et al. (2009).

(a) The marginal detections of millimeter emission in the V773 Tau and V410 Tau systems by Andrews & Williams (2005) are likely unrelated to circumstellar dust. Both systems are known to emit relatively strong synchrotron radio signals (Massi et al. 2006; Bieging et al. 1984). To be conservative, we consider these systems to have only upper limits on their millimeter luminosities. Synchrotron contamination from T Tau Sab is also likely to dominate over thermal emission from dust, even at millimeter wavelengths (see Loinard et al. 2007). The millimeter emission from the XZ Tau binary may also be contaminated, given its relatively bright centimeter-wave signal (see Carrasco-González et al. 2009). Moriarty-Schieven et al. (2006) suggest a smaller 880 μm flux density of $\sim$10 mJy.

(b) The V773 Tau A-B mass ratio was computed assuming the V773 Tau Aab system mass from Boden et al. (2007). V773 Tau C is an "infrared companion" (Duchêne et al. 2003a), so there are no reliable estimates of its mass to compute q. The total mass of LkCa 3 Aab estimated by Kraus et al. (2011) was used to help determine the mass ratio of the spectroscopic binary. The Duchêne et al. (2006) results were used in conjunction with the measurements of White & Ghez (2001) to estimate the T Tau Sab-N mass ratio. The DH Tau AB and GG Tau Bab mass ratios implicitly assume the M_p values derived by Kraus et al. (2011). The mass ratio for J1-4872 Bab was estimated from the spectral type and K-band magnitude difference from Correia et al. (2006), as described by Kraus et al. (2011).

(c) The single-lined spectroscopic binaries LkCa 3 Aab and UZ Tau Eab have a separation weighted by an unknown factor of $\sin i$ and a mass ratio proportional to $(\sin i)^3$ (although an independent inclination estimate is available for UZ Tau Eab, assuming its gas disk is co-planar; see Simon et al. 2000). The double-lined spectroscopic binaries V826 Tau AB and DQ Tau have only their separations weighted by $\sin i$; the mass ratios are determined precisely. White & Hillenbrand (2005) demonstrated that St 34 Aab is a single-lined spectroscopic binary, but did not have sufficient radial velocity data to constrain the orbit. The V773 Tau B-C projected separation was estimated using the weighted mean position offsets at the same epochs from Duchêne et al. (2003a).

(d) Although the current projected separation for the T Tau Sab-N pair is $\sim 0\farcs7$ (Duchêne et al. 2006), astrometric monitoring of the pair suggests that the true separation is likely substantially larger. Köhler et al. (2008) suggest that the pair may be near periastron on an eccentric orbit with a much larger true separation, $a \sim 1500\,\mathrm{AU}$, than would be suggested by the projected distance on the sky. In the analysis of §2.5,

we adopt their estimate, but note that the major features of our statistical analysis do not depend on that decision.

Table 2.7. Single Stars Observed at Millimeter Wavelengths

Name	M_* [$M_\odot$]	F_d [mJy]	Ref	Name	M_* [$M_\odot$]	F_d [mJy]	Ref
(1)	(2)	(3)	(4)	(1)	(2)	(3)	(4)
LkCa 1	0.27	< 8	1, A	L1551-55	0.72	< 5	1, A
IRAS 04108+2910	0.30	(< 20)	1, B	V830 Tau	0.72	< 6	1, A
FM Tau	0.64	32 ± 8	1, A	IRAS 04301+2608	0.64	18 ± 6	1, A
CW Tau	0.94	66 ± 6	1, A	DL Tau	0.72	440 ± 40	1, A
FP Tau	0.27	(< 9)	1, B	DM Tau	0.57	210 ± 1	1, E
CX Tau	0.45	25 ± 6	1, A	CI Tau	0.72	324 ± 6	1, A
LkCa 4	0.72	< 4	1, A	JH 108	0.57	< 7	1, A
CY Tau	0.57	140 ± 5	1, A	AA Tau	0.72	144 ± 5	1, A
V410 Tau X-ray 1	0.30	< 9	1, C	HO Tau	0.60	44 ± 6	1, A
HBC 372	0.94	< 8	1, A	DN Tau	0.64	201 ± 7	1, A
HBC 376	0.72	< 6	1, A	HQ Tau	0.94	11 ± 3	1, A
BP Tau	0.72	130 ± 7	1, A	LkCa 14	0.64	< 9	1, A
V819 Tau	0.72	< 9	1, A	DO Tau	0.64	258 ± 42	1, A
DE Tau	0.50	90 ± 7	1, A	LkCa 15	1.01	410 ± 1	1, E
RY Tau	1.46	560 ± 30	1, A	ITG 33A	0.40	(< 5)	1, B
HD 283572	2.26	< 9	1, A	IRAS 04385+2550	0.64	(24 ± 1)	1, B
FT Tau	0.60	121 ± 5	1, A	GO Tau	0.64	173 ± 7	1, A
IRAS 04216+2603	0.64	(< 20)	1, B	DR Tau	0.72	533 ± 7	1, A

Table 2.7—Continued

Name	M_* [$M_\odot$]	F_d [mJy]	Ref	Name	M_* [$M_\odot$]	F_d [mJy]	Ref
(1)	(2)	(3)	(4)	(1)	(2)	(3)	(4)
IP Tau	0.64	34 ± 5	1, A	DS Tau	0.82	39 ± 4	1, A
DG Tau	0.94	1100 ± 100	1, A	Haro 6-39	···	36 ± 6	··· , A
IRAS 04260+2642	0.94	(105 ± 10)	1, D	GM Aur	0.94	640 ± 4	1, E
HBC 388	1.46	< 6	1, A	LkCa 19	1.69	< 10	1, A
IQ Tau	0.60	178 ± 3	1, A	SU Aur	2.34	74 ± 3	1, A
JH 56	0.60	< 8	1, A	V836 Tau	0.72	74 ± 3	1, A
L1551-51	0.72	< 13	1, A	CIDA-8	0.33	27 ± 3	1, A
Haro 6-13	0.64	395 ± 56	1, A	CIDA-12	0.27	< 7	1, A

Note. — Col. (1): Star name. Col. (2): Estimated stellar mass. Col. (3): 880 μm flux density or upper limit. Values in parenthesis were measured instead at 1.3 mm: the analysis in §2.5 assumes a conservative scaling by a factor $(1.3/0.88)^2 \approx 2.2$. Col. (4): References for M_* and F_d: [1] = Kraus et al. (2011), and [A] = Andrews & Williams (2005), [B] = Schaefer et al. (2009), [C] = Motte & André (2001), [D] = Mannings & Emerson (1994), and [E] = Andrews et al. (2011).

2.5.1 Millimeter detection statistics

If interactions with companions efficiently remove material from circumstellar disks in young multiple systems, there should be a clear signature in the relative detection fractions of millimeter-wave emission (a rough proxy for dust mass) between isolated (single) stars and the individual stellar components of multiple systems: the fraction of stars that exhibit detectable millimeter emission, $f_{\rm mm} = N_{\rm det}/N_{\rm tot}$, should be substantially higher for singles compared to multiples. This feature has been noted anecdotally in the past (e.g., Jensen et al. 1994, 1996b; Osterloh & Beckwith 1995; Andrews & Williams 2005), but the inability to assign millimeter emission to individual components in multiple systems has limited any firm quantitative assessment of the detection statistics.

There are millimeter-wave continuum measurements available for 52 single stars in Taurus, 48 binaries (96 stars), 13 triples (39 stars), 7 quadruples (28 stars), 2 quintuples (10 stars), and 1 sextuple (6 stars; the LkHα 332 system). Using the component-resolved F_d measurements in Tables 2.4 and 2.5 along with the additional literature photometry compiled in Tables 2.6 and 2.7, we computed the $f_{\rm mm}$ values for single stars and multiples listed in Table 2.8. The ranges of $N_{\rm det}$ and $f_{\rm mm}$ for multiples correspond to the potential distribution of the observed millimeter emission among any unresolved components. We find that 32 of 52 single stars show millimeter emission, $f_{\rm mm} = 62 \pm 11\%$, while only 50-67 of 179 individual stars in multiple systems have millimeter-wave detections, $f_{\rm mm} = 28\text{-}37 \pm 5\%$. A two-tailed Fisher Exact test confirms that these are indeed statistically different detection fractions, with a p-value < 0.002. Remarkably, the millimeter detection fraction for individual stars in multiple systems

does not depend on the number of companions: binaries, triples, and higher-order groups all have $f_{\rm mm} \approx 1/3$, roughly half the detection rate for singles. That uniformity is a testament to the hierarchical nature of multiples, where higher-order ($N_* \geq 3$) systems tend to be be constructed of sets of binary pairs.

Given that the detection fraction for stars with companions is roughly half that for stars without them, it may seem natural to assume that only one stellar component in a multiple retains disk material. While not uncommon, this is not necessarily the typical scenario. Of the 48 binaries in Taurus, 20 exhibit millimeter emission. Of those 20 pairs, our millimeter observations have resolved the individual components of 12 (from 24 stars). In 6 of those pairs, the emission is concentrated solely around the primary. In the other 6, both components show some emission – however, the primary is *always* brighter. So, for the sub-population of component-resolved binaries with millimeter emission, the detection fraction for individual stars is actually fairly large (18/24). In the higher order multiples, the situation is slightly more complicated by their hierarchical structure. In some cases, we find dust emission coincident with all components, albeit usually with some pair presumably surrounded by a circum*binary* disk (e.g., UZ Tau, MHO 1/2). In others, the dust emission is only present around a more isolated, distant companion (e.g., HV Tau, Haro 6-37).

As might be expected, the likelihood that any individual component of a multiple system harbors a circumstellar disk that is massive enough to generate detectable millimeter emission depends critically on the individual details of the system. The following sections explore the potentially observable signatures expected from star-disk interactions, with a more explicit focus on some key connections between the stellar properties tied to orbital dynamics and the basic disk characteristics that can be inferred

Table 2.8. Millimeter Detection Statistics

Type	$N_{\rm det}$	$N_{\rm tot}$	$f_{\rm mm}$
singles	32	52	$62 \pm 11\%$
binaries	26-34	96	$27\text{-}35 \pm 5\%$
triples	11-15	39	$28\text{-}38 \pm 10\%$
higher order	13-18	44	$30\text{-}41 \pm 10\%$
all multiples	50-67	179	$28\text{-}37 \pm 5\%$

Note. — Col. (1): Type of stellar system. Col. (2): Number of individual stars with detected millimeter emission. Col. (3): Total number of stars of that category. Col. (4): Millimeter detection fraction.

from the millimeter data.

2.5.2 Pair demographics and disk – star connections

Theoretical models of star-disk interactions in binary pairs suggest that the separation between the stellar components is the key property that controls the tidal truncation of individual circumstellar disks (Artymowicz & Lubow 1994; Pichardo et al. 2005). These interactions effectively remove mass from the outer regions of these disks (either by accretion or ejection into the local interstellar medium), such that stellar pairs with smaller separations should harbor smaller – and therefore less massive – disks. Since the cool dust in the outer disk that is being stripped by this process emits continuum radiation at millimeter wavelengths, these tidal interactions should naturally produce an observable trend where the millimeter luminosity is positively correlated with the separation of the stellar pair. Indeed, the pioneering work on this subject by Jensen et al. (1994, 1996b) clearly identified that the millimeter luminosities for pairs with projected separations $a_p \leq$ 50-100 AU were statistically lower than their more widely-separated counterparts or single stars. These different populations were confirmed with larger and deeper millimeter-wave surveys (Osterloh & Beckwith 1995; Andrews & Williams 2005), but the detailed distribution of $F_{\rm pair}$ with respect to a_p has remained unclear for two reasons: the low resolution of single-dish millimeter-wave photometry often included several pairs together, and the multiplicity census of the nearest star-forming regions was incomplete. Our survey mitigates these issues, providing an opportunity to look at the details of the millimeter luminosity–separation distribution.

Figure 2.6*a* shows $F_{\rm pair}$ as a function of a_p for the 111 stellar pairs in Taurus (see

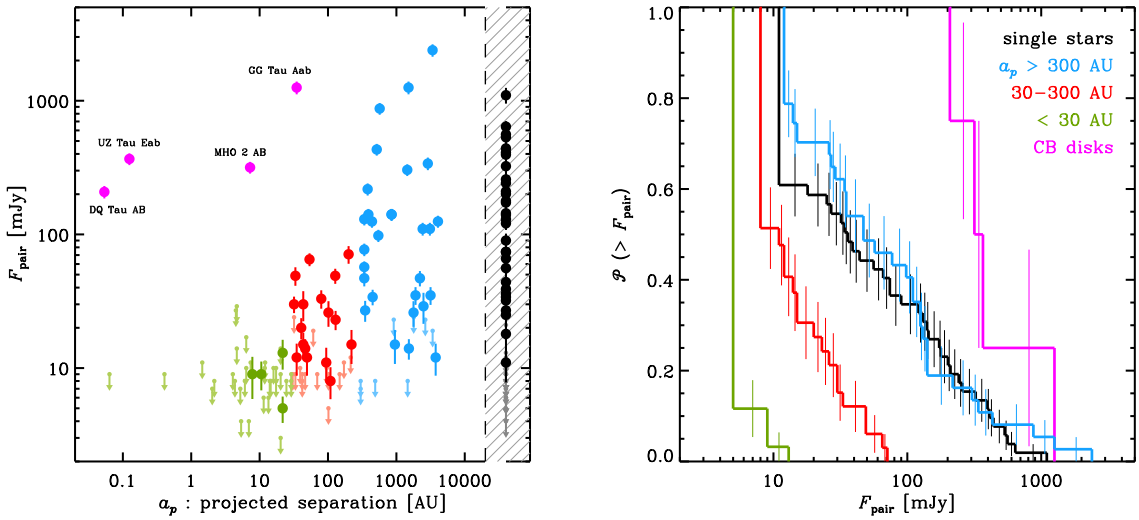

Figure 2.6: (*a*) A comparison of millimeter flux densities from potentially interacting pairs as a function of the projected pair separation. Single stars are shown to the right of the plot as black points for reference. The pair population can be distinguished into 4 clear sub-categories: wide ($a_p > 300$ AU), medium ($a_p = 30$-300 AU), and small ($a_p < 30$ AU) pairs, and circumbinary disks (*purple*). (*b*) The cumulative distributions of millimeter flux densities for each of these sub-categories, constructed with the Kaplan-Meier product-limit estimator to include the available upper limits. Millimeter luminosity is strongly dependent on projected separation.

Table 2.6), along with the 52 single stars that have millimeter-wave measurements (see Table 2.7; black points, gray upper limits). This diagram is a striking confirmation of the original conclusions of Jensen et al., plainly demonstrating that millimeter continuum luminosities scale with the separation between stellar pairs. However, as the pair separation decreases, the *maximum* millimeter luminosities appear to decline in discrete jumps (rather than continuously) at two relatively well-defined locations: $a_p \approx 300$ and 30 AU ($\rho \approx 2$ and $0.2''$, respectively). These features facilitate a natural breakdown of the Taurus pairs into distinct sub-populations. The distribution of $F_{\rm pair}$ for wide pairs,

with projected separations greater than 300 AU (*blue*), is similar to the distribution for single stars. At medium separations – a_p = 30-300 AU (*red*) – we find a notable absence of bright pairs and a decreased detection rate. At yet smaller separations, $a_p < 30$ AU (*green*), only a few pairs exhibit very weak millimeter-wave emission. A small group of dramatic outliers sparsely populate the otherwise empty region of bright pairs with small separations (*purple*): these pairs are known or suspected to harbor massive circum*binary* rings (e.g., see Piétu et al. 2011, regarding GG Tau Aab).

The cumulative distributions of $F_{\rm pair}$ for each separation-based sub-population can better quantify this apparent trend. The $\mathcal{P}_a(>F_{\rm pair})$ distributions shown together in Figure 2.6*b* were constructed using the Kaplan-Meier product-limit estimator to properly account for the substantial number of pairs in each sub-population that exhibit no millimeter emission (see Feigelson & Nelson 1985). The distributions are compared directly with the standard two-sample tests used in survival analysis in Table 2.9. These tests confirm the qualitative examination of Figure 2.6*a*: (1) wide pairs and single stars have statistically indistinguishable millimeter luminosity distributions; (2) medium pairs have significantly lower luminosities; and (3) small pairs have yet less millimeter emission. The $\mathcal{P}_a(>F_{\rm pair})$ in Figure 2.6*b* have similar functional forms, albeit shifted in luminosity. A simple scaling indicates that $F_{\rm pair}$ decreases by a factor of $\sim$5 from wide to medium separations, and then another factor of 5 from medium to small separations. These trends are not an artifact of including non-detections in the analysis: similar conclusions are drawn by comparing only the detected pairs in the same sub-populations using the two-sided Kolmogorov-Smirnov (K-S) test (see Table 2.9).

Models of star-disk interactions also postulate an association between the amount of disk truncation and the component masses of the stellar pair. Massive companions impart

Table 2.9. Two-Sample Tests Comparing Millimeter Luminosity Distributions

Group 1	Group 2	$\mathcal{P}$(survival)	$\mathcal{P}$(K-S)
single stars	wide pairs (>300 AU)	0.20-0.40	0.37
wide pairs (>300 AU)	medium pairs (30-300 AU)	<0.00006	0.017
medium pairs (30-300 AU)	small pairs (<30 AU)	<0.00005	0.047
high mass ratios ($q > 0.5$)	low mass ratios ($q < 0.5$)	<0.04	0.48
wide pairs with $q > 0.5$	wide pairs with $q < 0.5$	<0.00001	0.77
medium pairs with $q > 0.5$	medium pairs with $q < 0.5$	<0.08	0.10
single stars	primaries in pairs	0.41-0.98	···
primaries in pairs	secondaries in pairs	<0.008	···

Note. — Cols. (1) & (2): The sub-populations being compared. Col. (3): The probability that these two groups are drawn from the same parent distributions. The listed values correspond to the range or more conservative limit from the standard two-sample tests used in survival analysis (Peto-Prentice, Logrank, and Gehan tests). Col. (4): Same as Col. (3), but for the special case that includes only those pairs with millimeter-wave detections in each sub-population, derived from the two-sided Kolmogorov-Smirnov test.

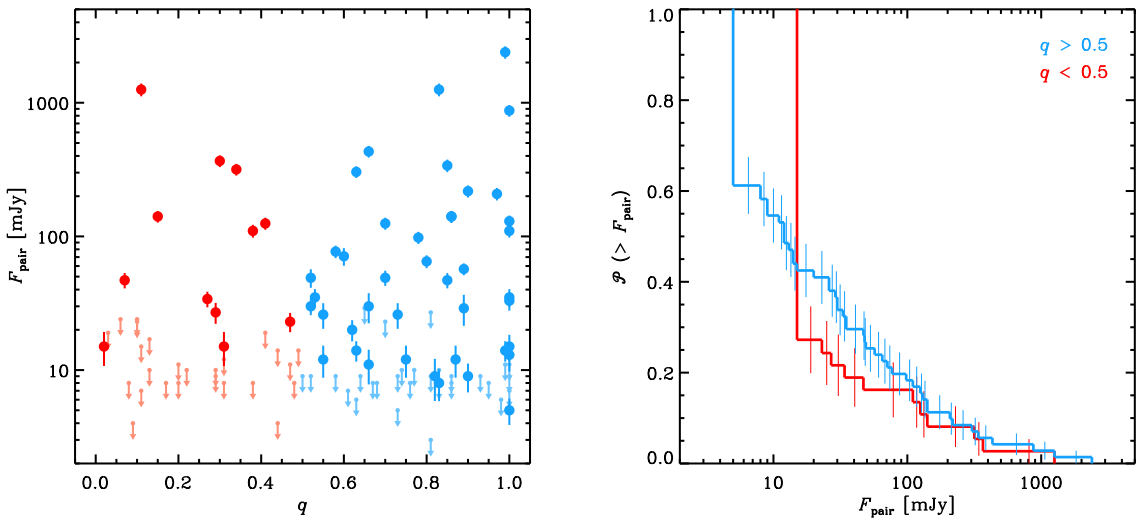

Figure 2.7: (*a*) A comparison of millimeter flux densities from potentially interacting pairs as a function of stellar mass ratio. For reference, the pair population is distinguished into high ($q > 0.5$; *blue*) and low ($q < 0.5$; *red*) mass ratio groups. (*b*) The cumulative distributions of millimeter flux densities for high and low mass ratio pairs, constructed with the Kaplan-Meier estimator to include the available upper limits. Millimeter luminosity depends only weakly on the stellar mass ratio.

larger dynamical perturbations to individual disks, producing more tidal stripping, and leading to lower disk masses and therefore less millimeter-wave emission. In that case, $F_{\rm pair}$ should be anti-correlated with q: higher mass ratio pairs should have fainter disk emission. No such trend is obvious in Figure 2.7*a*. If we separate the full population into high and low mass ratio pairs at some critical q_c, we find the largest difference between those sub-categories for $q_c = 0.5$. Figure 2.7*b* compares the cumulative distributions of the millimeter flux densities for high ($q > 0.5$; *blue*) and low ($q < 0.5$; *red*) mass ratio pairs, again with $\mathcal{P}_q(> F_{\rm pair})$ constructed using the Kaplan-Meier estimator to include the pairs that do not have detectable millimeter emission. The same two-sample tests employed above indicate a weak relationship between $F_{\rm pair}$ and q (see Table 2.9),

such that pairs with low stellar mass ratios have slightly less millimeter emission – the opposite of expectations from tidal interaction models. However, the evidence for any increase in the millimeter emission with higher stellar mass ratios is contained entirely in the relative detection ratios: a larger fraction of pairs with low q are not detected at millimeter wavelengths (see Figure 2.7*a*). If only the detected pairs are compared, the millimeter luminosity is found to be independent of q (see the K-S test results in Table 2.9). Moreover, this trend is present (and in fact enhanced) only for stellar pairs with wide separations: no clear relationship between $F_{\rm pair}$ and q exists for pairs with $a_p < 300\,{\rm AU}$ (see Table 2.9).

The absence of a firm connection between the millimeter luminosity and stellar mass ratio for smaller-separation pairs is consistent with the weak q-dependence predicted by tidal interaction models. Nevertheless, the correlation between $F_{\rm pair}$ and q for widely-separated pairs is compelling. Since star-disk interactions in these cases should be inherently less destructive, this trend might indicate a relationship between the millimeter luminosity and the absolute (and not relative) stellar masses in the pair. Indeed, Figure 2.8*a* demonstrates a marginal association between the millimeter luminosity and total stellar mass in Taurus pairs. Taking only the detections, we find a $\sim 3\,\sigma$ correlation between $F_{\rm pair}$ and $M_{\rm pair}$ (this improves slightly to $3.7\,\sigma$ if the labeled outliers are excluded). Figure 2.8*b* demonstrates that this relationship is not restricted to stellar pairs, but apparently also applies to *individual* stars, both isolated (single) cases and members of multiple systems. In the latter case, we have combined the component-resolved F_d estimates from Table 2.4 and the single star measurements from the literature (Table 2.7): the result is again a $\sim 3\,\sigma$ positive correlation ($4.5\,\sigma$ if SU Aur is excluded). It is worth noting that the M_* distributions for isolated stars and individual

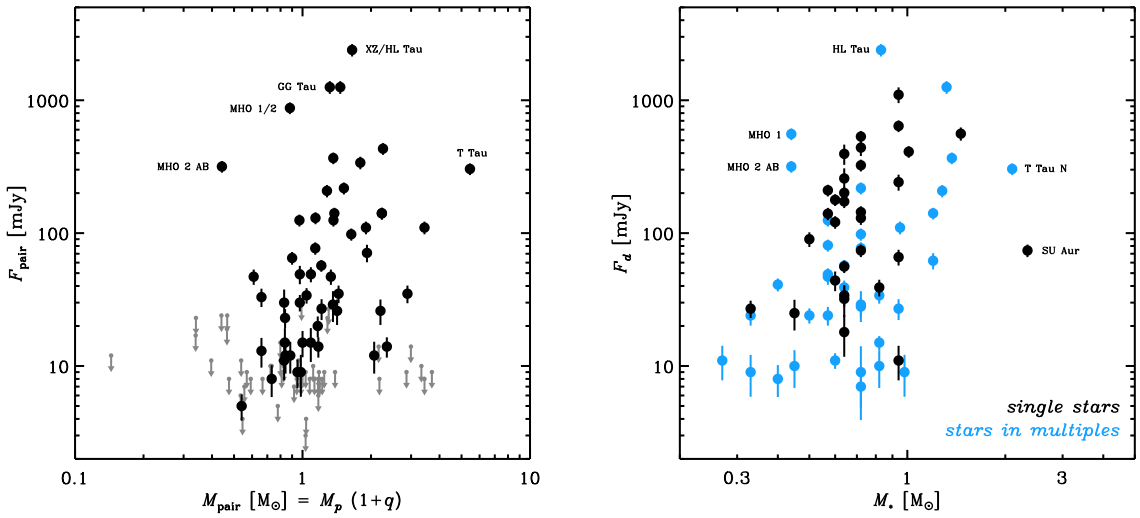

Figure 2.8: (*a*) Millimeter flux density as a function of the total mass of a stellar pair, where $M_{\rm pair} = M_p + M_s = M_p(1+q)$. (*b*) Millimeter flux densities as a function of stellar mass for the individual, detected stellar components in Taurus, for both single stars (*black*) and those in multiple systems (*blue*). Note that upper limits for non-detections are not shown in the right-hand panel.

stars in multiple systems are statistically indistinguishable. However, it is premature to draw any firm conclusions from these weak trends for two reasons: (1) the dispersion is large relative to the range of the trend, and (2) the stellar masses used here have large systematic uncertainties.

The demographic properties of stellar pairs discussed above are certainly informative, but they also naturally hide some characteristics of individual components that are available from this resolved survey. The two panels in Figure 2.9 are intended to compare the millimeter-wave luminosities from individual disk components *within* each stellar pair, as a function of their stellar host masses. Figure 2.9*a* directly compares the resolved 880 μm flux densities for each component in each pair. As mentioned

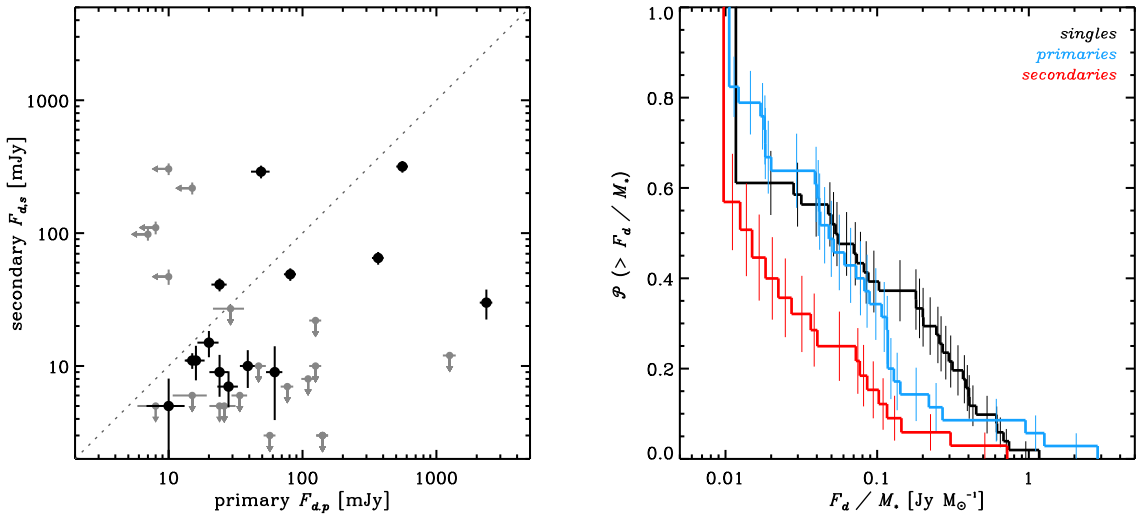

Figure 2.9: (*a*) The 880 μm flux densities for the primary and secondary components of each stellar pair. (*b*) The cumulative distributions of the ratio of millimeter-wave disk flux densities to their stellar host masses (a proxy for the disk:star mass ratio) for singles (*black*), primaries (*blue*), and secondaries (*red*), each constructed from the Kaplan-Meier product-limit estimator to include upper limits on F_d. Two-sample tests (see Table 2.9) demonstrate that these ratios are systematically lower for secondaries, implying that their disks are inherently less luminous regardless of the host masses.

in §2.5.1, the emission from the primary is usually more luminous than from the secondary. The exceptions above the dashed line are comprised of the widely-separated tertiary companions of close pairs and the UZ Tau Wab and FS Tau/Haro 6-5B pairs. The relative dominance of the primary disk emission is unaffected by the projected separation to a companion, and is typically more than would be expected if the amount of millimeter-wave disk emission scales linearly with the stellar host mass. This latter feature is shown more directly in Figure 2.9*b*, which compares the cumulative distributions of the ratio of the millimeter flux density to the stellar mass (akin to a disk:star mass

ratio) for singles, primaries, and secondaries. In some studies of disks around low-mass stars and brown dwarfs, this F_d/M_* ratio is found to be roughly constant; the weaker emission (or lower detection rate) is a manifestation of inherently lower host masses (e.g., Scholz et al. 2006; Schaefer et al. 2009). That implicit sensitivity threshold is not the case for the secondaries in our sample: the F_d/M_* ratio is systematically lower for secondaries compared to primaries and singles, with a probability that it is drawn from the same parent distributions as the primaries or singles of <0.008 (two-sample test results are compiled in Table 2.9). The results suggest that the millimeter-wave disk emission from the secondaries is inherently less luminous than around the primaries (or isolated stars), regardless of the stellar host mass.

2.5.3 Disk sizes and tidal truncation

A more direct test of dynamical predictions for star-disk interactions lies with our measurements of individual disk sizes. Theoretical models provide a way to estimate the truncated equilibrium tidal radii (R_t) for the disks around each component of a stellar pair given a few key orbital parameters, $\{a, e, q\}$, and some characterization of the viscous properties of the disk material (Artymowicz & Lubow 1994). Although they remain uncertain, there are reasonable ways to estimate stellar mass ratios (q) from optical/infrared measurements and pre-main sequence stellar evolution models (see the references in Table 2.6). However, the stellar pairs in this sample have wide enough projected separations that they are expected to have prohibitively long orbital periods and exhibit little apparent motion on reasonable time baselines for observations: therefore, we generally do not have any direct knowledge about their true orbital

separations (a) or eccentricities (e).

Nevertheless, we can construct a probabilistic model of R_t using only the *projected* physical separation of any pair, a_p (based on the projected angular separation, ρ, and assumed distance, d). Following Torres (1999), the ratio of the semimajor axis to the projected physical separation is

$$\mathcal{F} \equiv \frac{a}{a_p} = \frac{1-e^2}{1+e\cos\nu}\sqrt{1-\sin^2(\omega+\nu)\sin^2 i}, \tag{2.1}$$

where e is the eccentricity, ν is the true anomaly, ω is the longitude of periastron, and i is the orbital inclination relative to the observer (note that the ratio $\mathcal{F}$ is exact for binaries; we expect only modest deviations from it for well-separated hierarchical pairs). Since we do not know $\{\omega, i, e, \nu\}$ for any individual stellar pair, we have to construct a probability distribution for the true-to-projected separation ratios, $\mathcal{P}(\mathcal{F})$, using a Monte Carlo approach. To accomplish that, we assume that stellar pairs are not observed at any preferential orbital location and adopt uniform distributions for the orbital phase (or mean anomaly) and longitude of periastron (ω). The assumption of random viewing geometries suggests that the distribution of orbital inclinations (i) has a $\sin i$ dependence. However, inferring an appropriate functional form for the eccentricity (e) distribution (and by extension the distribution of true anomalies, ν) is more challenging.

There is little empirical information available to constrain the eccentricity distribution for the pre-main sequence binary population. Pairs with short orbital periods have low eccentricities ($e < 0.1$), due to the rapid tidal circularization of their orbits (Zahn 1977; Zahn & Bouchet 1989; Melo et al. 2001). At longer periods, the eccentricity distribution appears relatively uniform in the range $e \approx 0.1$-0.9 (Mathieu 1994). It is not clear if the apparent dearth of young stellar pairs with extreme (circular

or parabolic) eccentricities is real or an artifact of low-number statistics and selection effects. Based on their samples of main sequence field binaries, Duquennoy & Mayor (1991) and Tokovinin (1998) suggested an increasing eccentricity distribution, where $\mathcal{P}(e) \propto 2e$ (see also Ambartsumian 1937). However, the recent comprehensive survey of such systems by Raghavan et al. (2010) instead suggests that a flat eccentricity distribution is preferable for orbital periods of $\sim$10-10^5 days. Similar results are also noted for very low mass binaries (Dupuy & Liu 2011). Based on these more recent studies, we assume that the eccentricity distribution is uniform. For reference, Figure 2.10*a* illustrates the influence of different forms for $\mathcal{P}(e)$ on the shape of $\mathcal{P}(\mathcal{F})$.

Having established the infrastructure to derive a probabilistic model of the true orbital separation (a) given the observed projected separation (a_p), we can build on that to determine the distribution of tidal truncation radii, $\mathcal{P}(R_t)$, for a given stellar pair. Because of its relative simplicity, we adopt the semi-analytic approximations for truncated disk sizes based on the analysis of stable invariant loops by Pichardo et al. (2005). Using their formulation, the tidal radius is

$$R_t \approx 0.337 \left[\frac{(1-e)^{1.20}\ \varphi^{2/3}\ \mu^{0.07}}{0.6\,\varphi^{2/3} + \ln\left(1+\varphi^{1/3}\right)} \right] \mathcal{F}\ a_p\,, \tag{2.2}$$

where $\mu = q/(1+q)$ is the mass fraction of the stellar pair and φ is the mass ratio of the host star for which R_t is being calculated relative to its companion. For example, the truncation radius of the disk around the primary star is calculated with $\varphi = M_p/M_s = 1/q$, whereas the R_t for the disk around the secondary is determined by setting $\varphi = M_s/M_p = q$. For any pair in a multiple system, there is a direct measurement of a_p (or rather ρ, and an assumed distance) and an estimate of q (see Table 2.6). Fixing these quantities, we constructed the probability distribution $\mathcal{P}(R_t)$ that a component of

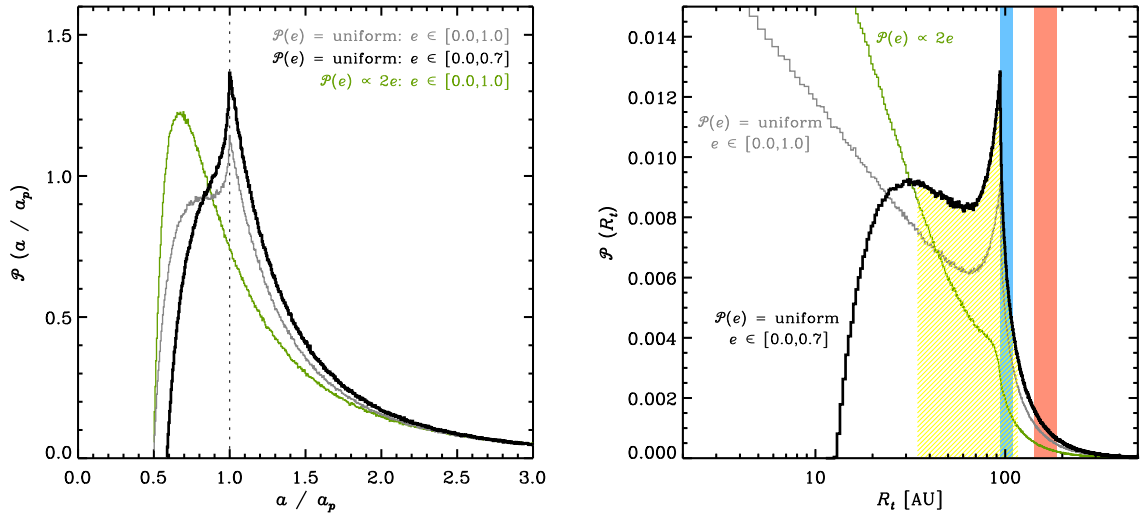

Figure 2.10: (a) Probability distributions for the ratio of true to projected separations, $\mathcal{P}(\mathcal{F})$ where $\mathcal{F} \equiv a/a_p$, using three different underlying eccentricity distributions. (b) An example probability distribution for the disk radii (R_t) expected in the HK Tau binary based on the tidal interaction models of Pichardo et al. (2005) for the same three assumed eccentricity distributions. The blue and red vertical bars represent the best-fit disk radii (and $1\,\sigma$ uncertainties) for HK Tau A and B, respectively, measured directly from the SMA visibilities in §2.4. The yellow filled area marks the region containing 68% of the probability for the $\mathcal{P}(R_t)$ with the favored eccentricity distribution (black curve; see text), used to determine the error bars in Figure 2.11.

the pair hosts a disk with a tidally truncated radius R_t using a Monte Carlo simulation with $\sim 10^7$ realizations of Equation 2.2, assuming the priors for the distributions of the orbital elements $\{\omega,\, i,\, e,\, \nu\}$ (and therefore $\mathcal{F}$) discussed above.

As an example, Figure 2.10*b* shows $\mathcal{P}(R_t)$ for the HK Tau binary, where $a_p = 340\,\mathrm{AU}$ and $q \approx 1$, for three representative assumptions about the underlying eccentricity distribution (note that the same R_t distribution applies to both components for this equal-mass stellar pair). The best-fit estimates of the disk radii from our modeling of the SMA data (see §2.4) are marked as red (HK Tau A) and blue (HK Tau B) vertical bars. Tidal interaction models predict that the disk sizes have a rather steep dependence on the orbital eccentricity (see Equation 2.2), which means that the assumption of an underlying $\mathcal{P}(e)$ that permits or favors high eccentricities will lead to the *general* prediction of very small disk sizes (gray or green curves in Figure 2.10*b*) and, therefore, low millimeter-wave luminosities. While such eccenticity distributions may be relevant for the general population of multiple systems, the luminosity-based selection criterion used to build our component-resolved SMA sample creates a strong bias that would exclude high-e pairs. With that bias in mind, we favor the use of a truncated eccentricity distribution to make comparisons between the measured and predicted disk radii; we assume $\mathcal{P}(e)$ is uniform for $e \in [0.0, 0.7]$ (black curves in Figure 2.10).

Figure 2.11 makes a direct comparison between the measurements of dust disk sizes (R_d) that were determined in §2.4 (see Tables 2.4 and 2.5) and the truncation radii (R_t) predicted by our probabilistic treatment of the Pichardo et al. (2005) models. The location of the points along the R_t axis (abscissae) correspond to the peaks of their $\mathcal{P}(R_t)$ distributions (for the assumed $\mathcal{P}(e)$ described above), and their asymmetric error bars encapsulate the central 68% of those probability distributions (see the shaded yellow

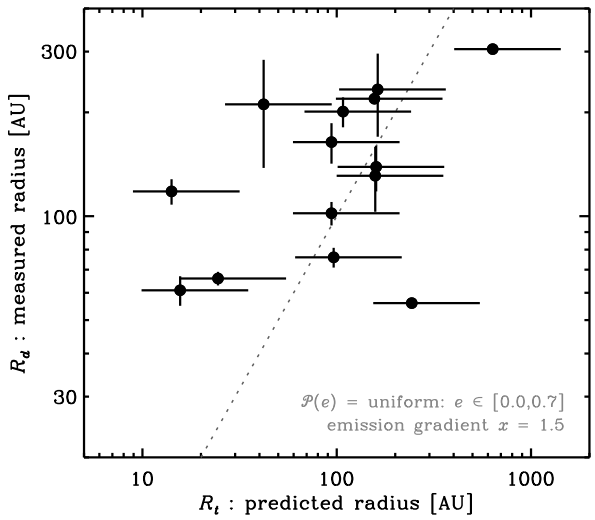

Figure 2.11: The measured disk radii (see Tables 2.4 and 2.5) compared with the expected disk radii based on a probabilistic treatment of the Pichardo et al. (2005) tidal interaction models, for an assumed underlying uniform eccentricity distribution truncated at $e = 0.7$ (see text).

region of Figure 2.10*b* for an example). Of the 14 disks with available R_d measurements, eight have sizes that are in good agreement with predictions from the tidal interaction models, two are smaller than expected (around GG Tau Aab and DK Tau A), and the remaining four are considerably larger. These decidedly mixed results for the Pichardo et al. (2005) model predictions could be at least partially ameliorated by introducing a term that incorporates viscosity into the interaction calculations, which would tend to increase R_t due to the viscous spreading of disk material (see Artymowicz & Lubow 1994). Quantitatively comparable shifts in the measured R_d values could be accomodated by permitting a range of emission gradients (x) in model fits to the observations. Reconciling the measured disk sizes with the predictions from tidal interaction models would require that the disk viscosity increases and/or the millimeter-wave emission gradient (x) decreases as a function of pair separation (a).

2.6 Discussion

We have carried out a luminosity and separation limited survey of the millimeter-wave dust continuum emission from the disks around individual components of 23 young multiple star systems in the ∼1-2 Myr-old Taurus-Auriga star formation region. With a simple morphological model, we fitted the continuum visibilities observed with the SMA interferometer to determine the luminosity and size of each individual disk in these systems. These component-resolved measurements were then coupled with a comprehensive database of millimeter-wave luminosities for *all* of the multiple systems in Taurus (with spectral types F0-M4) to estimate millimeter detection frequencies, evaluate the dependence of continuum emission levels on the separations and masses of companion stars, and make direct comparisons with predictions from tidal interaction models.

We find that roughly one third (28-37%) of the individual stars in multiple systems harbor disks with dust masses that are large enough to emit detectable millimeter continuum radiation (see §2.5.1). This low incidence rate is approximately half that for isolated single stars (62%), and does not depend on the number of stellar companions in the system. Similar disk frequencies have been inferred from accretion and infrared excess signatures (Cieza et al. 2009; Kraus et al. 2012), although without component-resolved diagnostics. Given these disk frequencies, it is clear that some *external* processes driven by the presence of a companion act to hasten the dispersal of circumstellar material in multiple systems at a level comparable to any *internal* disk evolution mechanisms (e.g., photoevaporation, grain growth, planet formation, etc.) on ∼1-2 Myr timescales.

Some basic demographic properties of stellar pairs in Taurus can provide new

insights into the mechanics of those external evolution processes. Building on the initial work by Jensen et al. (1994, 1996b), we have shown that the millimeter-wave luminosity from a pair of stars depends strongly on their (projected) separation (see §2.5.2). We identified substantial changes in the millimeter luminosity distributions of pair populations at discrete separations of 30 and 300 AU. Widely-separated pairs ($a_p > 300$ AU) have emission levels similar to single stars. Pairs with medium separations (a_p = 30-300 AU) are typically 5× fainter, with a lower overall detection fraction. Millimeter emission is rarely detected around pairs with small separations ($a_p < 30$ AU), representing at least another factor of ∼5 reduction in luminosity. We demonstrated that there is a weak tendency for pairs with comparable stellar masses (higher q) to have brighter millimeter emission, with the effect being considerably stronger for wider pairs. We suggested this is related to a marginal correlation between stellar mass and millimeter luminosity, although verifying that tentative trend is a challenge due to the systematic uncertainties involved in estimating stellar masses.

The relationship between millimeter luminosity and pair separation (Fig. 2.6) suggests that the external process relevant for the evolution of circumstellar material in multiple systems may be tied to tidal stripping from the outer regions of their constituent disks (e.g., Artymowicz & Lubow 1994). However, we found mixed results in a comparison of individual disk sizes that were measured (from the SMA data; §2.4) and predicted from tidal interaction models (see §2.5.3). Using a probabilistic treatment of orbital parameters, we showed that about half of the resolved disks in our sample have sizes that are consistent with the truncation predictions of the Pichardo et al. (2005) models. Most of the remainder have sizes that are substantially larger than expected, given the smaller projected separations to their companions (Fig. 2.11).

Analogous discrepancies have been noted regarding the observed and predicted inner edges of circumbinary rings (e.g., Beust & Dutrey 2005; Nagel et al. 2010). These results hint that *another* external process also shapes the circumstellar environments of young multiples. Further support for this additional evolutionary process is found in the observed distributions of circumstellar dust around individual stellar components. Tidal interaction models predict that disks should survive around both components of a pair, with their relative sizes roughly set by q (for a given a). However, Fig. 2.9 (see §2.5.2) demonstrates that this is often not the case. Roughly half of the multiple systems with detectable millimeter emission harbor only a single disk, usually around the primary component (or the wide tertiary in some hierarchical triples; e.g., HV Tau or Haro 6-37). Moreover, aside from a few exceptional counterexamples (see Fig. 2.6*a*), we find little millimeter-wave evidence for the circumbinary disks that should be common around pairs with small separations if tidal interactions were the sole external evolution mechanism.

To be fair, tidal interactions alone may still be able to explain many of these observed properties. The processes of stripping and truncation in pairs where the orbital and disk planes are misaligned has not yet been explored in detail (although see, e.g., Akeson et al. 2007; Verrier & Evans 2008), but might be substantially enhanced for some configurations. With limited orbital information, the prevalence of such misalignment is not known: but, there is some indication from polarization measurements that it is common (Jensen et al. 2004) and a number of specific examples have been identified (e.g., HK Tau or HD 98800; Duchêne et al. 2003a; Andrews et al. 2010). Moreover, it is important to keep in mind that the emission we have measured is only capable of probing the trace population of dust particles in these disks, and not their dominant mass reservoirs of molecular gas. The total disk masses that would be inferred from this

emission could be substantially under-estimated (see Andrews & Williams 2005, 2007a), as could the apparent disk sizes (e.g., Hughes et al. 2008; Panić et al. 2009; Andrews et al. 2012). Future complementary observations of emission line probes would help better address such uncertainties.

Alternatively, the disk properties we observe may be set at very early stages by the processes that regulate accretion during multiple star formation. Numerical simulations indicate that the ratio of the specific angular momenta of the infalling material ($j_{\rm gas}$) to the stellar pair (j_*) is fundamental in determining how the gas and dust accreted from a proto-system envelope is distributed among individual stellar components (Bonnell & Bate 1994; Bate & Bonnell 1997). If $j_{\rm gas} < j_*$, most of the infalling material will form a disk around the stellar primary. Conversely, if $j_{\rm gas} \geq j_*$, then a circum-secondary or circumbinary disk will dominate (see also Ochi et al. 2005). In the many cases with only circum-primary disk detections described above, the data are consistent with the former scenario. Similar millimeter-wave observations suggest that primary stars preferentially harbor more circumstellar material at the even earlier Class 0/I stages of protostellar evolution (e.g., Launhardt 2004; Patience et al. 2008, and references therein).

To summarize, there is a body of observational evidence suggesting that (at least) two fundamental processes related to the presence of stellar companions play significant roles in the evolution of circumstellar material in young multiple systems. The first is associated with the multiple star formation process itself, where the fraction of angular momentum associated with infalling material relative to that contained in the orbital motion of the stellar pair determines how circumstellar material is apportioned to each component. This is likely responsible for the pairs we observe with very large primary-to-secondary millimeter luminosity ratios. The second is a tidal interaction

process that strips material from any individual disks that survive the formation process. This is thought to be the origin of the millimeter luminosity – pair separation relationship.

At the typical ∼1-2 Myr age of Taurus-Auriga multiples, both of these evolution mechanisms have already made their mark on disk properties. The long-term fate of the circumstellar material in these multiple systems now rests with the same internal mechanisms that govern the subsequent evolution and dissipation of the disks around their isolated (single) counterparts. The formation and evolution of planets from this disk material are mechanisms of particular interest in these systems. The relatively straightforward, albeit uncertain, relationship between millimeter-wave luminosities and total disk masses enables at least a preliminary assessment of the likelihood of planet formation around individual components in multiple systems. Using the conversion advocated by Andrews & Williams (2005, 2007a) – which assumes optically thin, isothermal dust emission with a mean temperature of 20 K and (gas+dust) opacity of $0.034\,\mathrm{cm^2\ g^{-1}}$ at $880\,\mu$m – $F_d \approx 15$ mJy corresponds to a disk mass of $\sim 1\,\mathrm{M_{Jup}}$, and $F_d \approx 150$ mJy represents the standard estimate of the minimum mass of the solar nebula, $\sim 0.01\,\mathrm{M_\odot}$. Taking these conversions at face value, we would conclude that giant planets are unlikely to form around stars in close pairs (Fig. 2.6) or around the secondary components of most pairs with wider separations (Fig. 2.9). However, we would likewise infer that the primary components in wider pairs, the wide tertiaries in hierarchical triples, and perhaps the population of spectroscopic binaries should be just as likely to host giant planets as single stars.

Direct exoplanet searches of main sequence multiple systems in the field confirm these general expectations from the disk survey: planet formation is not severely inhibited

by the presence of a stellar companion (e.g., Patience et al. 2002; Raghavan et al. 2006; Duchêne 2010), and giant planets are preferentially found around primaries, the isolated components of hierarchical triples (Desidera & Barbieri 2007; Bonavita & Desidera 2007; Mugrauer & Neuhäuser 2009; Desidera et al. 2011), and perhaps even spectroscopic binaries (e.g., Doyle et al. 2011). That corroboration of results is a promising sign for planet formation studies in multiple systems, but the characterization of the disks around individual stellar components in these systems is still in its early stages. In the near future, we expect that new facilities like the Atacama Large Millimeter Array (ALMA) will shift the focus to study these individual disks in detail to directly compare their density structures and particle growth signatures with the disks around isolated (single) stars. Ultimately, such observations will help determine the impact of a nearby stellar neighbor on the planet formation process.

2.7 Summary

We have presented the results of an SMA imaging survey of the millimeter-wave (880 μm or 1.3 mm) thermal continuum emission from circumstellar dust in 23 young multiple systems in the Taurus-Auriga star-forming region. This census was designed to target relatively bright (>20 mJy at 880 μm) and well-separated ($\rho > 0\farcs3$) systems with primary spectral types between F0 and M4. We employed simple morphological models of the SMA visibilities to measure component-resolved millimeter luminosities and disk sizes whenever possible. Those results were considered together with a comprehensive literature compilation of the millimeter luminosities from *all* Taurus multiples (in this spectral type range) to better analyze how the presence of a stellar compaion affects

basic disk properties. Our primary conclusions are the following:

1. The millimeter detection frequency for individual stars in multiple systems is approximately 1/3 (28-40%), about half that for single stars (62%), and independent of the number of companions. These relative incidence rates suggest that the presence of a stellar companion plays a substantial *external* role in the early development and evolution of circumstellar material, at a level comparable to the standard *internal* disk evolution mechanisms that can operate in isolation (e.g., photoevaporation, particle growth, planet formation, etc.).

2. The millimeter luminosity from a pair of stars depends strongly on their projected separation (a_p), such that closer pairs are substantially fainter. We find natural breaks in the luminosity–separation plane at $a_p \approx 30$ and 300 AU. The luminosity distribution of wide pairs ($a_p > 300$ AU) is indistinguishable from that of single stars. Pairs with medium separations ($a_p = 30$-300 AU) are 5× fainter, and the very few close pairs ($a_p < 30$ AU) that we detect are 5× fainter yet – although a few bright circum*binary* disks represent notable exceptions.

3. There is no clear relationship between the millimeter luminosity from a pair and its stellar mass ratio (q) in general, but wide pairs with higher q tend to be brighter. We show that this latter behavior is produced by a marginal correlation between millimeter luminosities and stellar masses (both summed among pairs and for individual stars). However, the significance of this trend is questionable: the scatter is large, and there are substantial systematic uncertainties in estimating individual stellar masses that are not considered here. In nearly all cases, the primary component of a binary pair or the wide tertiary of a hierarchical triple harbors the

disk material that dominates the millimeter luminosity of the system (higher-order systems show a range of behavior, depending on the hierarchical nature of their pairings).

4. We find mixed results from a direct comparison of the disk sizes measured from the data and predicted from tidal interaction models, based on a probabilistic treatment of the orbital parameters for each system. Of the 14 resolved disks in our sample, the radii expected from the models described by Pichardo et al. (2005) are commensurate with the observed radii for eight disks; two others are found to be too small, and the remaining four are notably larger than would be expected given the relatively small (projected) distances to their companions.

5. These millimeter-wave observations suggest that at least two external mechanisms contribute to the evolution of circumstellar material in young multiple star systems. Star-disk tidal interactions strip material from the outer regions of individual disks, a process responsible for the strong dependence of the millimeter luminosity on the projected separation to a companion. We are lead to infer that accretion during the multiple star formation process itself also plays a substantial role in apportioning disk material, in many cases setting the initial disk masses such that primary stars harbor substantially more circumstellar material than their companions. The long-term prospects for (giant) planet formation in multiple systems are poor for stars in close pairings and around secondaries, but should be comparable to those around single stars for primaries, wide tertiaries in hierarchical triples, and perhaps around both components of very close spectroscopic binaries.

Chapter 3

Particle Growth in the Disks of the UZ Tauri Quadruple System

This thesis chapter has been submitted to the Astrophysical Journal and is under review.

Abstract

We present new, sensitive, high angular resolution ($\sim$0.1-0.5$''$) observations of the radio continuum emission from the UZ Tau quadruple star system at wavelengths of 0.88, 1.4, 2.9, 8.0, 9.8, and 50 mm. Emission is detected at all wavelengths toward the UZ Tau E spectroscopic binary and each component of the UZ Tau W close stellar pair, exhibiting thermal greybody spectra from dusty disks out to a wavelength of $\sim$1 cm. The emission at 5 cm, assumed to be of compact, non-dust origin, is used to estimate the contribution

of non-dust emission to the total emission at 8 and 9.8 mm. The dust emission from the UZ Tau E disk is well-resolved, although the emission morphology becomes notably more compact at longer wavelengths. Using a simple parametric modeling prescription, this size–wavelength anti-correlation is quantified through measurements of the radial optical depth profiles at each wavelength, and therefore the spatial variation of the disk colors across the millimeter-wave spectrum. There is robust evidence that the UZ Tau E continuum emission spectrum flattens with increasing proximity to the central binary, suggesting that the power-law index of the dust opacity spectrum β increases with disk radius. However, the data also suggest that the dust opacities in this part of the spectrum are not described well by a single power-law in frequency. We interpret this behavior as evidence for a substantial spatial variation in the particle size distribution, with a factor of $\gtrsim$10 increase in particle sizes across the disk. Comparisons with particle evolution models suggest that radial drift plays a more significant role than turbulent fragmentation in setting the particle size distribution.

3.1 Introduction

Most theoretical models of planet formation require that the solids in a circumstellar disk grow from sub-μm dust particles to >1000 km-scale planetesimals within a relatively brief timeframe ($\sim$1-5 Myr). The detailed evolution of disk solids involves an extraordinarily complex interplay between a diverse set of physical processes, including small-scale material effects (coagulation; e.g., Dominik & Tielens 1997; Okuzumi 2009), collision physics (e.g., Blum & Wurm 2008; Birnstiel et al. 2009; Zsom et al. 2010; Güttler et al. 2010), and aerodynamic effects caused by the turbulent reservoir of disk gas (e.g.,

Weidenschilling 1977; Brauer et al. 2008b; Windmark et al. 2012). Recently, theoretical studies that incorporate numerical simulations of these processes, informed by laboratory collision experiments, have been developed in an effort to better understand the growth and migration of solids in circumstellar disks (Birnstiel et al. 2010a, 2011, 2012b). Further progress along these lines requires the use of direct astronomical observations of dust in these disks to test, calibrate, and refine those models (e.g., Birnstiel et al. 2010b, 2012a; Ricci et al. 2011b; Pinilla et al. 2012b).

The best available constraints on the particle size distribution in a disk come from observations of thermal continuum spectra from (sub)mm to cm wavelengths (Weintraub et al. 1989; Beckwith & Sargent 1991). This emission has low optical depths, with an intensity profile $I_\nu \propto \tau_\nu \, B_\nu(T)$, where τ_ν and T are the dust optical depth and temperature, respectively (both vary with location in the disk). The spectral morphology of this emission is set by both the local grain temperatures (through the Planck function, B_ν) and opacities, κ_ν (note that $\tau_\nu = \kappa_\nu \, \Sigma$, where Σ are the surface densities). For long wavelengths or warm temperatures, the Rayleigh-Jeans limit applies and the emission spectrum varies like $I_\nu \propto \nu^2 \, \kappa_\nu$. The information on dust particle sizes (and composition) is encapsulated in the opacity spectrum, κ_ν. For a single particle of radius a, κ_ν is roughly constant in the geometric optics limit ($\lambda \ll a$), has a broad peak in a resonance regime ($\lambda \sim a$), and then falls off as λ^{-2} in the Rayleigh scattering regime ($\lambda \gg a$). And for a distribution of particle sizes $n(a)$, the composite opacity corresponds to the distribution-weighted average of the individual particle opacities. For many reasonable particle mineralogies and size distributions, the opacity spectrum can be described well by a power-law at the low frequencies probed by radio observations: $\kappa_\nu \propto \nu^\beta$. In principle, the spectral index β can be used to constrain $n(a)$ and learn about particle

growth: for a top-heavy $n(a)$, the geometric optics regime becomes more relevant at longer wavelengths, causing β to decline (Miyake & Nakagawa 1993; Stognienko et al. 1995; Henning & Stognienko 1996; D'Alessio et al. 2001; Draine 2006). In short, particle growth decreases β and should flatten the mm/cm-wave continuum spectrum.

Multi-wavelength radio photometry observations of disks are consistent with significant particle growth, such that disk-averaged spectral indices are much lower ($\beta \approx$ 0-1; Beckwith & Sargent 1991; Natta & Testi 2004; Andrews & Williams 2005; Wilner et al. 2005; Rodmann et al. 2006; Ricci et al. 2010a,b, 2011a) than in the diffuse or molecular interstellar medium ($\beta \approx$ 1.7-2.0; Hildebrand 1983; Henning et al. 1995; Goldsmith et al. 1997; Finkbeiner et al. 1999; Li & Draine 2001). Following the analysis of Draine (2006), these β values suggest particle growth to *at least* $\sim$mm-cm sizes has occured in disks on $\sim$1 Myr timescales. However, these unresolved spectral measurements provide only limited constraints for particle evolution models. Furthermore, unresolved observations do not allow distinguishing between genuinely low β and merely high disk-averaged optical depth. In principle, resolved interferometric observations of the mm/cm-wave spectrum can probe how the particle size distribution varies spatially in the disk, which can be used to refine the theoretical models of particle collisions (growth efficiency) and migration (i.e., radial drift). Observational inferences of radial variations in the opacity spectrum, $\beta(r)$, have only recently become possible. Banzatti et al. (2011) resolved the disk around CQ Tau at multiple wavelengths between 880 μm and 3.6 cm and found marginal evidence for a radial decrease in β interior to 60 AU. Isella et al. (2010) studied the DG Tau and RY Tau disks at 1.3 and 2.9 mm, and placed an upper limit to the spatial variation of their opacity indices, $\Delta\beta \leq 0.7$, inside $\sim$100 AU. With similar observations, Guilloteau et al. (2011) claimed that $\beta(r)$ was not

constant between 1.3 and 2.7 mm for six additional disks in the Taurus region. Ideally, this kind of analysis would be performed on resolved measurements for a large range of observing wavelengths, to maximize the spectral leverage. Recently, Pérez et al. (2012) achieved the most robust detection to date of an increasing $\beta(r)$ in the AS 209 disk, using resolved data at wavelengths of 880 μm, 2.9 mm, 8.0 mm, and 9.8 mm as part of the "Disks@EVLA" project (Chandler et al., *in preparation*).[1]

To build on these recent results, we study new spatially resolved interferometric observations of the individual disks in the UZ Tau multiple star system. UZ Tau is a hierarchical quadruple system in the Taurus region ($d \approx 145$ pc; Loinard et al. 2007; Torres et al. 2007, 2009) composed of two binary pairs (Joy & van Biesbroeck 1944). The primary, UZ Tau E, is a double-lined spectroscopic binary with a 19 d period (Mathieu et al. 1996), well-separated (3.″6) from the secondary, UZ Tau W, itself a close binary (0.″3; Simon et al. 1992; Ghez et al. 1993). Beckwith et al. (1990) first identified mm-wave dust emission from the system, which was subsequently resolved and associated with a bright circumbinary disk around UZ Tau E, as well as a fainter, unresolved contribution from the UZ Tau W binary (Jensen et al. 1996b; Dutrey et al. 1996; Simon et al. 2000). Subsequently, Harris et al. (2012) resolved the UZ Tau W emission into individual disk components centered on each star in the binary (see Chapter 2). The UZ Tau system is an interesting target for resolved studies of its radio spectrum: the primary disk is bright and extended, and the secondary disks are sufficiently separated to provide new information on how particle growth is affected by the presence of stellar companions. Rodmann et al. (2006) claimed evidence for large (cm-sized) particles in the UZ Tau

[1] `https://safe.nrao.edu/evla/disks/`

system, using marginally resolved observations at $\lambda = 7\,\mathrm{mm}$: they measured $\beta \approx 0.8$ averaged over all three disks in the system.

In this Chapter, we present observations of the UZ Tau system at $\lambda = 0.88$, 1.4, 2.9, 8.0, 9.8, and 50 mm as another contribution from the "Disks@EVLA" project. Using data from the Submillimeter Array (SMA), Combined Array for Research in Millimeter Astronomy (CARMA), and the Karl G. Jansky Very Large Array (VLA), we measure the radial variation of mm/radio colors in the UZ Tau E disk and provide constraints on the mm/radio spectra from each disk in the UZ Tau W binary. In §3.2, we describe the observations and data calibration. In §3.3, we outline the adopted modeling techniques. The modeling results are presented in §3.4, and then discussed in the context of particle evolution models in §3.5. A summary of our principal conclusions is provided in §3.6.

3.2 Observations and Data Reduction

3.2.1 SMA observations at 0.88 mm (340 GHz)

UZ Tau was observed with the SMA interferometer (Ho et al. 2004) on Mauna Kea, Hawaii at 0.88 mm in three different array configurations: compact (C; 6-70 m baselines) on 2010 Nov 4, extended (E; 16-70 m baselines) on 2011 Feb 17, and very extended (V; 68-509 m baselines) on 2010 Feb 18 and Mar 2. The observations were conducted in good weather conditions, with stable phases and low precipitable water vaper (PWV) levels (<2 mm). The correlator was configured to process two 2 GHz-bandwidth intermediate frequency (IF) bands for each of two receiver sidebands (a total bandwidth of 8 GHz), centered at ± 5 GHz and ± 7 GHz from the local oscillator (LO) frequency, 340.755 GHz.

Each IF+sideband combination comprised 24 slightly overlapping spectral chunks of 104 MHz width, divided into 32 channels each: a single chunk reserved for the CO J=3−2 transition was divided into 256 channels (these CO data will be presented elsewhere). The observations cycled between UZ Tau and the quasars 3C 111 and J0510+180 in a 10-20 minute cycle, depending on the array configuration. These SMA observations were originally presented by Harris et al. (2012).

The visibility data from each observation were calibrated independently with the `MIR` package. The spectral bandpass response was determined from observations of the quasars 3C 279 and 3C 454.3. The absolute amplitude scale was bootstrapped from observations of Uranus and Ganymede, with an estimated systematic uncertainty of ∼10%. A complex gain calibration was determined from observations of the nearby quasar 3C 111. The calibrated data were spectrally averaged to form multiple continuum datasets, which were subsequently combined. This composite set of visibilities was then Fourier transformed with natural weighting, deconvolved with the `CLEAN` algorithm, and restored with a $0\farcs43 \times 0\farcs31$ (P.A. = 49°) synthesized beam using the `MIRIAD` package.

3.2.2 CARMA observations at 1.4 and 2.9 mm (217 and 103 GHz)

The 15-element CARMA interferometer near Big Pine, California was used to observe UZ Tau at 217 GHz (1.4 mm) in the C (26-370 m baselines), B (82-946 m baselines), and A (150-1883 m baselines) configurations on 2007 Oct 27, 2009 Dec 10, and 2011 Dec 9, respectively, and at 103 GHz (2.9 mm) in the C and B configurations on 2010 Mar 24 and 2009 Dec 17, respectively. The observations were conducted in good

weather, with stable phases and PWV less than 2 mm at 217 GHz (<1.5 mm in the A array) and in the B configuration at 105 GHz; the 105 GHz data in the C configuration had PWV <4 mm. These data were obtained over the course of an expansion in the CARMA correlator capabilities, and therefore have different spectral configurations. The 2007 C configuration data were collected in two 468 MHz-wide sub-bands per sideband, each composed of 15 spectral channels and centered around a mean frequency of 225.6 GHz (these were the data presented by Isella et al. 2009). The 2009 and 2010 C and B configuration data utilized a third 468 MHz-wide sub-band in each sideband, with mean frequencies of 225.7 and 103.2 GHz. The 2011 A configuration observations were conducted with a total of 8 GHz of bandwidth, employing eight 494 MHz (partly overlapping) sub-bands in each sideband, centered around the LO frequency of 214.6 GHz. The composite datasets have mean frequencies of 217.4 and 103.2 GHz (computed from the naturally weighted average of the visibilities), corresponding to effective wavelengths of 1.38 and 2.90 mm. In all cases, we interleaved observations of UZ Tau with 3C 111, J0336+323, and J0510+180 in a 5-20 minute cycle, depending on the available baseline lengths.

The `MIRIAD` package was used to calibrate each individual visibility dataset independently. Observations of the bright quasar 3C 84 were employed to calibrate the spectral bandpass response, and measurements of Uranus were used to bootstrap the amplitude scale, with an approximate uncertainty of ∼10%. Complex gain variations induced by atmospheric and instrumental effects were corrected using observations of J0510+180 or 3C 111. Once calibrated, the visibilities in each spectral window were averaged. After correcting for small proper motions at each epoch and checking for consistency on overlapping baselines and between spectral sub-bands, all of the data

for a given observing frequency were combined into a composite visibility dataset. The 1.4 mm visibility set was then Fourier inverted with natural weighting, deconvolved with the `CLEAN` algorithm, and then restored with a $0\farcs21 \times 0\farcs17$ (P.A. = 83°) synthesized beam. To achieve comparable resolution, the composite 2.9 mm visibility set was Fourier inverted using Briggs weighting with the robust parameter set to zero, deconvolved, and restored with $0\farcs75 \times 0\farcs55$ (P.A. = 75°) synthesized beam.

3.2.3 VLA observations at 8.0, 9.8, and 50 mm (37.5, 30.5, and 6.0 GHz)

The UZ Tau disks were also observed with the VLA as part of the "Disks@EVLA" program in the Ka band with the C (45-3400 m baselines), B (0.24-11 km), and A (0.68-36 km) array configurations on 2010 Nov 1, 2011 Mar 19, and 2012 Nov 4-7, respectively. The correlator was configured with two 1 GHz-wide IF bands centered at 30.5 and 37.5 GHz (9.8 and 8.0 mm), with each divided into eight 128 MHz sub-bands composed of 64 channels. The observations were conducted in good conditions with low atmospheric optical depth ($\tau \approx 0.03$ at 34 GHz) and good phase stability. Additional observations in the C band were conducted with the D (35-1000 m baselines) and A array configurations on 2010 Jul 11 and 2011 Jul 23, respectively. The two available 1 GHz-wide IF bands were designed to continuously span sky frequencies from 5 to 7 GHz in the D configuration observations, but were centered slightly apart at 4.5 and 7.5 GHz when we observed in the A configuration (in both cases, the mean wavelength is 5 cm). For both the Ka and C band, the observations of UZ Tau were interleaved with the nearby quasar J0431+2037 on a ∼3 and 10 minute cycle, respectively.

The visibilities for each dataset were iteratively calibrated and flagged for interference and bad pointing, and subsequently imaged using the `CASA` package. After removing radio frequency interference and other corrupted data, observations of 3C 84 were used to calibrate the bandpass response. The spectral morphology of 3C 84 is not flat, but varies significantly across the widely separated individual sub-bands (relative to the observing frequency). To account for the shape of the 3C 84 spectrum, we bootstrapped its flux density in each sub-band from observations of the amplitude calibrator 3C 286, fit a power-law model to its spectrum, and then used that model to compute the bandpass response and calibrate the observations of the other sources. After bandpass calibration, the Ka band data were spectrally averaged, giving eight 128 MHz-wide pseudo-continuum channels for each IF band. To minimize bandwidth smearing, the C band visibilities were not spectrally averaged. The observations of J0431+2037 were used to calibrate the complex gain variations, and the amplitude scale was determined from observations of the well-monitored quasar 3C 286. Because 3C 286 is resolved in all but the most compact VLA configuration, a catalogued source model was used for this calibration, with the flux density scaled as appropriate to each sub-band. The estimated uncertainty in the amplitude scale is $\sim$10% at Ka band and $\sim$5% at C band.

Although the calibrations performed for the Ka and C band visibilities were similar, the imaging and deconvolution procedures differed slightly. After calibration, the Ka band data were Fourier inverted with natural weighting and then deconvolved using the multi-frequency synthesis version of the `CLEAN` algorithm with two Taylor terms to account for the flux variation of the source across each sub-band. The 37.5 GHz and 30.5 GHz IF band images were restored with $0\farcs18 \times 0\farcs14$ (P.A. = 131°) and $0\farcs20 \times 0\farcs14$ (P.A. = 134°) synthesized beams, respectively. For the C band data, extra care had

to be taken in the imaging process. At low frequencies, the primary beam of the VLA antennas is large (at C band, $\sim 8'$), and for any given field there are a number of very strong sources present in the field of view. Failure to `CLEAN` a strong source, even in the sidelobes of the primary beam, will leave residual sidelobes in the image center. Five sources within the field were strong enough to create imaging artifacts near the field center, so faceting was done on these sources to simultaneously deconvolve their outlying fields and the center of the primary beam. With these important caveats, the remainder of the C band imaging was analogous to the Ka band. A multi-frequency synthesis imaging and deconvolution that combines the D and A array data resulted in a naturally weighted 6 GHz ($\lambda = 5$ cm) map with a $0\farcs64 \times 0\farcs36$ (P.A. = 141°) synthesized beam.

3.2.4 Final data products

Figure 3.1 shows a continuum emission map gallery of the UZ Tau system at six different radio wavelengths. Each map was created with natural weighting of the visibilities, with the exception of the CARMA $\lambda = 2.9$ mm data (see §3.2.2). Emission from UZ Tau E and W are clearly detected at all six wavelengths, from $\lambda = 0.88$ to 50 mm. The UZ Tau E emission is resolved in all cases, although only marginally so in the VLA C band map (bottom panel). Both of the individual components in the UZ Tau W binary exhibit distinct emission peaks in each map, with the exception of the comparatively low-resolution CARMA $\lambda = 2.9$ mm data. The continuum emission centroid for UZ Tau E is located at $\alpha = 04^{\rm h}32^{\rm m}43\fs08$, $\delta = +25°52'30\farcs8$ (J2000), with an accuracy of $\sim 0\farcs1$. Relative to the UZ Tau E position, the UZ Tau Wa peak (the southern component of the UZ Tau W binary) lies $3\farcs60$ away at P.A. = 274°, and the UZ Tau Wb peak is found at

a distance of 3.″56 at P.A. = 279°. The emission peaks associated with UZ Tau Wa and Wb are separated by 0.″33, with P.A. = 12° (measured from Wa to Wb, E of N). The separation and orientation of the UZ Tau E–W pairing is consistent with the historical stellar astrometry, but a comparison between the orientation of the Wa–Wb continuum peak centroids and the infrared measurements of their stellar positions by White & Ghez (2001) suggests ∼10° of rotation (counter-clockwise in the plane of the sky) over the past ∼15 years, consistent with the shift expected in a Keplerian orbit with semimajor axis given by the projected separation of UZ Tau Wa–Wb. The relative positions of the radio centroids are consistent with a more recent image of the UZ Tau stars in the *Hubble Space Telescope* archive (taken with the F165LP filter and the ACS instrument on 2007 Aug 15: proposal ID 10840, PI N. Calvet).

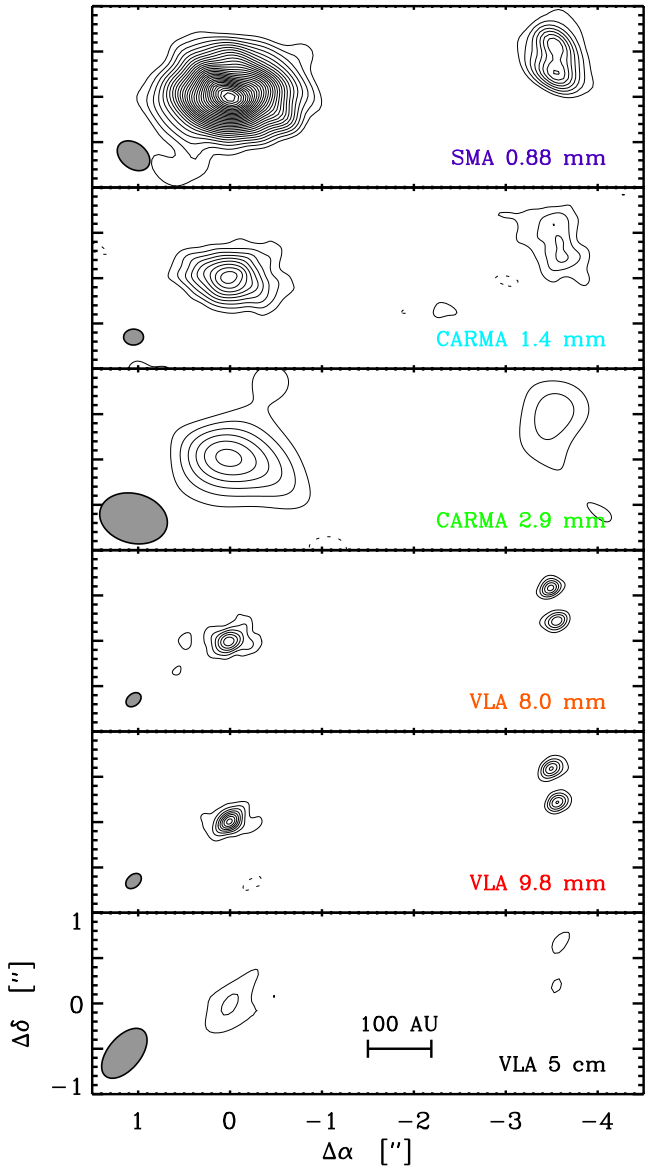

Figure 3.1: Synthesized images of the dust continuum emission from disks in the UZ Tau system at six different (sub)mm–radio wavelengths. Contours for each map except for that at 0.88 mm are drawn at $3\,\sigma$ intervals. The contour levels for the 0.88 mm map start at 5σ and increment by 2σ. RMS noise levels are provided in Table 3.1. The synthesized beam dimensions are shown in the lower left corner of each panel. A scale bar is marked in the bottom panel: each map spans 870×290 AU.

Table 3.1 lists the basic image properties for the maps in Figure 3.1, and Table 3.2 includes measurements of the peak and integrated flux densities for each of the emission components. The latter were determined from the visibility modeling procedures we will describe in §3.3. Figure 3.2 compares the radio continuum spectra for each component in the UZ Tau system: a description of the technique used to extract photometry from the partially blended UZ Tau W pair is provided in §3.3.4. All three emission components in the system are dominated by a thermal greybody spectrum from dust at $\lambda \leq 1\,\mathrm{cm}$, although there is some curvature at the shortest wavelengths for UZ Tau E and Wb that could be produced by low dust temperatures and/or high optical depths. At the longest radio wavelengths, the spectra start to increase and appear to be dominated by non-dust emission (presumably free-free radiation from stellar winds; e.g., Chiang et al. 1996; Pascucci et al. 2012). To quantify that behavior, we performed simple fits to the radio spectra for a model composed of a linear combination of two power-laws in wavelength (shown as dashed curves in Fig. 3.2): $F_\nu = a\lambda^{-\alpha_d} + b\lambda^{-\alpha_{nd}}$, where the indices α_d and $\alpha_{nd} \approx -0.1$ represent the spectral slopes in the dust and non-dust dominated regions of the spectrum, respectively. We find $\alpha_d \approx 2.90$, 2.23, and 2.30 ± 0.05 for UZ Tau E, Wa, and Wb, respectively, in agreement with results of Rodmann et al. (2006) for UZ Tau E.

Table 3.1. Properties of Synthesized Images

λ (mm)	beam size ($''\times''$)	beam P.A. ($^\circ$)	map RMS (mJy beam^{-1})
0.88	0.43×0.31	49	0.9
1.4	0.21×0.17	83	0.5
2.9	0.75×0.55	75	0.6
8.0	0.18×0.14	131	0.014
9.8	0.20×0.14	134	0.010
50	0.65×0.30	142	0.014

Table 3.2. Peak and Integrated Flux Densities

Component	λ (mm)	peak I_ν (mJy beam^{-1})	integrated F_ν (mJy)	Component	λ (mm)	peak I_ν (mJy beam^{-1})	integrated F_ν (mJy)
UZ Tau E	0.88	51.9 ± 1.5	375.0 ± 10.0	UZ Tau Wa	0.88	17.5 ± 0.9	35.9 ± 1.3
	1.4	13.8 ± 0.6	135.0 ± 5.0		1.4	2.0 ± 0.5	14.3 ± 2.9
	2.9	13.3 ± 0.8	21.6 ± 1.0		8.0	0.22 ± 0.02	0.32 ± 0.02
	8.0	0.27 ± 0.02	0.76 ± 0.07		9.8	0.15 ± 0.01	0.19 ± 0.01
	9.8	0.24 ± 0.01	0.36 ± 0.03		50	0.04 ± 0.01	···
	50	0.07 ± 0.02	0.11 ± 0.02				
UZ Tau Wb	0.88	16.4 ± 0.9	40.2 ± 1.8	UZ Tau Wa+Wb	2.9	5.7 ± 0.8	6.4 ± 0.8
	1.4	4.7 ± 0.5	30.7 ± 2.7				
	8.0	0.25 ± 0.02	0.32 ± 0.02				
	9.8	0.15 ± 0.01	0.21 ± 0.01				
	50	0.05 ± 0.01	···				

Notes to Table 3.2: Peak flux densities are measured directly from the maps shown in Figure 3.1. Except for the C band ($\lambda = 5\,\mathrm{cm}$), integrated flux densities are derived from the outcome of the modeling process described in §3.3 and 3.4. The C band properties were measured from the maps in Figure 3.1: since the emission from UZ Tau Wa and Wb is consistent with two point sources, we do not list separate integrated flux densities. The emission from the western pairing of UZ Tau Wa and UZ Tau Wb is not resolved at 2.9 mm; we therefore report the composite flux for the pairing at this wavelength.

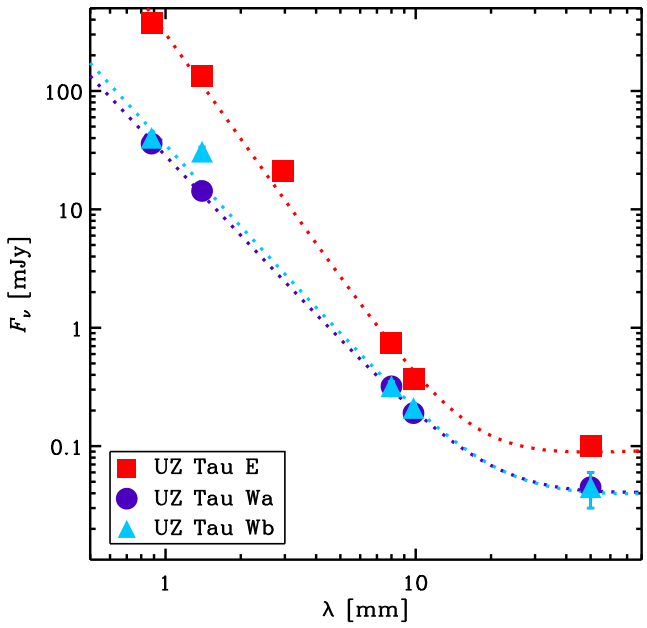

Figure 3.2: The spatially-integrated (sub)mm–radio continuum spectra for each UZ Tau emission component: flux densities and uncertainties are derived in §3.4, and listed in Table 3.2. Error bars are drawn, but are typically smaller than the datapoints. Dashed curves mark simple double power-law fits to the data: they suggest that the emission at shorter wavelengths ($\leq 1\,\mathrm{cm}$) is dominated by optically thin greybody dust emission, while there is a significant non-dust (presumably free-free emission or synchrotron flares) contribution at the longest wavelengths.

Given its large spatial extent and clear separation from its companions, the circumbinary disk around UZ Tau E will be the primary focus here. Perhaps the most striking feature of the UZ Tau E disk in Figure 3.1 is the apparent decrease in the continuum emission *size* as a function of observing wavelength. That size-wavelength trend is somewhat difficult to quantify in the image plane due to the different synthesized beam sizes, but it is manifest more clearly in Figure 3.3, which shows the deprojected, azimuthally-averaged visibility profiles at each wavelength. These were constructed after subtracting models for the UZ Tau W disks (see §3.3.4), assuming that the UZ Tau E disk had an inclination $i = 56°$ and major axis P.A. $= 86°$ (Simon et al. 2000), and normalized by their integrated flux densities (see Table 3.2). In this representation, an unresolved point source would have unit flux density at all baselines (a horizontal line), while increasingly resolved (larger) sources have steeper decreases in their visibility profiles, assuming they are properly described by a continuous disk-like morphology. Figure 3.3 unequivocally demonstrates that the UZ Tau E continuum emission morphologies are more compact (less resolved) at longer wavelengths.

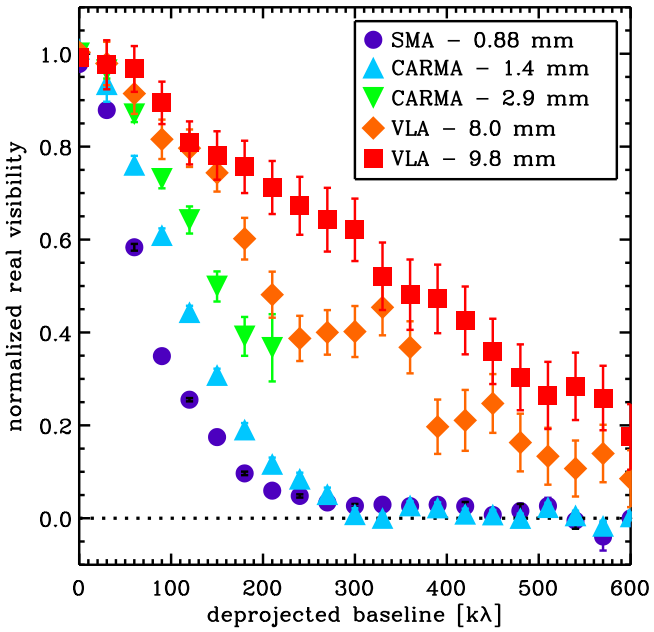

Figure 3.3: The normalized (real) visibility amplitudes for the UZ Tau E emission at each (sub)mm–radio wavelength, azimuthally-averaged and deprojected according to the disk viewing geometry, as a function of baseline length (within the noise, the imaginary amplitudes are all consistent with zero). There is a clear, monotonic progression in the visibility profiles as a function of wavelength, such that longer wavelengths have more compact (less resolved) distributions. This effect is noted in Figure 3.1, but here there is no potential for confusion from the different synthesized beam sizes. The data are binned into overlapping 60 kλ bins.

3.3 Modeling Analysis

Having presented the multi-wavelength radio observations of the UZ Tau disks, and shown that the UZ Tau E disk exhibits a trend of more compact emission morphologies at longer wavelengths, we turn to a modeling analysis of the continuum visibilities to better characterize the emission properties. Our goal is to use the observations to quantify how the (sub)mm–radio spectral shape (or color) *varies with location* in the UZ Tau E disk. First, we establish an underlying physical motivation for our modeling scheme (§3.3.1). Then, we describe the parametric modeling approach that is couched in those motivations (§3.3.2) and the method utilized for parameter estimation (§3.3.3). Finally, we address some of the caveats and assumptions in our technique, in particular the model subtraction of emission from the UZ Tau W binary and the treatment of radio contamination from non-dust emission mechanisms (§3.3.4). The modeling results are presented in §3.4.

3.3.1 Physical motivation

The thermal continuum emission from a protoplanetary disk is determined by the local dust temperatures (T) and densities (ρ). For a simple two-dimensional axisymmetric structure model in cylindrical coordinates (r, z), the densities can be characterized by

$$\rho(r,z) = \frac{\Sigma}{\sqrt{2\pi}H} \exp\left[-\frac{1}{2}\left(\frac{z}{H}\right)^2\right], \tag{3.1}$$

where Σ is a radial surface density profile and H is a radial scale height profile. The functional form in Eq. 3.1 is appropriate for well-mixed dust (i.e., a constant dust-to-gas mass ratio, ζ, at all locations) in a vertically isothermal gas disk in hydrostatic

equilibrium. In that case,

$$H = \frac{c_s}{\Omega} = \left(\frac{k_B T}{\mu m_H} \frac{r^3}{G M_*} \right)^{1/2}, \tag{3.2}$$

where c_s is the sound speed, Ω the Keplerian angular velocity, k_B the Boltzmann constant, G the gravitational constant, M_* the stellar mass, μ the mean molecular weight, and m_H the mass of a hydrogen atom. In this formalism, the disk structure is defined by the radial profiles Σ and T. For the former, we adopt the self-similarity solution for a thin, Keplerian accretion disk with a time-independent, power-law viscosity profile (Lynden-Bell & Pringle 1974; Hartmann et al. 1998),

$$\Sigma = \Sigma_c \left(\frac{r}{r_c} \right)^{-\gamma} \exp \left[- \left(\frac{r}{r_c} \right)^{2-\gamma} \right], \tag{3.3}$$

with characteristic radius r_c, gradient γ, and normalization $\Sigma_c = e\ \Sigma(r = r_c)$, where e is the base of the natural logarithm. The Σ parameterization in Eq. 3.3 has been used to successfully model both gas and dust emission from many protoplanetary disks (e.g., Kitamura et al. 2002; Hughes et al. 2008; Andrews et al. 2009, 2010, 2011; Isella et al. 2009, 2010; Guilloteau et al. 2011). For the temperature profile, we assume a simple radial power-law,

$$T = T_{10} \left(\frac{r}{10\ \mathrm{AU}} \right)^{-q}, \tag{3.4}$$

where T_{10} is the temperature at 10 AU, and q is a gradient parameter.

Observationally, the continuum intensity distribution, I_ν, is determined by integrating the radiative transfer equation along a given line of sight, s (defined by the disk viewing geometry),

$$I_\nu = \int_0^\infty K_\nu(s) S_\nu(s) e^{-\tau_\nu(s)} ds, \tag{3.5}$$

where $S_\nu(s)$ is the source function, $K_\nu(s)$ the absorption coefficient, and $\tau_\nu(s) = \int_0^s K_\nu(s') ds'$ is the line-of-sight optical depth. We assume thermal emission, where

$S_\nu = B_\nu(T)$, the Planck function at the local temperature. The absorption coefficient (and therefore optical depth) is defined as

$$K_\nu = \zeta \ \kappa_\nu \ \rho, \tag{3.6}$$

where the mass absorption coefficient κ_ν represents the dust grain opacity spectrum.

Typically, modeling studies of continuum emission from protoplanetary disks greatly simplify Eq. 3.6 (or its equivalent) by assuming a spatially invariant opacity spectrum. However, numerical simulations of the collisional evolution of dust particles indicate that κ_ν varies with radius: for example, the Birnstiel et al. (2011) recipe for computing particle size distributions suggests that the (sub)mm–radio opacity spectrum behaves roughly like a radial power-law,

$$\kappa_\nu \propto r^\xi, \tag{3.7}$$

with an index ξ (usually positive) determined by the gas density and temperature profiles, the disk turbulence, and the material properties of the grains (i.e., the fragmentation velocity).[2]

3.3.2 Parametric approach

The essence of the model used to describe these multi-wavelength observations is encapsulated in Eq. 3.6, which describes the radial and spectral variation of the absorption coefficient, or equivalently the product $\kappa_\nu \times \rho$. To make an analogy with single-wavelength disk models, it helps to think of a parametric version of that expression

[2]Other factors, particularly the efficiency of radial drift, can have an important impact on $\kappa_\nu(r)$ (i.e., ξ) as well, but they are not explicitly treated in the simplified Birnstiel et al. (2011) prescription.

in terms of vertically integrated optical depths,

$$\tau_\nu(r) = \int K_\nu(r,z)dz \propto \kappa_\nu(r)\,\Sigma(r), \tag{3.8}$$

$$\propto \left(\frac{r}{r_c}\right)^{\xi-\gamma} \exp\left[-\left(\frac{r}{r_c}\right)^{2-\gamma}\right], \tag{3.9}$$

where the proportionality in Eq. 3.9 explicitly shows the radial behavior of $\tau_\nu(r)$ based on Eq. 3.3 and 3.7. In this context, a model of the disk emission at any given frequency can be defined with six parameters: four that characterize the radial variation of the absorption coefficient, $\{\tau_{0,\nu},\, r_c,\, \gamma,\, \xi\}$ (where $\tau_{0,\nu}$ is the constant of proportionality in Eq. 3.9), and two that describe the source function in Eq. 3.5 and the vertical distribution of dust (through Eq. 3.1-3.2), $\{T_{10},\, q\}$. We assume a fixed mean molecular weight $\mu = 2.37$, total stellar mass $M_* = 1.35\,\mathrm{M}_\odot$ (Prato et al. 2002), disk inclination $i = 56°$ and position angle P.A. = 86° E of N (to determine sight-lines, s; Simon et al. 2000), and a distance of 145 pc.

To summarize, the parametric model described here (and motivated physically in §3.3.1) can be used to fit each of the visibility datasets described in §3.2 *independently*, and effectively provides constraints on the optical depth profile, $\tau_\nu(r)$, at each observing frequency for some assumed temperature profile. However, we do not differentiate the relative contributions of $\kappa_\nu(r)$ and $\Sigma(r)$ to that optical depth profile. Instead, we can make a connection with the radial variation of the (sub)mm–radio *colors*, $\beta(r)$ (i.e., the shape of the opacity spectrum), by recognizing that the spectral gradient of the optical depths should be unaffected by the column densities, such that

$$\beta(r) \equiv \frac{\partial \log \kappa_\nu(r)}{\partial \log \nu} = \frac{\partial \log \tau_\nu(r)}{\partial \log \nu}, \tag{3.10}$$

as long as the emission is optically thin (Isella et al. 2010, see §3.3.4 and §3.4).

3.3.3 Model fitting

We considered three different scenarios for modeling the UZ Tau E disk emission with the formalism described above. In *Scenario A*, we follow the assumptions made in previous work on the subject and fix the radial gradient of the opacities, $\xi = 0$ (Isella et al. 2010; Pérez et al. 2012). This simplified case corresponds to a radial opacity profile that does not vary spatially ($\kappa_\nu \approx$ constant). In *Scenario B*, we instead fix the radial gradient of the surface density profile, $\gamma = 1$, to facilitate a fair comparison with the assumptions made in most theoretical models of particle evolution (e.g., Birnstiel et al. 2012b). For that reason, we consider *Scenario B* to be a representative "fiducial" model. Finally, in *Scenario C* we relax these assumptions and fit both γ and ξ as independent free parameters.

For the sake of computational expediency, the modeling procedure adopted here does not incorporate a formal radiative transfer component (where the source function is determined either directly or with a stochastic simulation method): therefore, we are required to specify S_ν at each location in the model via the parameters $\{T_{10}, q\}$. Unfortunately, those parameters can be degenerate with the parameters of interest here (those that define the spatial variation of the absorption coefficient) in an unconstrained fit, so we elect instead to conduct this modeling with a fixed temperature profile (e.g., Guilloteau et al. 2011). To guide our reference assumptions for $\{T_{10}, q\}$, we constructed a simple model of the UZ Tau E spectral energy distribution using the methodology described by Andrews et al. (2009) and the Monte Carlo radiative transfer code `RADMC-3D`[3] (v0.33; C. P. Dullemond). Making some simple assumptions (κ_ν constant;

[3] `http://www.ita.uni-heidelberg.de/~dullemond/software/radmc-3d`.

$\gamma = 1$; $r_c = 40\,\mathrm{AU}$), this model predicts a midplane temperature profile with $T_{10} \approx 35\,\mathrm{K}$ and $q \approx 0.5$. Given the substantial uncertainty associated with this fiducial temperature structure, we also consider some alternative profiles with $q = 0.3$ and 0.7 to assess the effects of our assumption (see §3.4.1 for details).

For each wavelength, we determine the optimal values of $\{\tau_{0,\nu},\, r_c,\, \gamma,\, \xi\}$ and their uncertainties by comparing synthetic visibilities (computed from a ray-tracing algorithm based on Eq. 3.5) with the data. For a given set of parameters, the sky brightness distribution is constructed via ray-tracing, Fourier transformed, and then sampled to yield model visibilities at the same locations in the uv-plane that we have sampled with our observations. The fit quality metric is the χ^2 summed over the real and imaginary visibilities at all spatial frequencies, with uncertainties determined by scaling the nominal visibility weights to agree with their intrinsic scatter (cf., Isella et al. 2009).[4] We used Monte Carlo Markov Chain (MCMC) simulations that employed the Goodman & Weare (2010) ensemble sampler to construct the posterior probability distribution functions for each parameter in the multi-dimensional model space (utilizing the algorithm of Foreman-Mackey et al. 2013). Uniform priors are assumed, although with limits imposed to ensure nonsensical models are avoided: i.e., $\{\tau_{0,\nu},\, r_c\} > 0$.

[4]We have verified that in practice this re-weighting scheme does not bias any parameter estimates, and leads to only slightly inflated parameter uncertainties compared to the case where the intrinsic visibility weights computed from system temperatures, observing bandwidths, integration times, and telescope efficiencies are taken as correct.

3.3.4 Additional considerations

There are two additional complications to the modeling that require some explanation. The first is that the procedure described above is meant to be applied to the UZ Tau E disk only. However, although fainter and well-separated spatially, the continuum emission from UZ Tau W is not negligible. A simultaneous fitting of a 3-disk model to the full UZ Tau datasets is impractical, and unlikely to be helpful, because the emission from each component in the UZ Tau W binary is not well-resolved. Instead, we opted to generate simple morphological models of the UZ Tau W emission at each wavelength, and subtract them directly from the full visibility sets. We assumed that each component can be described by a flux (F_a, F_b), a size (r_a, r_b), a $1/r$ intensity profile, and a viewing geometry that is co-planar with the UZ Tau E disk. The intensity profile was selected arbitrarily; neither its selection nor that of the exact viewing geometry play any role in biasing the results of our modeling of the UZ Tau E disk. We then manually optimized the flux and size parameters by minimizing the residuals at the UZ Tau Wa and Wb locations in the image plane. After subtracting these UZ Tau W models from the visibility sets, we are left with datasets that correspond to emission from the UZ Tau E disk only. The potential impact of an imperfect UZ Tau W model subtraction on the models of the UZ Tau E disk is discussed in §3.4.3.

We also must consider the contribution from emission that is not generated by dust, especially in the Ka band, where both dust and non-dust emission mechanisms can play an important role in determining the emission budget. In Figure 3.2, it is clear that the C band (5 cm) is dominated by non-dust emission, likely free-free radiation from a stellar wind (e.g., Panagia & Felli 1975; Chiang et al. 1996), or synchrotron flares

from magnetosphere interactions induced by orbital motion in the eccentric host binary (Kóspál et al. 2011). Both of these mechanisms generate highly localized emission at the stellar position (and would *not* be resolved with our observations), with power-law spectra, $F_\nu \propto \nu^\alpha$: free-free emission has an index $-0.1 \lesssim \alpha \lesssim 0.6$, depending on the optical depth and geometry of the wind, and synchrotron flares can have $-0.7 \lesssim \alpha \lesssim 0.0$, depending on the evolution of the electron energy spectrum. Either mechanism could produce variable emission: the synchrotron flares postulated by Kóspál et al. should appear on intervals similar to the binary period, $\sim$19 d (Prato et al. 2002). However, we find no evidence for emission variability beyond the calibration uncertainties. Nor is there any support for a significant point source component in the Ka band data (see the right panels of Fig. 3.4; if a point source contribution to the Ka band fluxes were significant, it would be apparent as a significant offset of the data from zero at long projected baselines). Nevertheless, to be conservative, we include a non-disk, point source contribution to the Ka band models, with a flux density of $\sim$0.1 mJy, estimated from the C band emission assuming an optically thin free-free ($\alpha = -0.1$) spectrum (consistent with Rodmann et al. 2006). In §3.4.2, we demonstrate how that assumption affects the derived disk properties.

3.4 Results

We present the results of the parametric modeling analysis for each wavelength and model scenario in Table 3.3, which lists the best-fit values for each parameter and its associated uncertainty (in terms of a marginalized 68% confidence interval) assuming the nominal temperature profile (with $\{T_{10}, q\} = \{35\,\mathrm{K}, 0.5\}$). Synthetic observations

generated from the best-fit models are directly compared with the data in Figure 3.4: for simplicity, only the fiducial *Scenario B* modeling results are shown there, but the results for *Scenario A* and *C* are virtually identical.

Table 3.3. Estimates of Model Parameters

Model	λ (mm)	$\tau_{0,\nu}$ (at 10 AU)	r_c (AU)	γ	ξ
A	0.88	0.209 ± 0.004	137 ± 2	-0.16 ± 0.01	0 (fixed)
	1.4	0.197 ± 0.013	78 ± 2	-0.40 ± 0.05	0 (fixed)
	2.9	0.406 ± 0.119	62 ± 3	0.25 ± 0.23	0 (fixed)
	8.0	0.040 ± 0.008	39 ± 4	-0.62 ± 0.23	0 (fixed)
	9.8	0.028 ± 0.010	26 ± 4	-1.1 ± 0.6	0 (fixed)
B	0.88	0.204 ± 0.005	55 ± 2	1 (fixed)	1.70 ± 0.03
	1.4	0.237 ± 0.017	24 ± 2	1 (fixed)	2.30 ± 0.12
	2.9	0.568 ± 0.194	28 ± 12	1 (fixed)	1.14 ± 0.53
	8.0	0.091 ± 0.013	9 ± 2	1 (fixed)	2.92 ± 0.6
	9.8	0.104 ± 0.019	5 ± 2	1 (fixed)	4.3 ± 1.1
C	0.88	0.202 ± 0.001	58 ± 13	0.97 ± 0.11	1.65 ± 0.23
	1.4	0.196 ± 0.014	65 ± 11	0.13 ± 0.36	0.72 ± 0.48
	2.9	0.448 ± 0.126	89 ± 10	-0.77 ± 0.40	-1.46 ± 0.42
	8.0	0.060 ± 0.030	22 ± 16	0.53 ± 1.04	1.31 ± 1.57
	9.8	0.021 ± 0.024	25 ± 7	-1.98 ± 2.38	0.86 ± 2.42

Note. — This compilation assumes the fiducial radial temperature profile and non-disk contamination in the Ka band. See §3.4.1 and 3.4.2 regarding the effects of these assumptions on the model behaviors. The $\sim 10\%$ systematic uncertainty in the amplitude scale has not been taken into account in the errors.

An examination of the best-fit parameter values and their uncertainties may not facilitate a straightforward interpretation of the modeling results. To better summarize the outcomes of the modeling process, we present the corresponding radial optical depth profiles $\tau_\nu(r)$ derived for each frequency and model scenario in Figure 3.5 (see Eqs. 3.8 and 3.9). The uncertainties on these profiles were determined by randomly sampling the joint posteriors from the MCMC simulations described in §3.3.3 for each combination of radius and observing frequency (e.g., Isella et al. 2010). These optical depth profiles illustrate well two fundamental conclusions from the modeling. First, regardless of the model scenario adopted, the emission being considered here is optically thin at all wavelengths and radii of consequence (an a posteriori confirmation of a key simplifying aspect of the data interpretation). Second, for all model scenarios the radial distribution of optical depths (and therefore emission intensities) becomes considerably more compact as the observing wavelength increases. This latter point is a quantitative affirmation of the size–wavelength anti-correlation we postulated based on a direct examination of the visibility data in §3.2.4 (see Fig. 3.3).

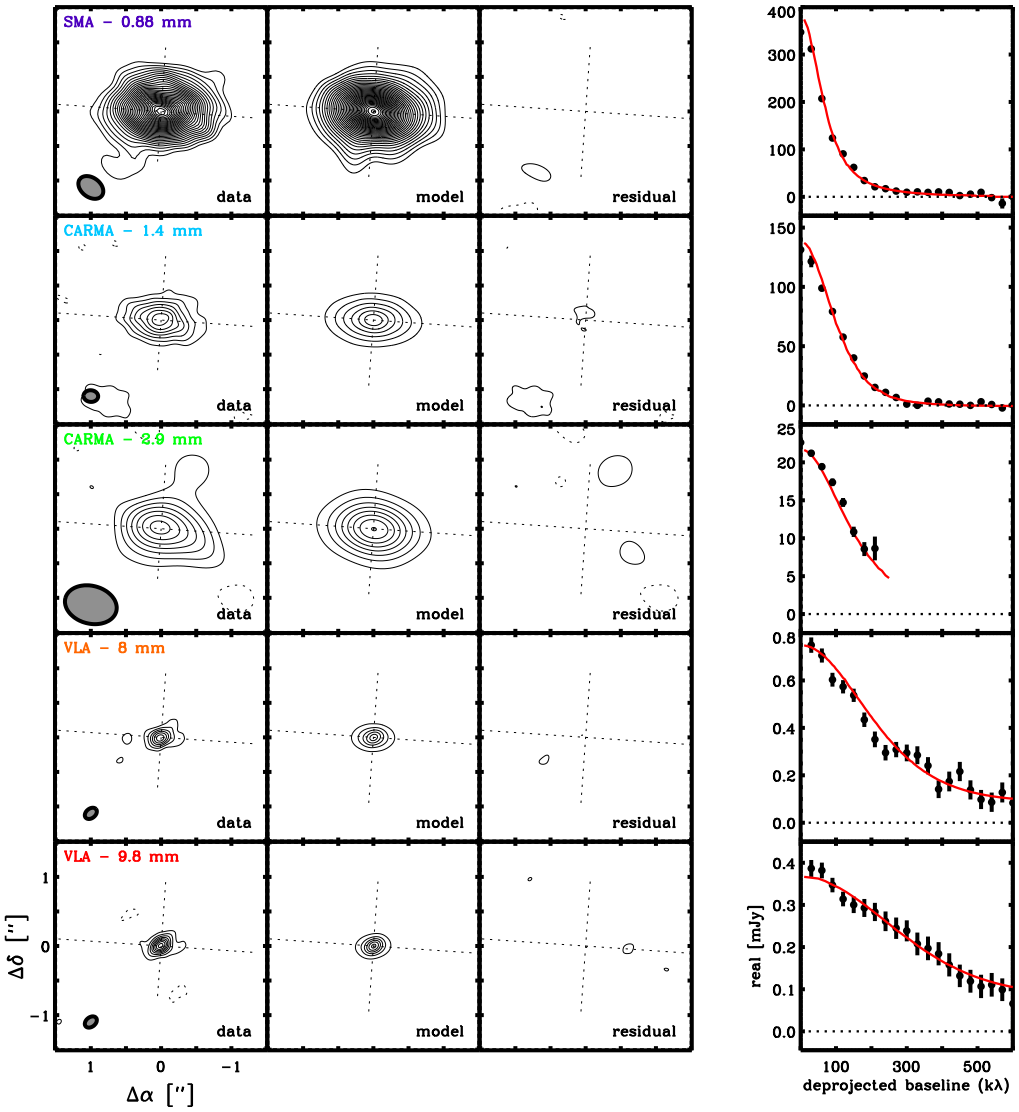

Figure 3.4: (*left*) An image-plane comparison of the data (after subtraction of a model for the UZ Tau W emission), best-fit model from *Scenario B* (synthesized in the same way as the data), and the imaged residual visibilities (as in Fig. 3.1). Dashed crosshairs mark the disk center and orientation. (*right*) The azimuthally-averaged (real) visibilities as a function of deprojected baseline for each observing frequency (as in Fig. 3.3), compared with the best-fit models for *Scenario B*. The results for *Scenario A* and *C* are indistinguishable.

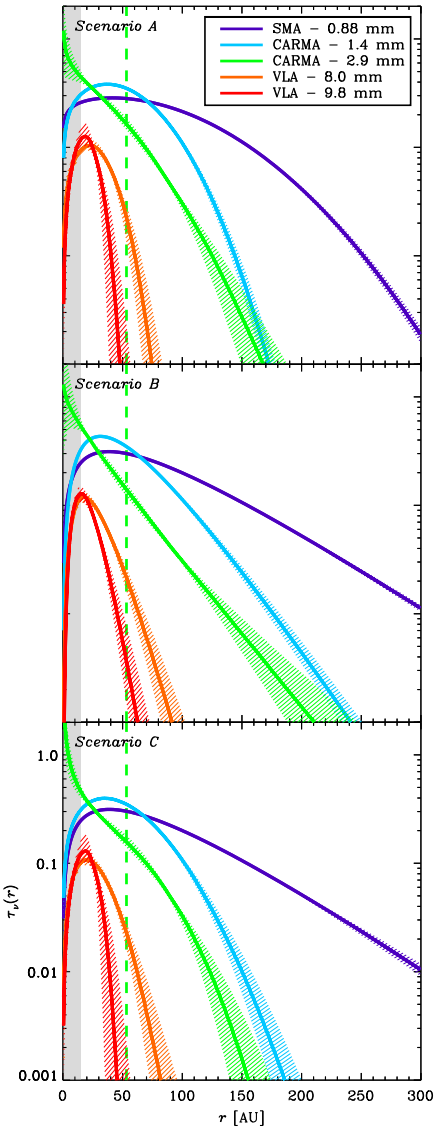

Figure 3.5: The derived optical depth profiles, $\tau_\nu(r)$, for each observing frequency and modeling scenario. The best-fit profiles are shown as thick lines; shaded regions mark the 99.7% confidence intervals. The resolution limits of our data are denoted by a gray shaded rectangle, marking the typical angular resolution limit of our data (excluding the comparatively poorer resolution 2.9 mm data), and a dashed green line, indicating the resolution of the 2.9 mm data. Information on $\tau_\lambda(r)$ inside the two regions are based on model extrapolations and are not directly constrained by the data.

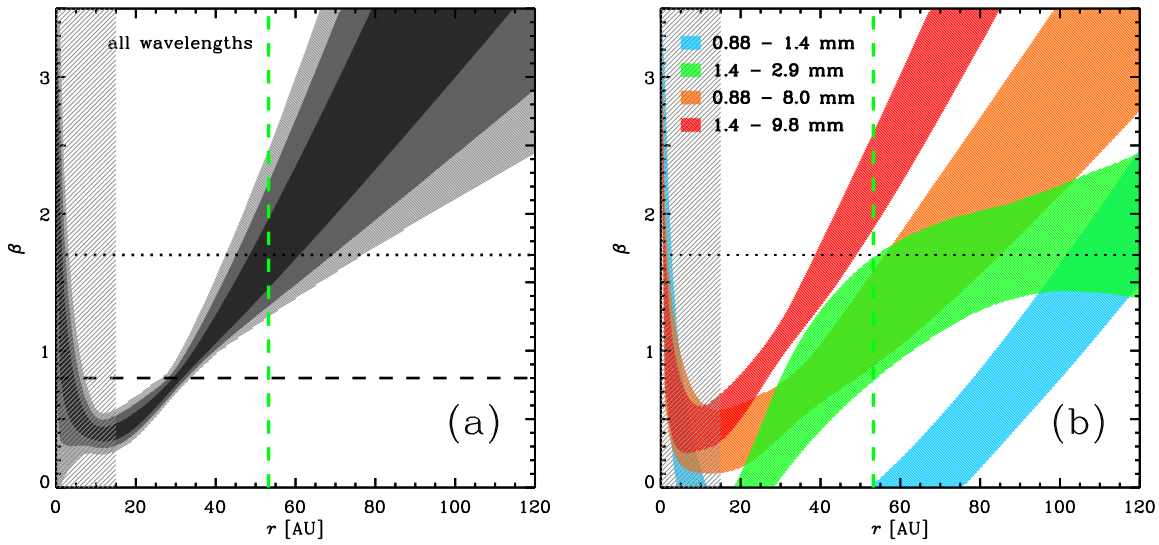

Figure 3.6: (a): The radial profile of the opacity spectral index, $\beta(r)$, constructed from the optical depth models, assuming a single power-law in frequency is applicable from 0.88-9.8 mm. From dark to light, the gray shadings represent the 68, 95, and 99.7% confidence intervals. The dotted horizontal line marks the β value derived for the interstellar medium, while the dashed horizontal line marks the β value derived by Rodmann et al. (2006) from unresolved photometry. The resolution limits are indicated with the same shaded gray region and dashed green line, as in Fig. 3.5. (b): The same as in panel (a), but constructed for different wavelength pairs (the shaded regions correspond to the 68% confidence intervals). The discrepancies in $\beta(r)$ profiles created from different combinations of wavelengths suggest the assumption of a single opacity spectral index is likely not valid. These $\beta(r)$ profiles include a 10% systematic uncertainty in the amplitude calibration at each wavelength.

We can further synthesize this information to quantify the spectral morphology of the dust opacities as a function of disk radius by constructing an index profile, $\beta(r)$,

as described by Eq. 3.10. In practice, this $\beta(r)$ profile is determined as follows: for each radius, we randomly sample the joint probability distribution functions for each model parameter, derive an optical depth at each frequency, and then fit a power-law in frequency to those τ_ν values. A probability distribution of β at each radius is determined from these power-law fits, reflecting the random sampling of the model parameter posteriors used to construct each τ_ν (i.e., the combined uncertainties in each model parameter) and an additional 10% deviation designed to account for the systematic uncertainty in the absolute amplitude calibration of the interferometer data (added in quadrature). As an example, Figure 3.6(a) shows the $\beta(r)$ profile constructed from all of the data for *Scenario B*: the profiles for *Scenario A* and *C* exhibit similar behavior (and have substantial overlap within the uncertainties). We find that in all modeling scenarios this measure of the dust opacity spectral index significantly increases with disk radius, from $\lesssim 0.5$ inside $\sim$20-30 AU to $\gtrsim 2.0$ outside $\sim$60-100 AU.

However, there is an important caveat to this result. It is clear from an examination of the derived optical depth profiles in Figure 3.5 that $\tau_\nu(r)$ is in fact *not* described well by a single power-law in frequency, especially in the inner disk. This issue is emphasized in Figure 3.6(b), where we have computed $\beta(r)$ profiles corresponding to four different frequency pairings (again for *Scenario B*). A comparison of the two panels in Figure 3.6 demonstrates that the composite measurement of $\beta(r)$ is (not surprisingly) dominated by the mm/radio colors that span the largest frequency range. In essence, the very compact morphology of the 9 mm emission forces the spectral slope computed in this way to steepen dramatically at large distances from the disk center. However, the $\beta(r)$ profiles corresponding to higher frequency emission only suggest overall flatter spectral morphologies (they tend to have substantially lower, even negative, β values), although

they all exhibit increasing trends with radius. A potential physical explanation for this behavior is addressed in §3.5. In the remainder of this section, we consider the possible roles that some of the key assumptions made in the modeling process might have on these results.

3.4.1 The dust temperature profile

Perhaps the most significant simplification adopted in our modeling effort is the assumption of a fixed radial dust temperature profile, defined as a power-law with a fiducial parametric normalization and index, $\{T_{10} = 35\,\mathrm{K},\ q = 0.5\}$ (see Eq. 3.4). Although grounded in a crude 2-D radiative transfer simulation, this $T(r)$ selection was made in an effort to keep the modeling problem tractable (e.g., Guilloteau et al. 2011), and to avoid the complication of reconciling the different temperature profiles that would be derived for each observing frequency in a more generalized analysis (e.g., Pérez et al. 2012). However, we can assess the effects of this assumption on the modeling results: the observations were also fitted with variations on the temperature profile shape for each modeling scenario, with extreme values of $q = 0.3$ and 0.7 for a fixed normalization at 10 AU (see §3.3.3).

If the continuum emission is optically thin at all relevant observing frequencies and locations, the impact of varying the temperature profile is relatively straightforward. In that case, the mm/radio emission brightness profile is roughly proportional to the product $B_\nu(T) \times \tau_\nu$, where the Planck function can be crudely approximated as linear with T (this is not strictly true, since the outer disk is cold enough that the Rayleigh-Jeans limit is not valid: however, the qualitative behavior is similar and the models properly account

for these low temperatures). Therefore, a shallow temperature profile ($q = 0.3$) requires relatively lower optical depths to reproduce the observed emission at each frequency, and vice versa for a steeper $T(r)$ ($q = 0.7$). Indeed, this is precisely what is found with our supplementary modeling: at any given radius, the optical depths at each frequency are lower (higher) for a flatter (steeper) temperature profile, relative to the fiducial $q = 0.5$ assumption. The basic shapes of the $\tau_\nu(r)$ profiles (i.e., γ, ξ, or the combination thereof) are not strongly affected by these adjustments (the mean shifts in these parameters are at most $\Delta\xi \sim \Delta\gamma \sim \Delta q \approx 0.2$), nor are the radial profiles of their spectral behavior. In both shape and amplitude, the $\beta(r)$ profiles are comparable with the fiducial case within the 68% confidence intervals. Overall, we find that the trend of increasing emission concentration with observing wavelength – or effectively an increasing $\beta(r)$ profile – is demonstrably robust to the intrinsic uncertainty in the dust temperature distribution.

In a more physically realistic model, the dust temperature structure could be considerably more complex than a simple power-law radial profile. In a more appropriate forward-modeling methodology, considerable iteration would likely be required to properly determine the co-dependence between temperature and optical depth structures in a disk with spatially varying particle properties. However, one would expect that disks with a decreasing optical depth profile that steepens with frequency at large radii would more likely than not have a relatively shallow temperature profile in the outer disk: less optical depth means that the midplane dust is heated more easily by irradiation from the central star. We suspect that a more realistic scenario might be a hybrid $T(r)$ profile that flattens (q decreases) with increasing radius in the disk.

3.4.2 Contamination from non-dust emission

In §3.3.4, we discussed our approach to account for the presence of a point-like contribution from non-dust emission in the modeling of Ka band (8.0, 9.8 mm) observations. We have assumed that this contamination is unresolved and has a flux density of ∼0.1 mJy, based on our measurement in the C band (5 cm) (i.e., assuming a nearly flat spectrum: see Table 3.2 and Fig. 3.2). This assumption should be considered a conservative upper limit on the Ka band non-dust contamination for UZ Tau E for two reasons. First, the C band map shown in Figure 3.1 indicates that the emission is marginally resolved, and therefore may have a contribution from dust. Since we would expect any $\lambda = 5$ cm dust emission to be even more compact than at Ka band, it is difficult to disentangle the relative fractions of disk and non-disk contributions in the C band. And second, the spectral behavior of the VLA radio emission is not strongly constrained by the data (due to limited measurements between the Ka and C bands), but some of the potential non-dust radiation mechanisms (e.g., synchrotron radiation from flares or stellar coronae) can produce negative spectral indices that would lead to much smaller contributions in the Ka band than have been assumed. Therefore, to assess the impact of our assumed contamination on the results described above, we repeated the modeling procedure with the alternative assumption that *all* of the Ka band emission is from dust.

Figure 3.7 compares the Ka band (8.0 and 9.8 mm) optical depth ($\tau_\nu(r)$; as in Fig. 3.5) profiles as well as the opacity index profile ($\beta(r)$; as in Fig. 3.6) for model fits both with and without the conservative assumption for radio contamination. Qualitatively, the outcomes under both assumptions are consistent: the optical depth

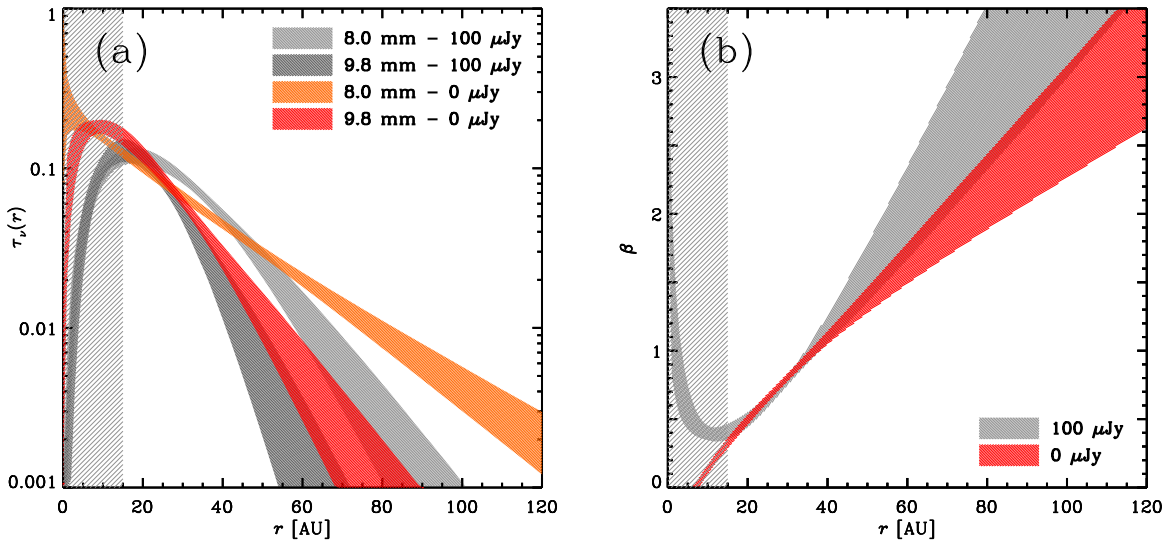

Figure 3.7: (a): Comparison of the 8.0 (light shaded) and 9.8 mm (dark shaded) optical depth profiles for models that include the fiducial, conservative assumption of point-like radio contamination (*gray*; as in Fig. 3.5) and those that do not (*red*). The inclusion of contamination produces a more compact $\tau_\nu(r)$ profile with a lower central optical depth. (b): The same comparison, but for the opacity spectral index profiles, $\beta(r)$ (as in Fig. 3.6a). The uncontaminated models result in a flatter opacity index profile at large r, although the increasing trend in $\beta(r)$ is still clearly present.

profiles are still compact relative to the shorter wavelengths, and therefore the $\beta(r)$ profile demonstrably increases with radius in the disk. However, it should be clear that from a quantitative perspective the treatment of non-dust contamination in the Ka band has a considerable impact on the results. This is not particularly surprising: although the conservative assumption for contamination represents only 10-20% of the total flux density in the Ka band, it comprises ∼50% of the peak intensity at the disk center. The removal of that contamination generates two principal differences in the results. First,

the optical depths in the disk center must increase to compensate (see Fig. 3.7a). The second difference is more subtle, and can perhaps be best understood by referring to the visibilities in Figure 3.3. Models that do not include a point source contribution yield steeper declines in the visibility amplitudes with projected baseline than would otherwise occur, thus inducing a more resolved disk morphology. In essence, the uncontaminated scenario will necessarily produce more spatially extended optical depth profiles in the Ka band, and therefore a relatively flatter $\beta(r)$ (as in Fig. 3.7b: analogous effects are found for opacity index profiles constructed from different wavelength pairs). A definitive conclusion regarding the appropriate assumption for radio contamination would require future high resolution measurements at frequencies intermediate to Ka and C bands (K/Ku/X bands with the VLA).

3.4.3 Potential bias from the UZ Tau W disks

Another consideration for simplicity made in §3.3.4 was to subtract off models of the emission from the UZ Tau W components before interpreting the UZ Tau E emission. There, we noted the potential concern that the use of an improper model for UZ Tau W could, in principle, bias our results. To test that possibility, we have repeated our fiducial analysis of the UZ Tau E disk emission using different variations on the nominal modeling prescription for the disks in the UZ Tau W binary. We considered simple radial intensity profiles for the UZ Tau W emission – power-law intensity profiles with sharp outer cut-offs, and profiles that mimic the tapered edge of the similarity solution prescription in Eq. 3.3 – and a range of disk inclinations and major axis orientations. The simple parameters in these intensity models (a normalization, size, and gradient)

were crudely optimized by minimizing the residuals in the synthesized images near UZ Tau W, and then the modeling analysis outlined in §3.3 was performed for the UZ Tau E disk. Regardless of the details for the UZ Tau W models, we found no shifts in the UZ Tau E model parameters. As long as the UZ Tau W models do not leave *large* residuals ($\gg 5\,\sigma$), the UZ Tau E modeling results are robust to any uncertainty in the details of the UZ Tau W characterization and subtraction process.

3.5 Discussion

We have presented sensitive, high angular resolution continuum observations of the disks in the UZ Tau quadruple star system at six different wavelengths that span the (sub)millimeter/radio spectrum: 0.88, 1.4, 2.9, 8.0, 9.8, and 50 mm. Emission at all wavelengths was firmly detected from three distinct components, associated with the UZ Tau E close binary and each star in the UZ Tau W pair. At wavelengths shortward of 1 cm, the spatially-integrated spectrum for each component is consistent with thermal greybody emission from a dusty disk: the 5 cm emission has a substantial contribution from a different mechanism. The dust emission from the UZ Tau E circumbinary disk is well resolved, but we find a clear, empirical trend that the size of the emission distribution is anti-correlated with the observing wavelength. A quantitative confirmation of this trend was derived using a series of models that aimed to measure the radial optical depth profiles at each wavelength, and thereby the spatial variation of the dust colors across the millimeter-wave spectrum. We find robust evidence that the dust emission becomes progressively redder at small disk radii: i.e., that the power-law index of the dust opacity spectrum, β, increases with radius in the UZ Tau E disk. However, there are also clear

indications that the dust opacities in this part of the spectrum are not described well by the single power-law in frequency that is typically assumed.

Previous radio-wave measurements of the UZ Tau system made by Rodmann et al. (2006) suggested a disk-integrated spectrum with a power-law index 2.7 ± 0.1 from 1-7 mm, in rough agreement with what we find here. They argued for a globally-averaged $\beta = 0.8 \pm 0.1$ (see also Ricci et al. 2010b); we find agreement with this value of β from the (sub)millimeter to the 8.0 mm band, with the 9.8 mm data slightly discrepant. This result is essentially the same value from all of our modeling scenarios. Guilloteau et al. (2011) employed a different, forward-modeling approach with two alternative (assumed) parametric forms for $\beta(r)$ to analyze observations of the UZ Tau E disk at 1.3 and 2.7 mm with comparable sensitivity and resolution to those presented here. Their best-fit $\beta(r)$ distributions are comparable (within the admittedly large uncertainties) to the opacity index profile that we derive for this pair of wavelengths (compare their Fig. 11 with the green profile in our Fig. 3.6b). The good agreement between our results is a strong affirmation that an increasing $\beta(r)$ profile is *required* to explain the observations, regardless of the specific approach chosen to interpret the data. Our modeling methodology is most similar to the recent analysis of the AS 209 disk by Pérez et al. (2012). A direct comparison of the AS 209 and UZ Tau E disk $\beta(r)$ profiles shows that they have a remarkably similar morphology, although the UZ Tau E profile increases slightly more steeply at large radii due to the much more compact morphology of its emission in the Ka band (8.0 and 9.8 mm).

The results derived here attest to the mounting evidence that substantial spatial variations in the spectral behavior of the dust opacities are a *generic feature* of protoplanetary disks. The most obvious interpretation of those results is that the

distribution of particle sizes depends intimately on disk location, such that larger particles are preferentially concentrated near the stellar host. However, the optimal approach for converting the observations into physically meaningful constraints on particle size distributions remains unclear. The methodology we used in §3.3 and 3.4 serves as an elaborate, physically motivated means of quantifying the spectral morphology of the dust emission as a function of radius. But these measurements need to be interpreted with caution, since we cannot easily convert β values to physical parameters related to the particle size distribution.

Nevertheless, there are promising avenues that merit pursuit. One of the most interesting results to come from our analysis is the realization that the morphology of the $\beta(r)$ profile has a strong dependence on the wavelength range being considered: the spectrum tends to be flatter (lower β) at shorter wavelengths. There is a straightforward, physical explanation of this phenomenon in terms of the dust opacities (cf., Pérez et al. 2012). If most of the emission is originating from particles with sizes (a) that are comparable to, or larger than, the emitting wavelength, the opacity spectrum (κ_ν) in that wavelength range will be roughly flat (i.e., the geometric optics limit). Indeed, for extreme top-heavy distributions where $\lambda \sim a$, there is a resonant regime where κ_ν can even *increase* over a limited wavelength interval. Therefore, we find a natural interpretation for our results if the mm/radio continuum emission – particularly in the inner disk – is being generated by an abundance of large particles, with sizes nominally in the mm/cm range.

To ground this possible explanation in a more quantitative analysis, we follow the approach of Pérez et al. (2012) to re-interpret our modeling results in a slightly different context. As before, at each model radius we Monte Carlo sample the joint probability

distribution in the $\{\tau_{0,\nu},\ r_c,\ \gamma,\ \xi\}$ parameter-space to effectively derive a sequence of optical depths at each frequency. But here, we decompose those results, $\tau_\nu = \kappa_\nu \Sigma$, and identify the combination of opacity spectrum morphology and surface density (of the solids) that best describe the given model parameter combination. To achieve that, the opacity spectrum is parameterized in terms of the particle size distribution, assuming it behaves as a power-law with index p from $0.01\,\mu$m up to an arbitrary $a_{\rm max}$. For a given composition, the specification of $\{a_{\rm max},\ p\}$ (and the local temperature, fixed in the modeling) sets the spectral behavior of the model at each radius, while the choice of Σ determines the normalization. Since this is a highly degenerate problem and we are mostly interested in a conceptual illustration of the results, the particle composition and size distribution index p are fixed in our analysis. We assume the grains are compact composite spheres made of 62% water ice, 30% carbonaceous material, and 8% olivine (percentages by volume; for purposes of comparison, this is the same composition assumed by Pérez et al. 2012). The optical constants for individual materials (from Warren 1984; Zubko et al. 1996; Semenov et al. 2003, respectively) were combined with the Bruggeman mixing rule, and then opacity spectra for any combination of $\{a_{\rm max},\ p\}$ were calculated with a Mie code. This analysis was performed for each modeling scenario using two representative values of the size distribution index, $p = 3.5$ and 3.0 (see Draine 2006). Due to the relatively low signal-to-noise of the Ka band optical depth profiles, we have combined the 8.0 and 9.8 mm data by using the geometric average and employed this average in our fits.

Figure 3.8 shows the results of this re-interpretation of the models, with the derived radial profiles of Σ (*top*) and $a_{\rm max}$ (*bottom*) for $p = 3.5$ (*left*) and 3.0 (*right*) in *Scenario B*. Both cases suggest that $a_{\rm max}$ increases with proximity to the central binary, and varies

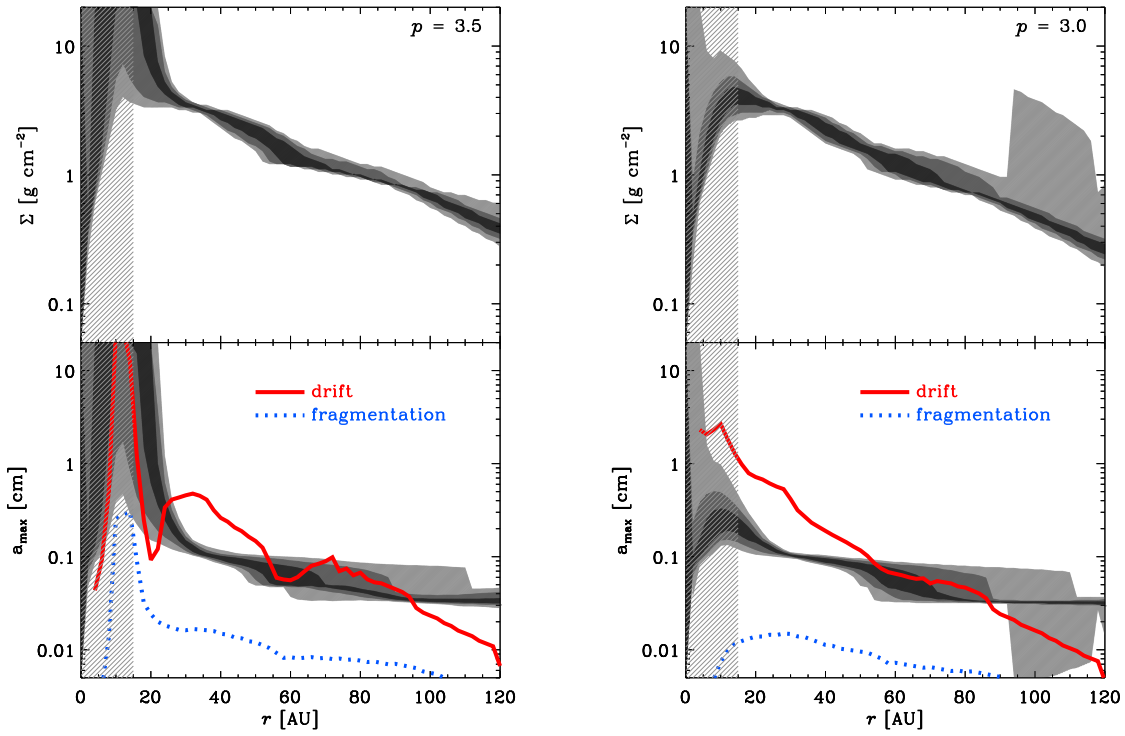

Figure 3.8: The inferred radial distributions of the dust surface densities (*top*) and maximum particle sizes (*bottom*) for model *Scenario B* and particle size distributions with power-law indices $p = 3.5$ (*left*) and 3.0 (*right*). The shading and hatched regions are as in Fig. 3.6(a). The red and blue curves represent simple predictions for the particle evolution dominated by radial drift and turbulent fragmentation, respectively, for fiducial disk parameters (see text; Birnstiel et al. 2012b).

by a factor of $\gtrsim$10 across the extent of the disk, from $\sim$300 μm to at least 3 mm (and potentially much larger for $p = 3.5$). To provide some context for these $a_{\rm max}$ profiles, we also display comparisons to simple, analytic prescriptions for the limiting particle sizes in the cases where radial drift (*red*) and turbulent fragmentation (*blue*) are the dominant drivers of the size distribution (Birnstiel et al. 2012b), assuming a constant gas-to-dust ratio of 100, a turbulent viscosity parameter $\alpha = 0.01$, and a fragmentation velocity of

$u_f = 10\,\mathrm{m\ s^{-1}}$, as might be expected for icy particles (e.g., Wurm & Blum 1998). Inside a radius of ∼80 AU, this interpretation of the data suggests that radial drift – the inward migration of solids due to the drag forces they feel from the sub-Keplerian rotation of the gas disk (Weidenschilling 1977) – appears to play the dominant role in setting the particle size distribution in the UZ Tau E disk. It is unclear how the results outside 80 AU should be interpreted: at these large radii, there is effectively no emission from the Ka band, so the models are largely driven by an attempt to fit the detailed behavior at the shortest wavelengths (880 μm and 1.4 mm) only. Nevertheless, it is telling that this drift-dominated behavior was also found for the AS 209 disk (Pérez et al. 2012). It should be noted, however, that consistency of the observed a_{max} with that predicted in a fragmentation-dominated regime could be produced if α were lower (~ 0.001) or u_f higher ($\sim 30\,\mathrm{m\ s^{-1}}$).

Ultimately, multi-wavelength, spatially resolved millimeter/radio datasets like those presented here for the UZ Tau E disk hold tremendous promise for a new capability to derive empirical constraints on the growth and migration of disk solids. Although there is unequivocal evidence for a spatial variation in the millimeter/radio spectral morphology in this (and other) disks, there is still much to be learned and developed in terms of the interpretation of the data. We expect that the modeling of such data will mature in the near-term, as numerical simulations of particle evolution strive to provide more accessible, analytic guidance for a flexible, parametric, forward-modeling approach to the problem. With the start of full operations at the Atacama Large Millimeter Array project and the upgraded VLA facility, the prospects are especially good for substantial observational input into these models using the multiwavelength approach illustrated here.

3.6 Summary

We have presented sensitive interferometric observations at wavelengths of 0.88, 1.4, 2.9, 8.0, and 9.8 mm (and supplementary data at 5 cm) that resolve the continuum emission from three dust disks in the UZ Tau quadruple star system, as part of the "Disks@EVLA" key project. Using a simple modeling prescription, we used these data to help constrain the evolutionary state of solid particles in these disks. The key conclusions from this work are as follows:

- All three components in the UZ Tau system have spatially-integrated thermal greybody spectra out to a wavelength of $\sim$1 cm, with shallow slopes that are consistent with substantial particle growth compared to normal interstellar medium values. At a wavelength of 5 cm, there is a substantial contribution from non-dust emission toward all components.
- The emission from the UZ Tau E disk is resolved at all wavelengths. We find a clear, empirical relationship between the spatial extent of the emission and the observing wavelength: the emission becomes progressively more compact at longer wavelengths.
- This anti-correlation between the emission size and wavelength is quantified using simple parametric modeling prescriptions designed to measure the radial optical depth profiles at each wavelength, and therefore the spatial variation of the disk *colors* across the millimeter/radio spectrum. We find robust evidence that the dust in the UZ Tau E disk substantially reddens with proximity to the central binary: or, put another way, that the power-law index of the opacity spectrum, β, increases with disk radius. However, there are also clear indications that particle opacities

have a more complex spectral behavior than is typically assumed.

- A comparison with simple models of the opacity spectra suggests that the maximum particle sizes are enhanced by a factor of $\sim$10 or more in the inner regions of the UZ Tau E disk, and that radial drift is likely the dominant mechanism in setting the particle size distribution.

Chapter 4

Particle Growth in the Disks of the Multiple Systems UX Tauri and AS 205

This thesis chapter will be submitted to the Astrophysical Journal.

Abstract

We present sensitive, high angular resolution ($\sim$0.1-0.5″) observations of the radio continuum emission from the AS 205 triple and UX Tau quadruple systems at wavelengths of 0.88, 1.4, 8.0, 9.8, and 50 mm and 0.88, 7.3, and 50 mm, respectively. Emission is detected at all wavelengths towards each system. Thermal greybody dust continuum emission from both the AS 205 A circumstellar disk and AS 205 Bab circumbinary disk

dominates the emission out to a wavelength of ∼1 cm. The same is true for the UX Tau A disk: no emission is resolved toward the other components of the UX Tau system. The emission at 5 cm, assumed to be of stellar origin, is used to place constraints on the contribution of non-dust emission at the shorter wavelengths. The spatial extent of the emission from the AS 205 A disk depends on the observing wavelength, with longer wavelength emission becoming more compact. The UX Tau A disk shows no significant wavelength dependence of the emission size. Parametric models are used to derive radial profiles of optical depth at each wavelength. By fitting the profiles for the AS 205 A dust disk to computed dust opacities for typical grain compositions assumed in circumstellar disks, we show that the maximum grain size varies by as much as a factor of ~ 10, from $\gtrsim$ cm sizes in the inner disk to $\lesssim$300 μm in the outer disk. These results are interpreted in the context of recent theoretical work coupling the evolution of the dust and gas components of the disk. For typical assumed disk parameters, neither radial drift nor turbulent fragmentation of dust particles can totally explain the distribution of dust sizes in this disk; some combination of these effects must be invoked.

4.1 Introduction

The current paradigm of planet formation, core accretion, requires the rapid growth of solid particles from $\lesssim$ microns to millimeter/centimeter sizes in the gas-rich disks around young stars within a typical timeframe of $\sim 10^6$ yr. The evolution of the dust population is intricately linked to that of the gas, and the interaction between the two can both inhibit and accelerate grain growth. Obstacles that are introduced by the gas-dust interaction include radial drift of particles toward the star (Weidenschilling 1977),

turbulence-induced fragmentation of large particles (Blum & Wurm 2008; Dominik & Tielens 1997), bouncing (Zsom et al. 2010), and electrostatic repulsion of dust particles (Okuzumi 2009). While the effects of the gas-dust coupling have been assumed to pose a substantial challenge to growth of dust particles beyond cm-m sizes, both hydrodynamic (e.g., zonal and meridonal flows; Urpin 1984; Kley & Lin 1992; Johansen et al. 2006) and particle trapping (e.g., radial and azimuthal pressure bumps; Whipple 1972; Brauer et al. 2008b; Pinilla et al. 2012b,a; Birnstiel et al. 2013) mechanisms can either reduce the efficiency of some of these processes (particularly radial drift) or create large particles so quickly that the largest disk solids become effectively decoupled from the gas. The relative contributions of these processes are, at this point, uncertain. Despite the complications these effects present, modelers have made some progress in understanding how the growth of smaller particles to cm-sizes can happen in protoplanetary disks (Birnstiel et al. 2010a, 2011, 2012b). These models, however, rely on some assumptions about the dust and gas properties that, at the present time, can only be considered educated guesses. Further progress in understanding how the dust evolves in the gaseous environment of the disk can only be made through observational work, particularly the millimeter and centimeter observations that directly probe the large grain population.

Submillimeter and radio-wave continuum observations inform us that solids have grown to $\gtrsim$ mm-sizes within $\sim$ 1 Myr. At the long-wavelengths probed by these observations, the emission is primarily optically thin, and the spectral shape is dictated by the dust temperatures and opacities, κ_ν. The surface brightness can be described as

$$I_\nu(r) = B_\nu(T(r)) \left(1 - e^{-\tau_\nu(r)}\right) \approx B_\nu(T(r))\tau_\nu(r) = B_\nu(T(r))\Sigma(r)\kappa_\nu(r) \qquad (4.1)$$

where $B_\nu(T)$ is the Planck function, T is the dust temperature, Σ is the dust surface

density, and κ_ν is the dust opacity. While the dust opacity depends on both composition and temperature, the overall shape of the spectrum is set by the grain size distribution. For most reasonable assumptions about the dust properties, the opacity in the millimeter and radio regimes is a power-law, $\kappa_\nu \propto \nu^\beta$, with β most dependent on the size distribution of dust particles, $n(a)$ (e.g., Miyake & Nakagawa 1993; Stognienko et al. 1995; Henning & Stognienko 1996; D'Alessio et al. 2001; Draine 2006). For ISM-like (i.e., unevolved) grains, β has been measured at $\sim 1.7 - 2.0$ (Hildebrand 1983; Henning et al. 1995; Goldsmith et al. 1997; Finkbeiner et al. 1999; Li & Draine 2001). However, long-wavelength photometry of protoplanetary disks has determined β values from 0 to 1, significantly lower than for the ISM (Beckwith & Sargent 1991; Natta & Testi 2004; Andrews & Williams 2005; Wilner et al. 2005; Rodmann et al. 2006; Ricci et al. 2010a,b, 2011a).

A thorough understanding of the processes that drive the evolution of the dust size distributions in disks will continue to elude us until we can calibrate theoretical models against observations. These models generally predict that the size distribution of dust particles varies as a function of radius, with larger particles preferentially inhabiting the inner disk. So far, the principal results on grain growth have relied on unresolved photometry. But testing and calibrating these models requires high spatial resolution, so interferometric observations are required. Thus far, there have been two good examples of disks sufficiently well resolved at multiple wavelengths to say definitively that radial evolution of the dust grain size distribution occurs. These disks, the UZ Tau E circumbinary disk (Chapter 3) and the disk around the isolated star AS 209 (Pérez et al. 2012) were observed at a spread of wavelengths between 0.88 mm and 1 cm as

part of the "Disks@EVLA" project (Chandler et al., *in preparation*).[1] Both disks show significant reddening in the continuum spectrum with proximity to their central hosts, which has been interpreted as a flattening of the opacity spectrum from the outer disk, where $\beta \sim \beta_{\rm ISM}$ to the disk center, where $\beta \sim 0.0 - 0.5$. Modeling indicates that the maximum dust grain sizes vary by a factor of $\gtrsim 10$ across these disks, consistent with growth that is limited by the radial drift of large particles toward the star. In order to usefully constrain the models of dust evolution, more examples are required.

This chapter continues the pursuit of that goal. We study new multiwavelength submillimeter and radio imaging observations of circumstellar disks in two multiple systems: UX Tau in the Taurus-Auriga star forming region, and AS 205 in Ophiuchus. The AS 205 A disk and the UX Tau A disk are sufficiently well resolved at multiple bands to make statements about the radial evolution of their constituent grain sizes.

AS 205 was discovered to be a multiple by Cohen & Kuhi (1979), who first reported an optical counterpart at a separation of $\sim 1''$. The separation of the companion AS 205 B from the K5 primary was subsequently refined by Ghez et al. (1993) to be $1\farcs34$, approximately 194 AU at the distance of Ophiuchus ($d \approx 125$ pc; de Geus et al. 1989). Koresko (2002) then discovered AS 205 B to be comprised of a pair of almost equally bright stars (K7/M0; Eisner et al. 2005) with an angular separation of ≈ 8.5 mas, approximately 1 AU physical separation, making AS 205 a hierarchical triple. Previous submillimeter observations by Andrews & Williams (2007a) found that this system exhibited a substantial millimeter excess, which was resolved by Andrews et al. (2009) into two components, a bright circumstellar disk around AS 205 A, and a substantially

[1] `https://safe.nrao.edu/evla/disks/`

fainter circumbinary disk around AS 205 B.

UX Tau was originally discovered to be a multiple system by Joy & van Biesbroeck (1944), who found a companion UX Tau B at 5.″7 almost directly due west of the primary. A tertiary companion, UX Tau C, was reported in the optical at $\sim 2.''0$ due south by Jones & Herbig (1979). Correia et al. (2006) then found UX Tau B to be comprised of a 0.″13 stellar pairing, and they also refined the position of UX Tau Bab relative to UX Tau A at 5.″856 ($\approx$ 849 AU at the distance $d \approx 145$ pc of Taurus-Auriga; Torres et al. 2007) as well as that of UX Tau C relative to that of UX Tau A at 2.″69 ($\approx$ 390 AU). The system is notable for a couple of reasons. First, despite the widely separated components, only the primary has any evidence of disk material in either the infrared or submillimeter bands. The UX Tau A disk was first observed in the millimeter at 250 GHz by Altenhoff et al. (1994), who found a millimeter excess over the stellar photosphere and interpreted it as evidence of a cool mass reservoir. Second, the disk around UX Tau A is substantially depleted of dust grains near the stellar host. (Espaillat et al. 2007) By modeling *Spitzer* IRS spectra, Espaillat et al. were able to estimate the region of low IR optical depth to a radius of approximately 28 AU. Subsequent imaging of the millimeter continuum emission by Andrews et al. (2011) found that the cavity inferred in the infrared persisted in millimeter bands, indicating a region fairly depleted of dust grains of all sizes. Despite that inner disk depletion, a substantial, yet compact, belt of millimeter emission amounting to $F_{0.88\ \mathrm{mm}} \approx 150$ mJy exists outside the cavity and extends from a radius of $\sim$ 25 to 50 AU.

Here, we present observations of the AS 205 and UX Tau multiple systems at wavelengths of 0.88, 1.4, 8.0, 9.8, and 50 mm, and 0.88, 7.3, and 50 mm, respectively. Using data from the Submillimeter Array (SMA), the Atacama Large

Millimeter/submillimeter Array (ALMA), and the Karl G. Jansky Very Large Array (VLA), we measure the spatial variation of mm/radio colors in the dust disks around AS 205 A and UX Tau A, and provide constraints on their mm/radio spectra. In §4.2, we describe the observations and data calibration. In §4.3, we outline the adopted modeling techniques. The modeling results are presented in §4.4, and then discussed in the context of particle evolution models in §4.5. A summary of our principal conclusions is provided in §4.6.

4.2 Data Reduction and Imaging

4.2.1 SMA observations at 0.88 mm (340 GHz)

UX Tau was observed with the SMA interferometer (Ho et al. 2004) on Mauna Kea, Hawaii at 0.88 mm in three different array configurations: compact (C; 6-70 m baselines) on 2009 Oct 23, extended (E; 16-70 m baselines) on 2010 Jan 9, and very extended (V; 68-509 m baselines) on 2010 Feb 5. The observations were conducted in good weather conditions, with stable phases and low precipitable water vaper (PWV) levels (<2 mm). The correlator was configured to process two 2 GHz-bandwidth intermediate frequency (IF) bands for each of two receiver sidebands (a total bandwidth of 8 GHz), centered at ±5 GHz and ±7 GHz from the local oscillator (LO) frequency, 340.755 GHz. Each IF+sideband combination comprised 24 slightly overlapping spectral chunks of 104 MHz width, divided into 32 channels each: a single chunk reserved for the CO J=3−2 transition was divided into 256 channels. The observations cycled between UX Tau and the quasars 3C 111 and J0510+180 in a 10-20 minute cycle, depending on the array

configuration. These SMA observations were originally presented by Andrews et al. (2011).

AS 205 was observed with the SMA in the compact configuration on 2006 May 12, in the extended configuration on 2006 June 3 and in the very extended configuration on both 2007 May 26 and 2007 June 17. The correlator settings were the same as those used for the UX Tau observations. Observations of AS 205 were interleaved with those of the complex gain calibrator J1625-254 on a 15-20 minute cycle (for the compact / extended configuration) or a $\sim$ 10 minute cycle (for the very extended configuration). The quasars 3C 454.3 and 3C 279 were used for bandpass calibration, while observations of Solar System objects, typically Uranus, Saturn, Titan, or Callisto, were used as absolute flux calibrators. These SMA observations were originally presented by Andrews et al. (2009).

The visibility data from each observation were calibrated independently with the `MIR` package. The spectral bandpass response was determined from observations of the quasars 3C 279 and 3C 454.3. The absolute amplitude scale was bootstrapped from observations of Solar System objects, with an estimated systematic uncertainty of $\sim$10%. A complex gain calibration was determined from observations of nearby quasars, 3C 111 and J0510+180 (for UX Tau) and J1625-254 (for AS 205). The calibrated data were spectrally averaged to form multiple wideband continuum channels, which were subsequently combined.

The composite sets of visibilities for each source were then Fourier inverted with Briggs weighting (for UX Tau, the robust parameter was set to 0.7, while for AS 205, it was set to -1), deconvolved with the `CLEAN` algorithm, and restored with the synthesized beam using the `MIRIAD` package. For UX Tau, the synthesized beam was $0\farcs34 \times 0\farcs29$

(P.A = 47°), while for AS 205 the synthesized beam was $0\farcs46 \times 0\farcs35$ (P.A = 193°),

4.2.2 ALMA observations at 1.4 mm (218 GHz)

The AS 205 system was observed with the Atacama Large Millimeter/submillimeter Array (ALMA) at 1.4 mm as part of an unrelated project; these data were acquired from the ALMA archive[2] for use in this work. A first observation was conducted on 2012 Mar 27 in the Early Science Compact array configuration (18 - 125 m baselines), and a second was made on 2012 May 04 in the Early Science Extended array configuration (36 - 400 m). The correlator was set to an LO frequency of 226.040 GHz. Because the science goals of the observations required high spectral resolution of various CO transitions and not continuum sensitivity, the correlator was configured to process four spectral windows (SpWs), each of 117.187 MHz bandwidth divided into 3840 channels. These spectral windows were centered at 230.530, 232.411, 220.524, and 219.669 GHz to provide spectral coverage for the ^{12}CO($J = 2-1$), ^{13}CO($J = 2-1$), and ^{18}CO($J = 2-1$) transitions at 230.538, 220.399, and 219.560 GHz, respectively. Observations of AS 205 were interwoven with those of the quasar J1625-254 on a $\sim$ 3 minute cycle.

The visibility data from each observation were calibrated independently with the `CASA` package. The bandpass calibration was determined from observations of the quasar J1924-292. The absolute amplitude scale was derived by observations of Titan, with an uncertainty of $\sim$ 10%. Observations of the quasar J1625-254 were used to solve for the antenna complex gain. After calibration, the data (i.e., all data except within a narrow region around the centers of the CO transitions) were spectrally averaged to

[2] `https://almascience.nrao.edu/alma-data/archive`

three pseudo-continuum channels (the ^{12}CO line was sufficiently broad that extracting a good continuum from this spectral window proved fruitless).

The composite sets of continuum visibilities for AS 205 were Fourier inverted using Briggs weighting with a robust parameter of 0, in order to create a beam of size comparable to those of the other continuum data sets. The inverted dataset was then deconvolved with the `CLEAN` algorithm and restored with the synthesized beam, also in the `CASA` package. The resulting synthesized beam was $0\farcs59 \times 0\farcs50$ (P.A. = 98.1°).

4.2.3 VLA observations at 7.3, 8.0, 9.8, and 50 mm (41.0, 37.5, 30.5, and 6.0 GHz)

The disks in the UX Tau and AS 205 systems were observed with the VLA as part of the "Disks@EVLA" program. UX Tau was observed in the Q band in the D (35-1000 m baselines), C (45-3400 m), and B (0.24-11 km) configurations on 2010 Aug 12, 2010 Nov 23, and 2012 Aug 10, respectively. The correlator was configured with two 1 GHz-wide IF bands centered at 40.5 and 41.5 GHz (corresponding to a central wavelength of 7.3 mm), with each IF band divided into eight 128 MHz sub-bands composed of 64 channels apiece. The observations were conducted in good conditions with low atmospheric optical depth ($\tau \approx 0.06$ at 41 GHz) and good phase stability. Additional observations in the C band were conducted with the D and A (0.68-36 km baselines) array configurations on 2010 July 11 and 2011 July 23, respectively. The two available 1 GHz-wide IF bands were set to continuously span sky frequencies from 5 to 7 GHz in the D configuration observations, but were centered slightly apart at 4.5 and 7.5 GHz when we observed in the A configuration. For both Q and C band, the observations of UX Tau were interleaved

with the nearby quasar J0431+1731 on a ∼3 and 10 minute cycle, respectively, to allow for complex gain calibration of the data.

AS 205 was observed in the Ka band in the CnB (65-7700 m baselines), the BnA (0.2-20 km), and the A configurations on 2011 Jan 26, 2011 May 16, and 2011 Jun 16, respectively. The correlator was configured with two 1 GHz-wide IF bands centered at 30.5 and 37.5 GHz (corresponding to central wavelengths of 8.0 and 9.8 mm), with each IF band divided into eight 128 MHz sub-bands composed of 64 channels apiece. The observations were conducted in good conditions with low atmospheric optical depth ($\tau \approx 0.04$ at 34 GHz) and good phase stability. Additional observations in the C band were conducted with the D and A array configurations on 2010 Sep 27 and 2011 Jul 14, respectively. The placements of the IFs for each configuration were identical to those used for the UX Tau observations. For both Ka and C band, the observations of AS 205 were interleaved with the nearby quasar J1617-1941 on a ∼3 and 10 minute cycle, respectively, for complex gain calibration.

The visibilities for each dataset were iteratively calibrated and flagged for interference and bad pointing, and subsequently imaged using the `CASA` package. After removing radio frequency interference and other corrupted data, observations of 3C 84 were used to calibrate the bandpass response. The spectrum of 3C 84 is not flat, but rather varies across the widely separated individual sub-bands. To account for the shape of the 3C 84 spectrum, we bootstrapped its flux density in each sub-band from observations of the amplitude calibrator 3C 286, fit a power-law model to its spectrum, and then used that model to compute the bandpass response and calibrate the observations of the other sources. After bandpass calibration, the Q and Ka band data were spectrally averaged, giving eight 128 MHz-wide pseudo-continuum channels for each IF band. To minimize

bandwidth smearing, the C band visibilities were not spectrally averaged. Observations of J0431+1731 were used to calibrate the complex gain variations for UX Tau, while J1617-1941 was used to calibrate those variations for AS 205. The amplitude scale was determined from observations of the well-monitored quasar 3C 286 for each dataset. Because 3C 286 is resolved in all but the most compact VLA configuration, a catalogued source model was used for this calibration, with the flux density scaled as appropriate to each sub-band. The estimated uncertainty in the amplitude scale is $\sim$10% at Ka band and $\sim$5% at C band.

Although the calibrations performed for both the high-frequency (Ka/Q bands) and low-frequency (C band) visibilities were similar, the imaging and deconvolution procedures differed slightly. After calibration, the high-frequency data were Fourier inverted and then deconvolved using the multi-frequency synthesis version of the `CLEAN` algorithm with two Taylor terms to account for the flux variation of the source across each sub-band. Because of the significantly different resolutions of the VLA and SMA data of AS 205, the VLA data were tapered in the *uv*-plane with a circularly symmetric Gaussian of half-width 600 kλ. The 37.5 GHz and 30.5 GHz IF band images of AS 205 were restored with $0\farcs26 \times 0\farcs22$ (P.A. = 140.7°) and $0\farcs28 \times 0\farcs22$ (P.A. = 135.5°) synthesized beams, respectively, while the 41.0 GHz image of UX Tau was restored with a synthesized beam of $0\farcs25 \times 0\farcs20$ (P.A. = 124.1°).

As was discussed in Chapter 3, extra care had to be taken to ensure proper imaging of the C band data. Because of the increased sensitivity of the upgraded VLA, as well as the large primary beam at low frequencies (at C band, $\sim 8'$), many unrelated sources are detected within the primary beam during a typical observation. These bright sources must be deconvolved separately in order to detect faint sources that would otherwise be

masked by imaging artifacts. However, because the VLA is a non-coplanar array, the exact Fourier transform relation between visibilities and sky intensities breaks down far from the phase center. This introduces distortions to images of sources near the edge of the field, which cannot be deconvolved properly (e.g. Taylor et al. 1999). To account for outlying sources, we iteratively phase rotated the data to each of the outlying sources, `CLEAN`ed them, and subtracted each `CLEAN` model from the data set. This residual dataset was then Fourier inverted to attempt to detect the UX Tau and AS 205 systems. For the UX Tau data, ~ 5 outlying sources were imaged in this way, while for the AS 205 data, 3 sources, including a large radio galaxy with complicated structure, were imaged. With these important caveats, the remainder of the C band imaging was analogous to the high-frequency imaging. A multi-frequency synthesis imaging and deconvolution of the D array data resulted in naturally weighted 6 GHz ($\lambda = 5$ cm) maps with synthesized beams of $16\farcs5 \times 11\farcs4$ (P.A. = 179.7°) for UX Tau and $11\farcs9 \times 8\farcs45$ (P.A. = 118.6°) for AS 205. The same imaging and deconvolution performed on the A array data of the UX Tau region resulted in a synthesized beam of $0\farcs49 \times 0\farcs31$ (P.A.=147.4°). The A array data for AS 205 was not used for reasons we discuss in §4.2.4.

4.2.4 Final data products

Figures 4.1 and 4.2 show continuum emission map galleries of the AS 205 and UX Tau systems at four and two different (sub)mm/radio wavelengths, respectively. For each source, the maps were produced with different visibility weighting schemes to ensure similar synthesized beam sizes. Emission from both components of AS 205 is clearly detected at four wavelengths, from $\lambda = 0.88$ to 10 mm. The UX Tau A emission is clearly

detected and resolved at both wavelengths. No emission is detected at any mm-radio wavelength from its two companions, UX Tau B, located 5.″86 to the west, and UX Tau C, located at 2.″63 to the south (the companions are not shown in the galleries in Fig. 4.2). The AS 205 A dust emission is resolved at each wavelength, but the AS 205 B emission is point-like.

The centroids of the disks in the AS 205 system were found from fitting independent Gaussians in the image plane. The AS 205 A disk was determined from the SMA observations to be at $\alpha = 16^{\rm h}11^{\rm m}31\overset{\rm s}{.}35$, δ = -18°38′25.″99, and the disk associated with the AS 205 Bab spectroscopic binary is centered at $\alpha = 16^{\rm h}11^{\rm m}31\overset{\rm s}{.}30$, δ = -18°38′27.″08. While the absolute astrometric uncertainty of the SMA observations is $\sim 0\overset{\prime\prime}{.}1$, the differential astrometric uncertainty is much better. Ghez et al. (1993) discovered the companion AS 205 B using speckle interferometry and found a separation of $\rho = 1\overset{\prime\prime}{.}32 \pm 0\overset{\prime\prime}{.}02$ at a position angle of PA = $212^\circ \pm 1^\circ$. Furthermore, both Koresko (2002) and Eisner et al. (2005) found a consistent companion position at $\rho \approx 1\overset{\prime\prime}{.}34 \pm 0\overset{\prime\prime}{.}01$ and a position angle of PA$\approx 213^\circ \pm 2^\circ$. With our SMA map, we can also measure the separation and position angle between the millimeter-wave continuum disks: we find these are consistent with the previous observations, with $\rho_{0.88\rm mm} \approx 1\overset{\prime\prime}{.}37 \pm 0\overset{\prime\prime}{.}01$ and PA$_{0.88\rm mm} \approx 215^\circ \pm 2^\circ$.

Table 4.1 lists the basic image properties for the maps in Figures 4.1 and 4.2. Table 4.2 shows measurements of the peak and integrated flux densities for each of the emission components. The latter were determined from the visibility modeling procedures we will describe in §4.3. Figures 4.3(a) and 4.3(b) compare the mm/radio continuum spectra for each detected component of the AS 205 and UX Tau systems. In each case, the emission is dominated by thermal greybody dust radiation at $\lambda \leq 1\,$cm. At the longest radio wavelengths, the spectra start to increase and appear to be dominated by non-dust

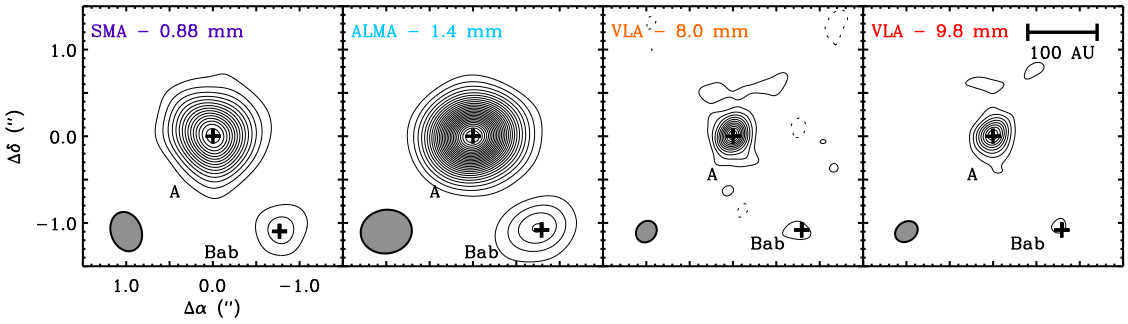

Figure 4.1: Synthesized images of the dust continuum emission from disks in the AS 205 system at four different (sub)mm–radio wavelengths. Contours in each map are drawn at $3\,\sigma$ intervals, with RMS noise levels provided in Table 4.1. The synthesized beam dimensions are shown in the lower left corner of each panel. A scale bar is marked in the fourth panel from the left. Each map spans 375 AU on a side.

emission (presumably free-free radiation from stellar or disk winds; e.g., Chiang et al. 1996; Pascucci et al. 2012). To quantify that behavior, we performed simple fits to the radio spectra for a model composed of a linear combination of two power-laws in wavelength (shown as dashed curves in Fig. 4.3) $F_\nu = a\lambda^{-\alpha_d} + b\lambda^{-\alpha_{nd}}$, where the indices α_d and $\alpha_{nd} \approx -0.6$ represent the spectral slopes in the dust and non-dust dominated regions of the spectrum, respectively. We find $\alpha_d \approx 2.75$, 2.50, and 2.34 ± 0.08 for AS 205 A, AS 205 B, and UX Tau A, respectively.

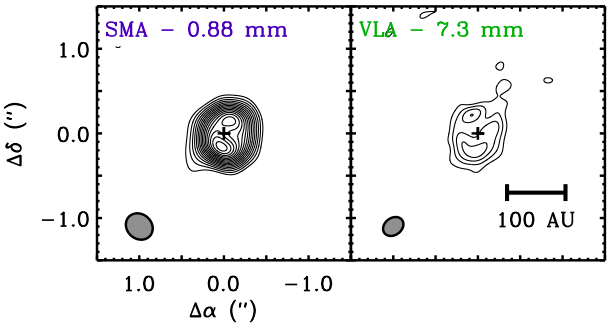

Figure 4.2: Synthesized images of the dust continuum emission from the UX Tau A disk at three different wavelengths. Contours for the 0.88 mm map start at 5σ and increment in 2σ increments, while those for the 7.3mm map start and are drawn at $3\,\sigma$ intervals. RMS noise levels provided in Table 4.1. The synthesized beam dimensions are shown in the lower left corner of each panel. A scale bar is marked in the right panel. Each map spans 435 AU on a side.

Table 4.1. Properties of Synthesized Images

System	λ (mm)	beam size (″×″)	beam P.A. (°)	map RMS (mJy beam^{-1})
AS 205 ABab	0.88	0.34×0.20	48.6	7.0
	1.4	0.59×0.50	98.1	2.5
	8.0	0.26×0.22	140.7	0.04
	9.8	0.28×0.22	135.5	0.05
	50 (D)	11.9×8.45	118.6	0.01
UX Tau	0.88	0.25×0.20	124.1	2.8
	7.3	0.25×0.20	124.1	0.02
	50 (D)	16.5×11.4	179.7	0.01
	50 (A)	0.49×0.31	147.4	0.01

Table 4.2. Peak and Integrated Flux Densities

Component	λ (mm)	peak I_ν (mJy beam^{-1})	integrated F_ν (mJy)
AS 205 A	0.88	323.0 ± 8.6	863 ± 8.6
	1.4	252.0 ± 2.5	377 ± 2.5
	8.0	1.54 ± 0.06	2.56 ± 0.06
	9.8	1.03 ± 0.04	1.67 ± 0.04
	50	0.17 ± 0.03	0.17 ± 0.03
AS 205 B	0.88	53.5 ± 5.0	86.2 ± 5.0
	1.4	36.3 ± 2.5	42.7 ± 2.5
	8.0	0.21 ± 0.06	0.29 ± 0.06
	9.8	0.15 ± 0.04	0.22 ± 0.04
UX Tau A	0.88	46.2± 2.8	150.0 ± 2.8
	7.3	0.25 ± 0.03	1.40 ± 0.03

Note. — Peak flux densities are measured directly from the maps shown in Figures 4.1 and 4.2. Except for the C band ($\lambda = 5\,$cm) and those of the AS 205 B disk, integrated flux densities are derived from the outcome of the modeling process described in §4.3 and 4.4. The C band properties were measured from maps made from the D configuration observations; the entirety of the C band D configuration flux for the AS 205 system is assigned to AS 205 A. The properties of the AS 205 B disk were measured from the synthesized images at each wavelength.

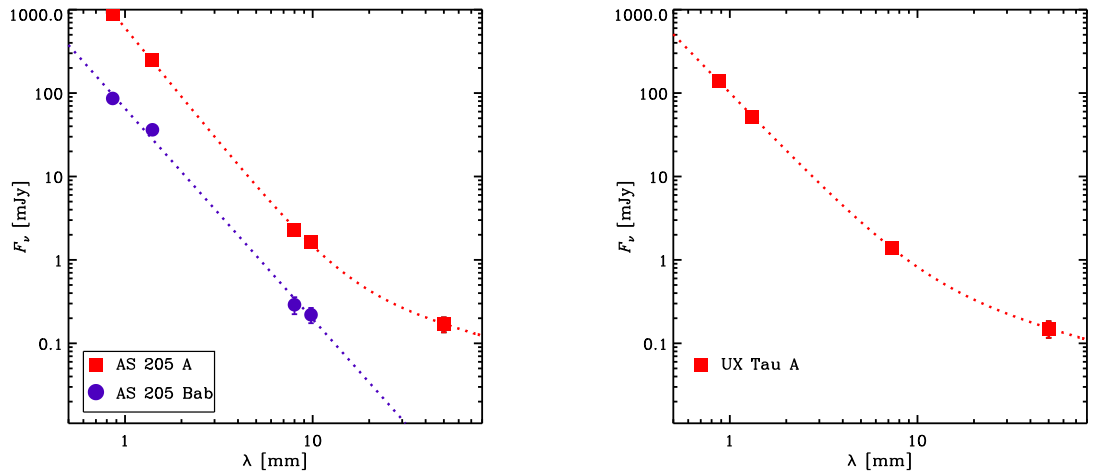

Figure 4.3: The spatially-integrated (sub)mm–radio continuum spectra for each AS 205 emission component *(left)* and for UX Tau A *(right)*; flux densities and uncertainties are derived in §4.4, and listed in Tables 4.2. Error bars are drawn, but are typically smaller than the datapoints. We assume that all of the detected C band emission derives from the primary component of each system. Dashed curves mark simple double power-law fits to the data for AS 205 A, while AS 205 B and UX Tau A were fit with a single power-law. These fits indicate that the thermal dust greybody emission dominates the spectrum out to at least 1 cm.

The normalized visibilty profile for AS 205 A in Figure 4.5 was constructed by first subtracting a model for the AS 205 B disk from the data in the *uv*-plane (see §4.3.2), then deprojecting and azimuthally-averaging the visibility profiles at each wavelength assuming that the AS 205 A disk has an inclination $i = 30°$ and major axis P.A = 120°. These geometric parameters were estimated from the optically thin ^{13}CO($J = 2 - 1$) emission from the gas disk, shown in Figure 4.4. These parameters are different than those derived by Andrews et al. (2009) for the source based on SMA observations of ^{12}CO($J = 3 - 2$) emission that was contaminated by both the secondary disk and the surrounding cloud. The visibility profile for UX Tau A in Figure 4.6 merely required deprojection and azimuthal averaging, as no other sources were detected at any wavelength. The geometry assumed for the UX Tau A disk was an inclination $i = 25°$ and PA = 176° (Andrews et al. 2011).

The low-frequency C band data from different observations are discrepant. A map made from the D configuration data shows several background radio galaxies, as well as a tentative detection of a point source coincident with the position of UX Tau with an integrated flux density of ~ 150 μJy. However, the A array data shows no evidence for radio emission in the vicinity of UX Tau. Each source detected in the D configuration map, with the exception of UX Tau, is detected in the A configuration map with flux densities consistent between the two maps.

There are three potential causes for this discrepancy. First, if the D configuration detection is real, then the A configuration could sufficiently resolve the emission out so that it is below the surface brightness threshold of the data. This would be expected if this were thermal dust emission from the disk. The spectral curvature in Fig. 4.3(b) seems to rule this out, however. Furthermore, maps of the A configuration data were

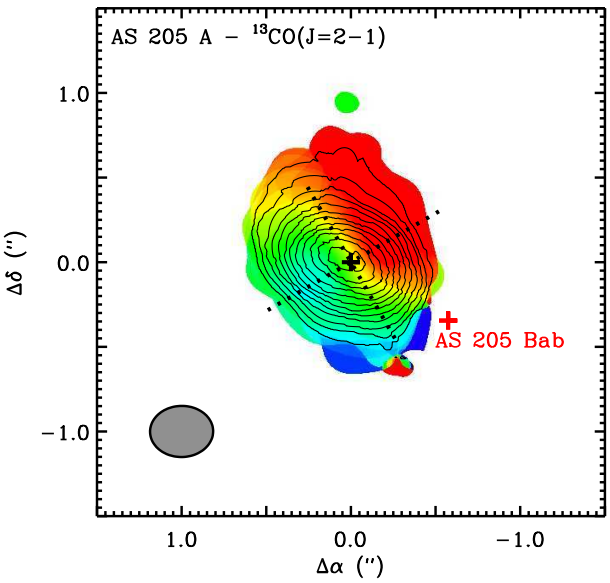

Figure 4.4: Integrated intensity (*contours*) and average velocity (*color*) of the ^{13}CO($J = 2 - 1$) line emission from the AS 205 A disk. The black cross indicates the location of the primary while the red indicates that of the secondary. The colors range from 3 to 5 km/s. The dashed axes indicate the orientation and inclination of the disk, assuming an intrinsic circular geometry. An inclination of $\sim 30°$ and position angle of $\sim$120° appear to describe the disk geometry well.

made with Gaussian tapers of 200kλ and 400kλ, to place more weight on larger spatial scales, but no sources were detected in those maps either. If the emission is real and not from dust, it could be thermal brehmstrahlung from an outflow or emission from the stellar corona. However, stellar emission would be completely unresolved and outflow emission would be marginally resolved, if at all, so resolution effects should not cause the discrepancy. Second, the detection could be spurious. However, the D configuration detection is made at a $\sim 5\sigma$ level, and the coincidence with the UX Tau location strongly suggests otherwise. The final option is that the C band emission could be time-variable. Centimeter-band variability on $\sim$ month timescales has been observed

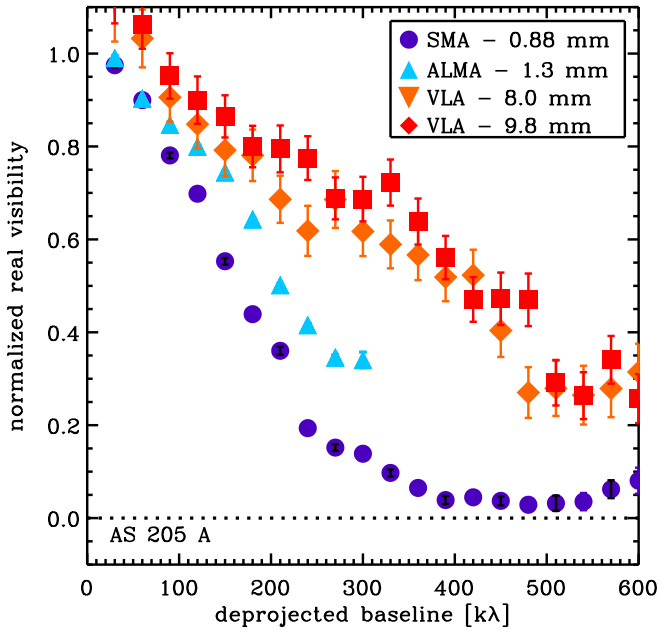

Figure 4.5: The normalized real visibility profiles for the emission from the AS 205 A dust disk at each (sub)mm–radio wavelength. The visibilities have been azimuthally-averaged and deprojected according to the disk viewing geometry, as a function of baseline length (within the noise, the imaginary amplitudes are all consistent with zero). The differences between the visibility profiles at 0.88, 1.4, 8.0, and 9.8 mm are striking and reflect the fact that emission morphology becomes more compact at longer wavelengths. The data are binned into overlapping 60 kλ bins. The procedure by which the AS 205 A visibilty profile was produced from the AS 205 AB data is outlined in §4.3.2.

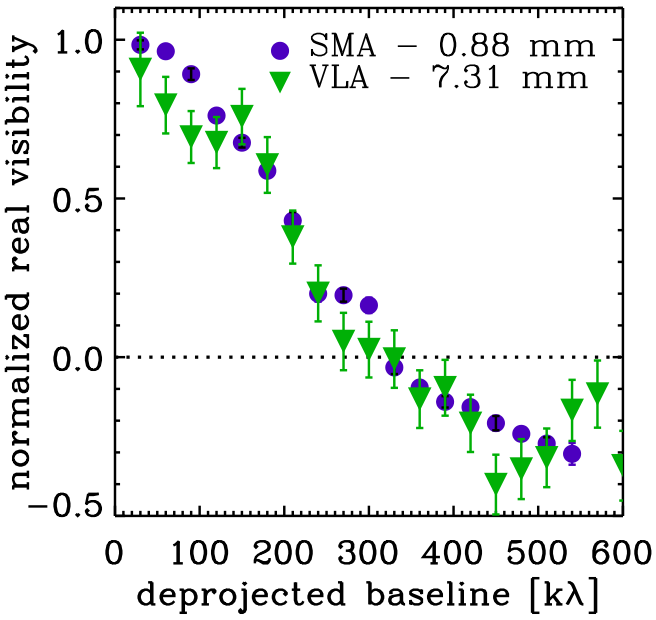

Figure 4.6: The normalized real visibility profiles for the emission from the UX Tau A disk at each (sub)mm–radio wavelength. The visibilities have been azimuthally-averaged and deprojected according to the disk viewing geometry, as a function of baseline length (within the noise, the imaginary amplitudes are all consistent with zero). For UX Tau A, the difference is not as striking as that in the AS 205 A disk: the structure of the disk, both the extent and cavity size, as indicated by the half-power point and null of the visibility profile, respectively, appear similar. The data are binned into overlapping 60 kλ bins.

before, particularly in diskless weak-lined T Tauri stars (WTTS) (e.g. DoAr 21; Feigelson & Montmerle 1985). We note that UX Tau Bab is comprised of a pair of WTTS and has been detected in VLA observations at 3.6 cm at a flux density of approximately 0.1 mJy (Chiang et al. 1996).

The observations of AS 205 at C band were similarly complicated. A ~ 170 μJy point source was detected coincident with the AS 205 system in the D configuration. However, the presence of a very large and bright radio galaxy several arcminutes to the west prevented high-fidelity imaging of the field using the A configuration data alone. Artifacts deriving from the inadequately sampled *uv*-plane caused ripples throughout the map that masked the emission from the other point sources in the field. This interfered with our ability to assess time variability of the C band emission, as well as our effort to isolate which component it originated from.

These complications present difficulties for robustly determining the dust disk properties at the centimeter bands. We defer further discussion of the complications related to the characterization of C-band emission to our modeling efforts to §4.4.4.

4.3 Modeling Analysis

The multi-wavelength observations of the disks in the AS 205 and UX Tau multiple systems show somewhat different behavior. The size of the AS 205 A continuum emission is anti-correlated with the observing wavelength. This can be seen by examination of the images (Figure 4.1) or by examining how steeply the visibility profile falls off with *uv*-distance (Figure 4.5). Similar behavior has been observed in the UZ Tau E disk

(Chapter 3) and in the disk around AS 209 (Pérez et al. 2012). However, neither the cavity size nor the emission extent of the UX Tau A disk seems to strongly depend on the observing wavelength in the images (Figure 4.2) or the shapes of the visibility profiles (Figure 4.6; comparison of the cavity sizes at each wavelength can be made by examining the locations of the intersection of the profile with zero).

In order to quantify these statements about the wavelength dependence of the emission size, we use parameterized models for the disk emission to model the continuum visibilities of each disk at each wavelength and characterize the optical depth profiles, $\tau_\nu(r)$, and then the millimeter colors. These derived millimeter colors will allow us to determine to what extent grain sizes vary across the disk. First, in §4.3.1 we review the physical basis for our modeling methodology and our adopted parameterizations for the disk structures, which were more thoroughly described in Chapter 3 (§3.3). We describe the modifications that are made to the models and their parameterizations for the AS 205 and UX Tau systems, as compared to how they were applied to the UZ Tau system in §4.3.2. Finally, in §4.3.3 we will discuss the incorporation of the information from the C band observations of both systems into our models.

4.3.1 Modeling summary

A model of the thermal dust continuum emission from a protoplanetary disk is completely specified by the spatial distributions of dust temperatures $T(r, z)$ and densities $\rho(r, z)$, as well as the dust opacities $\kappa_\nu(r, z)$, assuming azimuthal symmetry. For a vertically isothermal disk evolving viscously in vertical hydrostatic equilibrium, the disk surface

density profile ($\Sigma(r) = \int_{-\infty}^{\infty} \rho(r,z)dz$) is given by

$$\Sigma(r) = \Sigma_c \left(\frac{r}{r_c}\right)^{-\gamma} \exp\left[-\left(\frac{r}{r_c}\right)^{2-\gamma}\right], \tag{4.2}$$

where r_c is a characteristic radius, γ is a gradient, and Σ_c is a normalization (Lynden-Bell & Pringle 1974; Hartmann et al. 1998).

To generate the observationally relevant quantity, the surface brightness profile $I_\nu(r)$, from the model parameterization, we integrate the radiative transfer equation along each sight-line to the disk, i.e.

$$I_\nu(r) = \int_0^\infty K_\nu(s) S_\nu(s) e^{-\tau_\nu(s)} ds, \tag{4.3}$$

where $K_\nu \propto \kappa_\nu \rho$ is the absorption coefficient of the material, $S_\nu(s)$ is the source function of the medium, and $\tau_\nu(s)$ is the integrated optical depth of the material to some point s along the sight-line. In our case, S_ν is defined as the Planck function $B_\nu(T(r))$. The opacity $\kappa_\nu(s)$ is dominated by dust, which contributes to κ_ν in a size-dependent manner. Dust grains of size $a \sim$ the observing wavelength λ contribute the most to the opacity κ_ν. For a population of dust with sizes $a \ll \lambda$, the opacity scales as λ^{-2} due to Rayleigh scattering, while for a population of dust grains with $a \gg \lambda$, κ_ν is roughly constant. The total dust opacity is determined by taking a size-weighted average of the opacities from a distribution of grains.

The main difficulty in modeling resolved disk structures at millimeter- and centimeter-wave bands are the highly uncertain opacities. Studies of resolved disk structures have typically proceeded by assuming that $\Sigma(r)$ is described by Eq. 4.2 and that κ_ν is constant throughout the disk (e.g., Kitamura et al. 2002; Andrews et al. 2009, 2010). Then, $\tau_\nu(r)$ merely reflects the underlying surface density distribution,

because $\tau_\nu(r) = \kappa_\nu(r)\Sigma(r)$. However, there is no particular reason why κ_ν should be independent of radius. In fact, there are theoretical reasons to expect that the grain-size distribution varies with radius. Based on numerical simulations of dust grain growth in protoplanetary disks, Birnstiel et al. (2011) proposed a model that implies that κ_ν can be reasonably described as a power-law in radius, i.e.

$$\kappa_\nu(r) = \kappa_{c,\nu} r^\xi, \tag{4.4}$$

where $\kappa_{c,\nu}$ is some characteristic opacity, and ξ is a gradient parameter.

Because of the uncertainty about the proper model to use for opacity, we fit our data with three general parametric models. The first is what we term *Scenario A*, where γ is free, but the opacity κ_ν is fixed in both frequency and radius. This case has often been used to successfully model disks at (sub)millimeter wavelengths (e.g., Kitamura et al. 2002; Hughes et al. 2008; Andrews et al. 2009, 2010, 2011; Isella et al. 2009, 2010; Guilloteau et al. 2011). In Chapter 3, we introduced two other models: *Scenario B*, where ξ is allowed to vary, but γ is fixed to unity; and *Scenario C*, where both γ and ξ are allowed to vary. Once an opacity spectrum $\kappa_\nu(r)$ and a temperture law $T(r)$ are chosen, the model parameters $\{\Sigma_c, r_c, \gamma, \xi\}$ and disk geometry $\{i$,PA$\}$ completely specify the sky brightness distribution of the disk, $I_\nu(r)$.

For each parametric model, we use a computationally efficient implementation of Markov-chain Monte Carlo simulation (`emcee`; Foreman-Mackey et al. 2013) to fit the continuum visibilities at each wavelength and derive probability distributions for the model parameters. At each step in the Markov chain, parameter values are set, the resulting sky brightness I_ν is then projected onto a grid tangent to the plane of the sky, and then Fourier inverted and sampled at the same uv locations as the data. The

log-likelihood that determines the probability of jumping to a different set of parameter values is then computed as $\propto -\chi^2/2$. The constant of proportionality is derived by scaling the nominal visibility weights as discussed in Chapter 3. Uniform priors are made on the all parameters, with bounds where physical motivations demand them (e.g., disk radii and optical depth normalizations are non-negative).

4.3.2 Modeling complications

Some complications specific to these two disk systems studied here require adjustments to the modeling techniques described above. First, to model the UX Tau disk, we need to take into account the large central cavity in the millimeter continuum emission from the disk. Andrews et al. (2011) noted that the cavity radius was $\sim$ 25 AU at 880 μm. We modify our parametrization by setting the optical depth within some radius $r_{\rm cavity}$ to zero, and then fitting for the free parameters $\{\Sigma_c, r_c, \gamma, \xi, r_{\rm cavity}\}$. The AS 205 disk has no evidence for a cavity, so we only fit for $\{\Sigma_c, r_c, \gamma, \xi\}$, as was done in Chapter 3 for UZ Tau.

Second, both disks in the AS 205 system were strongly detected at both 880 μm and 1.4 mm. Because the main focus of this work is on the disk surrounding AS 205 A, we subtracted a model for the AS 205 B disk from the total dataset before modeling. The model of the AS 205 B disk was constructed from the `CLEAN` components found for AS 205 B during deconvolution. The `CLEAN` algorithm was allowed to find components down to $\sim$ 7 mJy at 880μm and $\sim$ 5 mJy at 1.4 mm. We found previously when modeling the UZ Tau system, in which the primary disk has two bright companions, that our quantitative results did not significantly depend on the model that we used for the

emission from the companions if no significant residuals remained after their subtraction (see §3.4.3). The total CLEANed flux density recovered during the deconvolution of the AS 205 B disk from the original SMA dataset was $\sim$ 80 mJy, while that recovered for the ALMA dataset was $\sim$ 40 mJy. This is within the uncertainty of the total integrated flux density for the disk derived from our image plane fitting (see Table 4.2), so we have confidence that any remaining signatures of the AS 205 B disk are minimal.

4.3.3 Temperatures and the contribution of non-dust emission

The two principal systematic uncertainties in determining the variation of optical depth with radius in our approach lie in the uncertain temperature distribution, $T(r)$, and the contribution of non-dust emission to the overall radio emission at the Ka and Q bands.

In this work, we adopt the temperature profiles that were constructed by a previous simultaneous fitting of the spectral energy distribution and the 880 μm visibility profiles (AS 205, Andrews et al. 2009; UX Tau A, Andrews et al. 2011).

The temperature profile assumed for the UX Tau A dust disk has

$$T(r) = 45 \left(\frac{r}{10 \text{ AU}}\right)^{-0.3} \text{ K},$$

while that for the AS 205 dust disk takes on a broken power-law form, with

$$T(r) = 70 \left(\frac{r}{10 \text{ AU}}\right)^{-0.6} \text{ K}$$

until $r = 120$ AU, at which point the power-law flattens to $q = 0.4$.

Assessing the contamination from non-dust emission sources at centimeter-wavelengths in the two disks is a difficult, but crucial task. As was described in §3.4.2

of this thesis, there is a degeneracy between the best-fit optical depth profile, $\tau_\nu(r)$, at Ka/Q bands and the assumed contribution of point-source emission at the disk center. A higher such contribution leads to a fainter and more centrally concentrated optical depth profile. Thus, an overestimate of the non-dust emission at centimeter wavelengths will cause an artificially red millimeter/radio color, both in the inner disk and outer disk. This can make a robust estimate of the $\beta(r)$ profile difficult.

For the UX Tau A dust disk, we assumed negligible contribution from free-free emission at centimeter-wavelengths for three reasons. First, while we detected a source at ~ 150 μJy coincident with UX Tau A in a $\sim 12''$ resolution VLA C-band map, a $\sim 0\farcs5$-resolution C-band map yielded no such detection, despite the fact that the expected level of emission should have been seen at ~ 10 σ. Second, there has been no detection of UX Tau A at any centimeter wavelength, but there has been a detection of long-wavelength emission from its $5\farcs6$-separation companion UX Tau B ($\sim$ 2.0 mJy at 3.6 cm; Chiang et al. 1996). Third, the non-dust emission from stellar sources is expected to be relatively flat or rising with frequency, if it comes from thermal free-free emission (with a spectral index of $\sim$ -0.1 to 0.6), or falling if the emission is synchrotron (with the spectral index related to the energy distribution of electrons generating the emission; typically -0.7). No matter the exact spectral index, if the emission detected in the low-resolution C-band map were non-dust emission from UX Tau A, its extrapolation to the higher-frequency Ka band data would allow a point source at the center to be detected above the level of the dust. But, there is no signature of such a point source in either the maps or the visibilities, supporting our initial assumption.

The assessment of the non-dust contribution to the AS 205 A emission is more complicated. A 170 μJy point source component was detected at the AS 205 location

in $\sim 12''$ resolution VLA C-band observations. However the difficulties of imaging the complicated structure of a nearby bright radio galaxy prevented us from determining the AS205 A flux density from the $0''.5$-resolution data. Therefore, we examined the visibility profiles at 8.0 and 9.8 mm to make a determination of the proper non-dust contribution to assume at these bands. By examining the flux level offset of the visibility curve at long baselines, we can ignore the (resolved-out) contribution of the disk and be assured that we are only seeing the contribution of point-like emission. Examination of the normalized visibilities suggested that as much as $\sim 20\%$ and $\sim 30\%$ of the emission at 8.0 mm and 9.8 mm, respectively, could be due to point-like non-dust emission. Surprisingly, the values estimated in this way for the non-dust emission are approximately those expected from the low-resolution C-band observations if the emission were coming from optically thick thermal free-free emission ($S_\nu \propto \nu^{0.6}$). So, to be conservative, we estimated the non-dust contribution to the 8.0 and 9.8 mm emission at 500 and 440 μJy, respectively.

4.4 Results

We present the results of our parametric modeling analysis for each disk and combination of modeling scenario and wavelength in Tables 4.3 and 4.4. These tables list the best-fit values for each combination of model and parameter, along with its associated marginalized 68% confidence interval, for our choice of the temperature profiles given in §4.3.3. We also present the results for the derived quantities $\tau_\nu(r)$ and $\beta(r)$. First, we describe how we derived these quantities from the parameter values returned by the MCMC simulations, and then we discuss the results for each source in turn.

Table 4.3. Estimates of Model Parameters for AS 205 A

Model	λ (mm)	$\tau_{0,\nu}$ (at 10 AU)	r_c (AU)	γ	ξ
A	0.88	0.804 ± 0.02	48.9 ± 0.6	-0.32 ± 0.035	0 (fixed)
	1.4	2.23 ± 0.10	32.7 ± 0.2	0.02 ± 0.096	0 (fixed)
	8.0	0.371± 0.041	17.3 ± 0.5	-1.46 ± 0.16	0 (fixed)
	9.8	0.227 ± 0.022	18.6 ± 0.3	-3.12 ± 0.25	0 (fixed)
B	0.88	0.845 ± 0.024	12.9 ± 0.5	1 (fixed)	2.49 ± 0.09
	1.4	2.57± 0.13	10.0 ± 0.13	1 (fixed)	1.97 ± 0.07
	8.0	0.344± 0.014	2.8± 0.5	1 (fixed)	5.0 ± 0.71
	9.8	0.297 ± 0.011	1.8 ± 0.4	1 (fixed)	9.3 ± 1.6
C	0.88	0.821 ± 0.017	17.0 ± 3.9	0.89 ± 0.10	2.18 ± 0.28
	1.4	0.040 ± 0.20	23.0 ± 5.5	-0.62 ± 0.59	2.52 ± 0.55
	8.0	0.385 ± 0.030	6.2 ± 4.2	0.69± 0.44	3.64 ± 1.2
	9.8	0.258 ± 0.018	7.3 ± 4.2	0.31 ± 0.59	6.13 ± 2.0

Note. — This compilation assumes the fiducial radial temperature profile and non-disk contamination in the Ka band. See §4.4.1 and 4.4.2 regarding the effects of these assumptions on the model behaviors. The $\sim$ 10% systematic uncertainty in the amplitude scale has not been taken into account in the errors.

Table 4.4. Estimates of Model Parameters for UX Tau A

Model	λ (mm)	$\tau_{0,\nu}$ (at 30 AU)	r_c (AU)	γ	ξ	r_i (AU)
A	0.88	0.241 ± 0.0175	42.25 ± 1.13	-1.54 ± 0.44	0 (fixed)	10.69 ± 6.89
	7.3	0.123 ± 0.0153	39.69 ± 1.57	-2.38 ± 0.83	0 (fixed)	10.85 ± 7.71
B	0.88	0.406 ± 0.018	8.66 ± 1.79	1 (fixed)	2.16 ± 0.88	23.29 ± 0.21
	7.3	0.196 ± 0.040	12.17 ± 5.26	1 (fixed)	0.65 ± 1.24	24.62 ± 1.72
C	0.88	0.393 ± 0.050	30.08 ± 7.28	-0.19 ± 0.95	0.88 ± 0.58	22.97 ± 2.13
	7.3	0.160 ± 0.026	40.22 ± 3.28	-2.64 ± 1.32	-0.25 ± 0.90	13.02± 8.59

Note. — This compilation assumes the fiducial radial temperature profile and non-disk contamination in the Ka band. See §4.4.1 and 4.4.2 regarding the effects of these assumptions on the model behaviors. The $\sim$ 10% systematic uncertainty in the amplitude scale has not been taken into account in the errors.

4.4.1 Derivation of $\tau_\nu(r)$ and $\beta(r)$

The outputs of the MCMC simulations of the continuum visibilities are samples of the joint posterior distribution of the parameters $\{\Sigma_c, r_c, \gamma, \xi\}$ for the AS 205 A dust disk, and $\{\Sigma_c, r_c, \gamma, \xi, r_{\rm cavity}\}$ for the UX Tau A dust disk. To arrive at distributions of $\tau_\nu(r)$ from these samples, we sample these joint distributions, and compute $\tau_\nu(r)$ for each disk radius. For AS 205 A, each sample of the distribution yields the optical depth profile

$$\tau_\nu(r) = \kappa_{\nu,c}\Sigma_c \left(\frac{r}{10\mathrm{AU}}\right)^{\xi} \left(\frac{r}{r_c}\right)^{-\gamma} \exp\left[-\left(\frac{r}{r_c}\right)^{2-\gamma}\right], \tag{4.5}$$

while for the UX Tau A disk, each sample yields the profile

$$\tau_\nu(r) = \begin{cases} \kappa_{\nu,c}\Sigma_c \left(\frac{r}{10\mathrm{AU}}\right)^{\xi} \left(\frac{r}{r_c}\right)^{-\gamma} \exp\left[-\left(\frac{r}{r_c}\right)^{2-\gamma}\right] & \text{if } r > r_{\rm cavity} \\ 0 & \text{otherwise} \end{cases}$$

We randomly sample the parameter posterior probability distribution many times and construct the full posterior distribution of τ_ν at each combination of disk radius and wavelength from these samples.

The posterior distribution of $\beta(r)$ is computed in the same fashion. We randomly choose samples from the MCMC simulation, construct for each radius $\{\tau_{0.88\mathrm{mm}}, \tau_{1.4\mathrm{mm}}, \tau_{8.0\mathrm{mm}}, \tau_{9.8\mathrm{mm}}\}$ (for the AS 205 A disk) and $\{\tau_{0.88\mathrm{mm}}, \tau_{7.3\mathrm{mm}}\}$ (for the UX Tau A disk), and fit these to the functional form

$$\log \tau_\nu(r) = A + \beta(r) \log \nu \tag{4.6}$$

where A sets the flux density level and $\beta(r)$ is the quantity of interest. The uncertainty we assign to τ_ν that yielding a 10% amplitude uncertainty at each band. This process

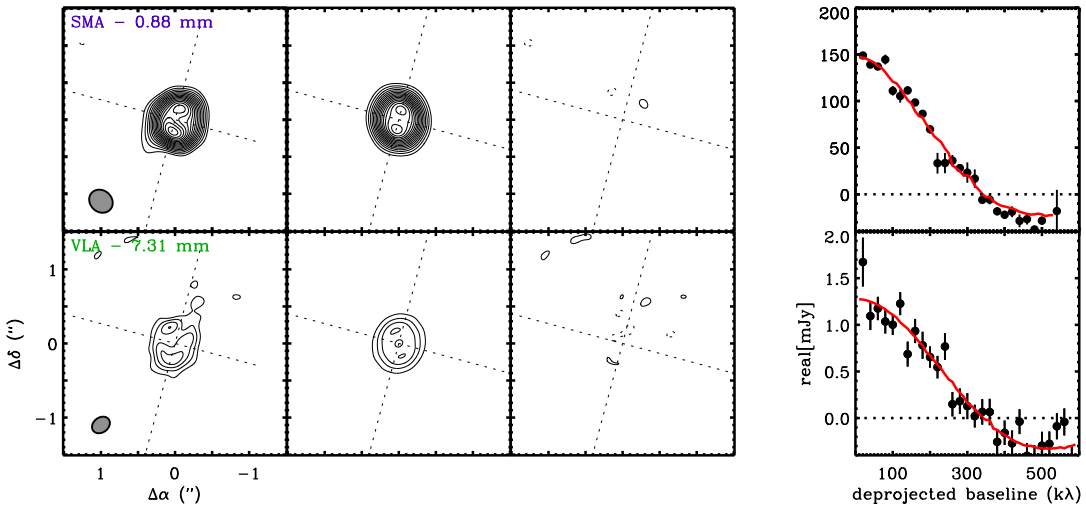

Figure 4.7: (*left*) An image-plane comparison of the UX Tau data, best-fit model from *Scenario B* (synthesized in the same way as the data), and the imaged residual visibilities (as in Fig. 4.2). Dashed crosshairs mark the disk center and orientation. (*right*) The azimuthally-averaged (real) visibilities as a function of deprojected baseline for each observing frequency (as in Fig. 4.6), compared with the best-fit models for *Scenario B*. The results for *Scenario A* and *C* are similar.

is repeated many times, and the posterior distribution of the profiles of $\beta(r)$ are constructed.

4.4.2 UX Tau

Figure 4.7 compares the synthesized images of the data, the best-fit model, and the residuals for the UX Tau A disk. We only show those comparisons for *Scenario B*, although the results for *Scenario A* and *Scenario C* are almost indistinguishable in both the image and *uv*-plane.

Figure 4.8 shows the resulting optical depth profiles derived for the UX Tau A disk for our chosen temperature law. These profiles clearly show that the disk is optically thin at both 0.88 and 7.3 mm, and that the disk has a prominent opacity deficit in the central regions, consistent with an inner cavity of $\sim 20 - 25$ AU radial extent. However, the emission region is only slightly more compact, if at all, at 7.3 mm than at 0.88 mm. This is clear from an examination of the visibility profiles in Figure 4.6, since they are not noticeably different at the two wavelengths.

We use these results to quantify limits on the relative compactness of the 7.3 mm emission as compared to the 0.88 mm emission by examination of the opacity spectral index. We plot the derived constraints on $\beta(r)$ in Figure 4.9 for our *Scenario B* (the other two model scenarios are qualitatively similar, within the uncertainties). It is clear that the mm-radio color of the UX Tau A disk does not significantly vary across the narrow radial extent of the ring-like morphology of the disk.

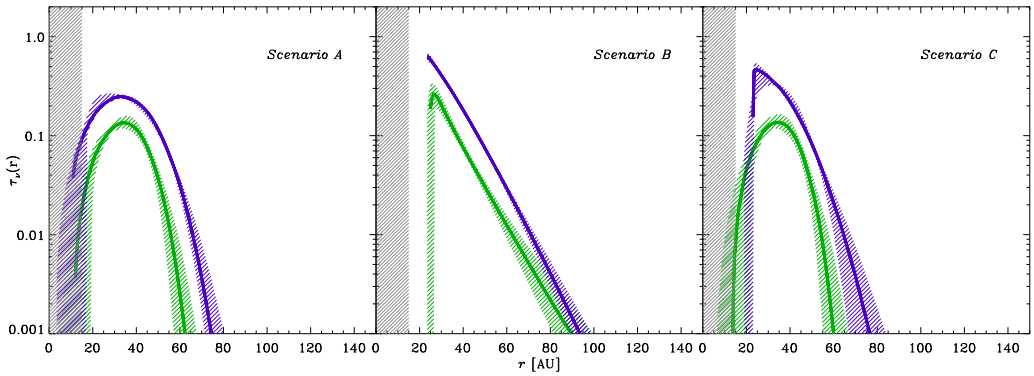

Figure 4.8: The derived optical depth profiles, $\tau_\nu(r)$, for both observing frequencies (0.88 mm - purple; 7.3 mm - green) and each modeling scenario for UX Tau A. The best-fit profiles are shown as thick lines; shaded regions mark the 99.7% confidence intervals. The mean resolution limit of our data is denoted by a gray shaded rectangle, marking the typical angular resolution. Information on $\tau_\lambda(r)$ inside the shaded region is based on model extrapolations and are not directly constrained by the data.

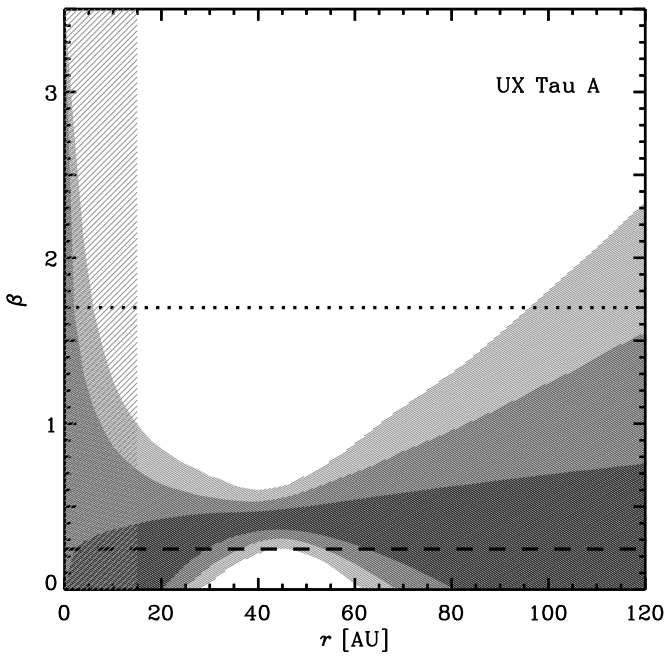

Figure 4.9: Constraints on the spatially-resolved profile of $\beta(r)$ for the UX Tau A transition disk for our *Scenario B*. The shaded regions correspond to 68, 95, and 99.7 % confidence regions. The shaded box on the left denotes the mean resolution limit of the data. The thick dashed line gives the disk-averaged value of β while the dotted line gives the estimate for the value derived for unevolved grains in the interstellar medium, $\beta_{\rm ISM} \sim 1.7$. The uncertainties incorporate a 10% amplitude uncertainty at both wavelengths, inflating the uncertainty for β by ~ 0.1.

4.4.3 AS 205

Figure 4.10 compares the synthesized images of the data, the best-fit model, and the residuals for the AS 205 A disk. We only show those comparisons for our *Scenario B*. The results from *Scenario A* and *Scenario C* are almost identical to those presented here.

Figure 4.11 shows the resulting optical depth profiles derived for the AS 205 A disk for our chosen temperature law. It is noteworthy that the disk has moderate optical depth ($\tau \sim 1$) at 0.88 mm, even at intermediate radii ($\sim 20 - 50$ AU). This is not unexpected, as the disk is very bright at this wavelength ($F_{0.88\mathrm{mm}} = 960$ mJy). The shape of the optical depth profile at 1.4 mm (in particular its increase above that of the 0.88 mm optical depth in the inner disk) is presumably an artifact due to the poorer resolution of the 1.4 mm data. The disk is optically thin at both 8.0 and 9.8 mm outside the effective resolution limit of the VLA data. Also, it is noteworthy that, in this case, the AS 205 A disk is notably more compact at centimeter-bands than in the submillimeter.

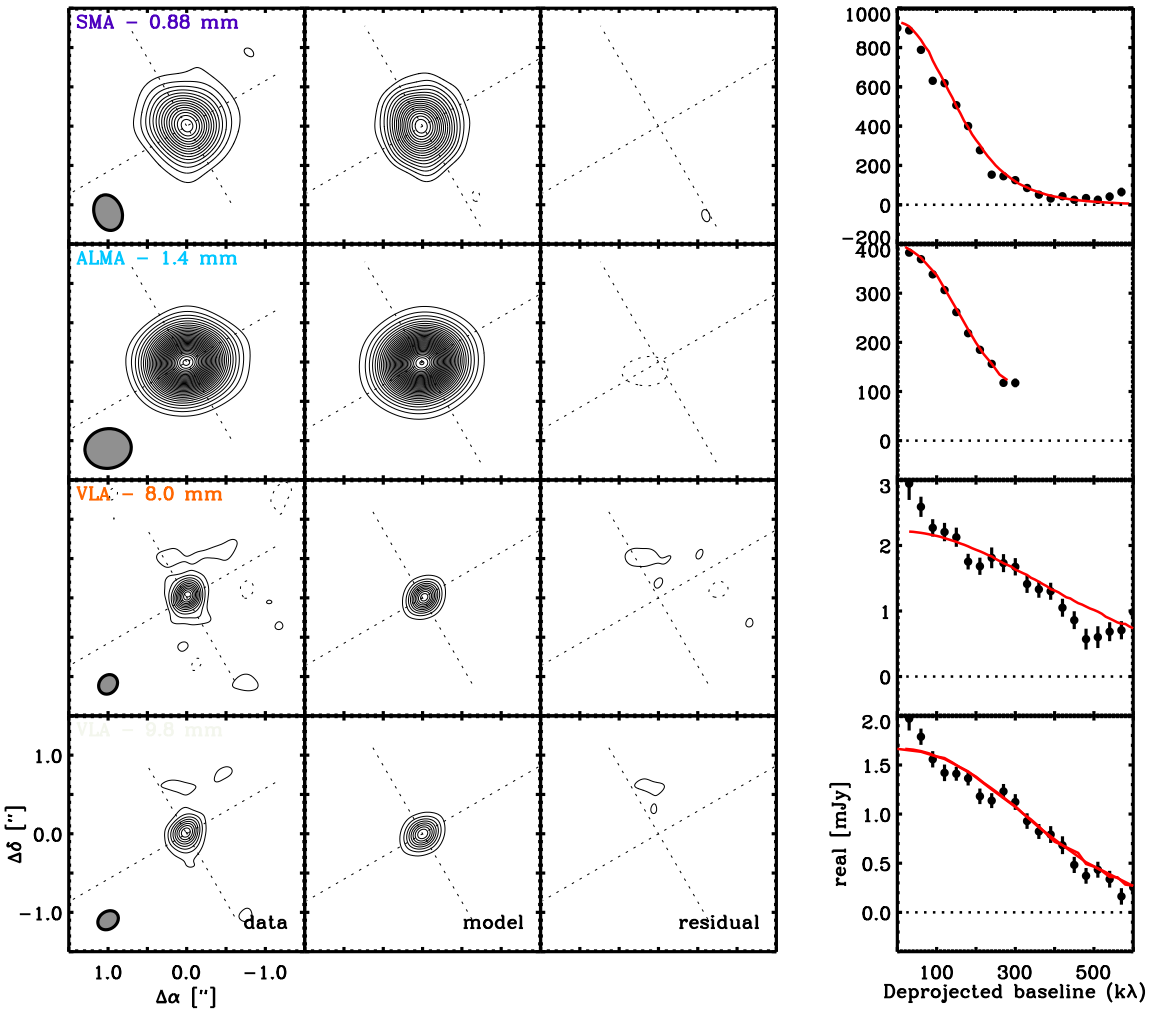

Figure 4.10: (*left*) An image-plane comparison of the AS 205 A data (after subtraction of a model for the AS 205 B emission), best-fit model from *Scenario B* (synthesized in the same way as the data), and the imaged residual visibilities (as in Fig. 3.1). Dashed crosshairs mark the disk center and orientation. (*right*) The azimuthally-averaged (real) visibilities as a function of deprojected baseline for each observing frequency (as in Fig. 4.5), compared with the best-fit models for *Scenario B*. The results for *Scenario A* and *C* are similar.

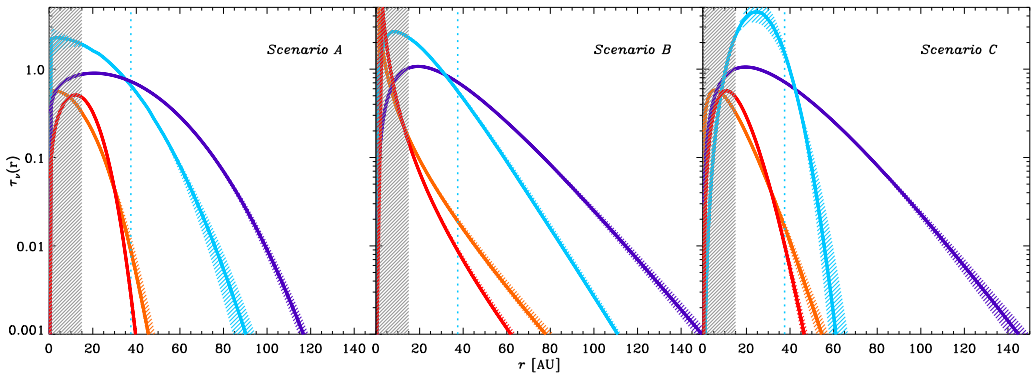

Figure 4.11: The derived optical depth profiles, $\tau_\nu(r)$, for each observing frequency (0.88 mm - purple; 1.4 mm - blue; 8.0 mm - orange; 9.8 mm - red) and modeling scenario for AS 205 A. The best-fit profiles are shown as thick lines; shaded regions mark the 99.7% confidence intervals. The mean resolution limit of our data (excluding the comparatively poor resolution 1.4 mm data) is denoted by a gray shaded rectangle, marking the typical angular resolution. The resolution of the 1.4 mm data is indicated by a dotted blue line. Information on $\tau_\lambda(r)$ inside the shaded region is based on model extrapolations and therefore not directly constrained by the data.

We plot the derived constraints on $\beta(r)$ in Figure 4.12 for *Scenario B*. The constraints derived on β assuming the other two scenarios are qualitatively the same. It is clear from the plot that the variations of β within the disk are significant and large, trending from ~ 0.5 at the resolution limit of our data to ISM values at only $r \sim 40$ AU.

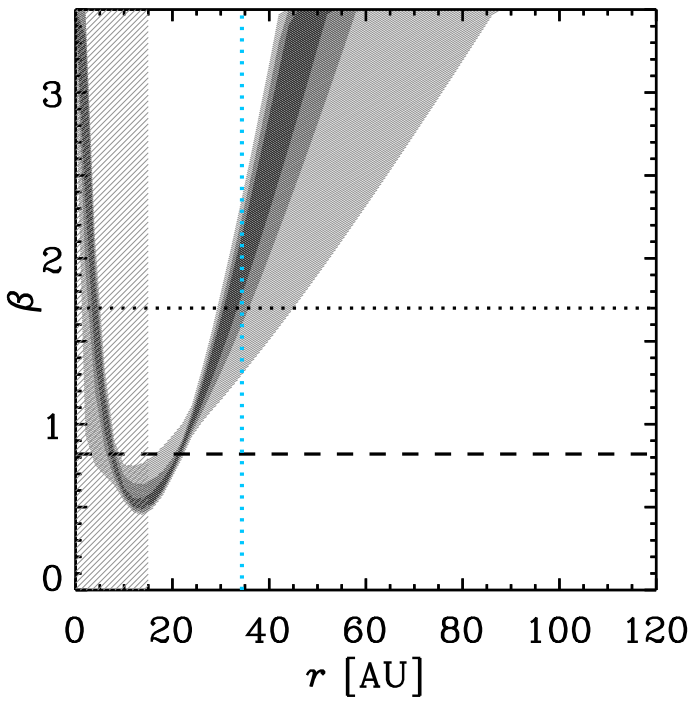

Figure 4.12: Constraints on the spatially-resolved profile of $\beta(r)$ for the AS 205 disk for our *Scenario B*. The shaded regions correspond to 68, 95, and 99.7% confidence regions. The shaded box on the left denotes the mean resolution limit of the data (excluding the 1.4 mm ALMA data), while the dotted blue line indicates the resolution of the 1.4 mm ALMA data. The thick dashed line gives the disk-averaged value of β while the dotted line gives the estimate for the value derived for unevolved grains in the interstellar medium, $\beta_{\rm ISM} \sim 1.7$. The uncertainties incorporate a 10% amplitude uncertainty.

4.4.4 Contamination from non-dust emission and the impact of temperature uncertainty

To demonstrate that an imprecise estimate of non-dust emission does not qualitatively affect our results for the AS 205 A disk, we have repeated our analysis assuming that the non-dust emission has a flat spectrum (S_ν constant in frequency). The derived constraints on the $\beta(r)$ profile are shown in Figure 4.13. It is clear that, while the range that $\beta(r)$ can take in the disk is affected, as is the exact location where $\beta(r)$ becomes approximately the ISM value, the trend of increasing $\beta(r)$ is unchanged.

In principle, our determination of the $\beta(r)$ profiles for each disk could be compromised by our imprecise knowledge of the temperature profile. In the simple case where low optical depth conditions and the Rayleigh-Jeans limit prevail across the disks at all frequencies, then to first-order the best-fit optical depths should merely shift with a change in temperature, and the best-fit values of β should be unaffected. These conditions hold mostly in the UX Tau A disk where there is sufficient signal to detect the continuum emission. However, for the AS 205 A disk, the Rayleigh-Jeans criterion is not applicable in the outer disk, while the low optical depth condition is not satisfied in the inner disk. However, the transition of the $\beta(r)$ profiles for the AS 205 A dust disk to ISM-like values of β occurs at $\sim$ 40-50 AU, well within the region where we expect the Rayleigh-Jeans limit to hold (out to $\sim$ 100 AU).

If the local temperature is incorrect, the fractional change in the optical depth required to reach the same surface brightness is given approximately by the fractional error in the temperature times the factor $\sim (1 + \tau_\nu/2 + \tau_\nu^2/6...) \sim O(2)$. At the long wavelengths, then, a temperature off by a factor of ~ 2 will yield an optical depth off by

a factor of ~ 2, while at the shorter wavelengths, the same temperature error will yield an optical depth error of a factor of ~ 4. Fortunately, the lever arm between 0.88 and 9.8 mm is such that this corresponds to an error in β of only ~ 0.3, much less than the variation we see in the source. For these reasons, we believe our qualitative result to be robust against errors in the temperature profile.

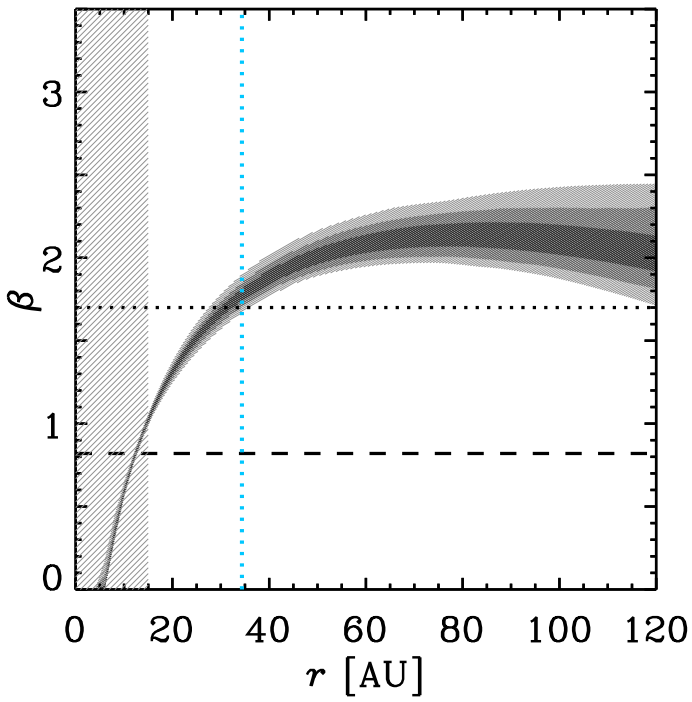

Figure 4.13: Constraints on the spatially-resolved profile of $\beta(r)$ for the AS 205 disk for our *Scenario B*, assuming a 170 μJy contribution of non-dust emission to the total emission at 8.0 and 9.8 mm. The shaded regions correspond to 68, 95, and 99.7% confidence regions. The shaded box on the left denotes the mean resolution limit of the data (excluding the 1.4 mm ALMA data), while the dotted blue line indicates the resolution of the 1.4 mm ALMA data. The thick dashed line gives the disk-averaged value of β while the dotted line gives the estimate for the value derived for unevolved grains in the interstellar medium, $\beta_{\rm ISM} \sim 1.7$. The uncertainties incorporate a 10% amplitude uncertainty at each wavelength.

4.5 Discussion

We have presented sensitive, high-resolution observations at submillimeter and radio wavelengths of the thermal dust continuum emission from two disks in multiple systems, the disks around UX Tau A and AS 205 A. These disks were detected at both 0.88 mm and 7.3 mm (UX Tau A) and at 0.88, 1.4, 8.0, and 9.8 mm (AS 205 A). The observations of these sources at centimeter-wavelengths represent the first detections of the dust continuum emission at these bands. The submillimeter-radio spectra of these sources provide clear evidence that the continuum emission is dominated by thermal greybody emission from the dusty disks, and not from stellar processes. While the emission from the AS 205 A disk is notably more compact at centimeter wavelengths than at submillimeter wavelengths, no such effect is observed for the UX Tau A disk. By fitting the data with parametric models, we estimated the radial profiles of optical depth at each wavelength. In doing so, we were able to quantify the shape of the local opacity spectrum for each disk. Quantified as a radial profile of the opacity spectral index, $\beta(r)$, we find that the disk of AS 205 A varies strikingly from $\beta \approx 0.5$ at $\lesssim 20$ AU to $\beta \gtrsim 1.7$ at $\sim 40 - 60$ AU, while that for UX Tau A is consistent with a flat radial profile.

The derivation of the spectral shape of the optical depth profile allows us to constrain the radial evolution of the size distribution of disk solids. Our observations of AS 205 and UX Tau add to the small, but growing, number of disks that have been resolved at sufficiently separated radio/millimeter bands to allow this kind of analysis. Previous observations of AS 209 (Pérez et al. 2012) and UZ Tau E (Chapter 3) have suggested that the radial evolution of disk solids is a generic feature.

Our observations suggest that any variation, if present, is small, and the data are

consistent with a constant κ_ν across the extent of the UX Tau A dust disk. This is at variance both with models of grain growth (e.g., Birnstiel et al. 2012b), and with observations of other disks. The likely reason for the difference is the relative size of the emission region in the disk. The UX Tau A disk is depleted of large mm-sized grains inward of $\sim$ 25 AU, and is only detected out to a radial distance of $\sim$ 50 AU at mm/cm bands. Such a small emission region does not lend itself to detection of small radial gradients with our data. Moreover, we still do not have a clear understanding of what process creates the central millimeter continuum cavity in transition disks like UX Tau A. Suggestions include grain growth to sizes large enough to be undetectable by millimeter instruments (but see Birnstiel et al. 2012a) and clearing by planetary-mass companions interior to the cavity. Dynamical effects produced by companions have not been included in models of grain growth, although there are hints that it is destructive to grains (Zsom et al. 2011). Such a scenario may be consistent both with our observations and models of grain growth. For instance, in the absence of a companion, internal disk processes (radial drift, fragmentation) may create top-heavy grain size distributions preferentially in the inner disk. The action of an (unseen) planetary companion could preferentially destroy the large grains in the inner disk, leaving behind no signature of the grain evolution processes internal to the disk.

The detection of the strong variation in the opacity spectral index in the AS 205 A disk is in line with both theory and the relatively few other disks that have been resolved at sufficiently many mm/cm bands. The variation in the opacity spectral index suggests that the size distribution of disk solids evolves with radius. To cast our observational results into the language of grain sizes, we follow the approach of both Pérez et al. (2012) and Chapter 3. We select a fixed composition for the dust grains, which are assumed

to be (by volume) 8% olivine, 30% carbonaceous materials, and 62% water ice (the optical constants for each of the materials can be found in Semenov et al. 2003, Zubko et al. 1996, and Warren 1984). The Brueggeman mixing formula is used to compute the effective optical constants of the resulting aggregates from their individual constituents. These effective constants are then used to derive opacities for a population of dust grains with minimum size 10 nm and variable maximum size $a_{\rm max}$, assuming a power-law form in between,

$$n(a)da \propto a^{-p}da, \tag{4.7}$$

for $p \in \{3.0, 3.5\}$. The opacities are computed at each wavelength for which we have data and a grid of $a_{\rm max}$ values. Then, for each radius in the disk, we sample the posterior distributions of $\tau_\nu(r)$ at each wavelength, giving us $\{\tau_{0.88{\rm mm}}, \tau_{1.4{\rm mm}}, \tau_{8.0{\rm mm}}, \tau_{9.8{\rm mm}}\}$. Because $\tau_\nu = \Sigma_{\rm dust}\kappa_\nu$, we then fit for both the dust surface density and for $a_{\rm max}$ by directly tabulating the quantities

$$\chi^2 = \sum_{\rm wavelengths} \left(\tau_\nu(r) - \Sigma_{\rm dust}\kappa_\nu(a_{\rm max})\right)^2 \tag{4.8}$$

where $\kappa_\nu(a_{\rm max})$ is the tabulated value of the opacity at the appropriate observing wavelength corresponding to a maximum grain size of $a_{\rm max}$. We then find the parameters $\{\Sigma_{\rm dust}, a_{\rm max}\}$ that minimize this value.

We show the constraints on both $\Sigma_{\rm dust}$ and $a_{\rm max}$ for the AS 205 A disk for each value of p in Figure 4.14. In both cases, our results suggest that the maximum dust grain size varies as a function of radius, from ~ 200 μm in the outer disk to at either a few mm in the inner regions of the disk (for $p = 3.0$) or a few cm (for $p = 3.5$). Also plotted are the predictions from analytic prescriptions based on the models of Birnstiel et al. (2012b), in the cases where grain growth is limited by radial drift (*red*) and turbulent fragmentation

(*blue*). These models assume a constant gas-to-dust ratio of 100, a turbulent viscosity parameter of $\alpha = 0.01$, and a fragmentation velocity of $u_f = 10$ m/s, appropriate for icy dust particles in the outer regions of the disk probed by our observations. The derived constraints on $a_{\rm max}$ do not lend themselves to agreement with predictions for growth limited by either physical effect considered here, assuming our model parameters: they lie in between the predictions. This is in contast to the cases of UZ Tau (Chapter 3) and AS 209 (Pérez et al. 2012), in which the same choices for parameter values led to agreement between the derived values of $a_{\rm max}$ and the predictions for growth limited by radial drift. It should be noted, however, that these choices of parameters may be different for each individual system.

With the growing consensus that dust grain properties should and do differ with radius in circumstellar disks, it is only a matter of time before dozens of examples of sources exhibiting this behavior are mapped in the millimeter and centimeter bands. At the present time, we are at the infancy of the study of the variation of the dust properties in disks. However, combined with the wealth of information that can be gathered about the properties of the gas from millimeter line transitions, these observations, particularly with the Atacama Large Millimeter Array and the Very Large Array, will serve as a crucial calibration tool for models of grain growth across circumstellar disks.

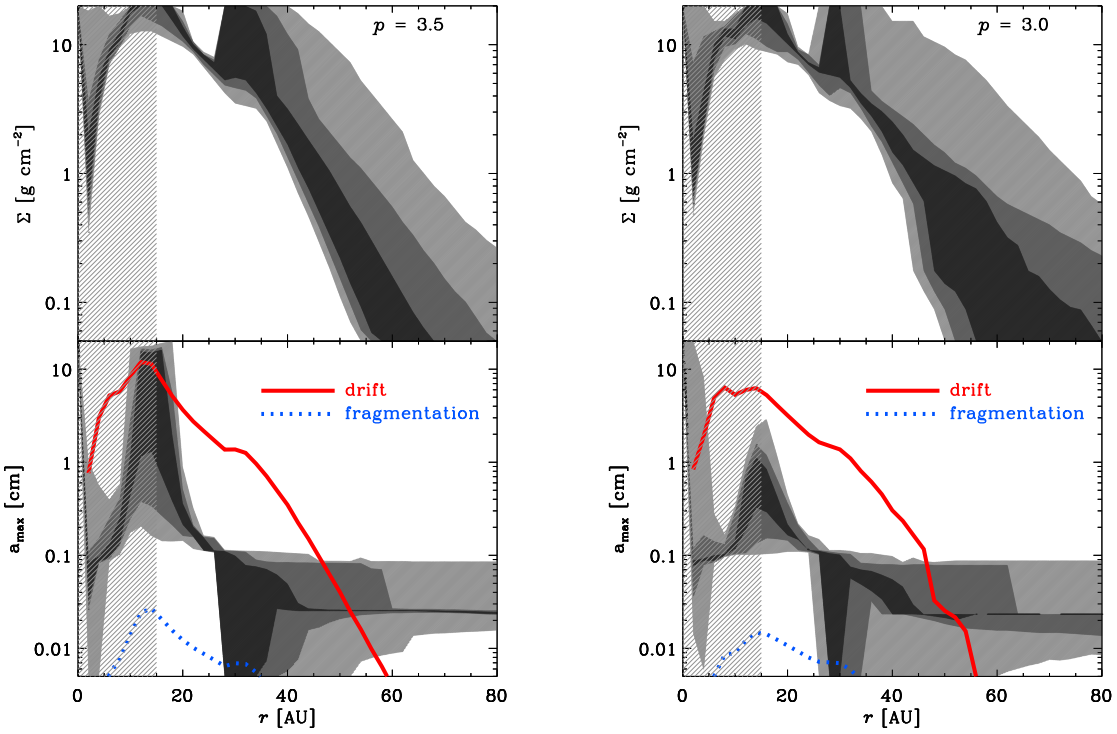

Figure 4.14: The inferred radial distributions of the dust surface densities (*top*) and maximum particle sizes (*bottom*) for model *Scenario B* and particle size distributions with power-law indices $p = 3.5$ (*left*) and 3.0 (*right*) for the AS 205 A dust disk. The shading and hatched regions are as in Fig. 4.12. The red and blue curves represent simple predictions for the particle evolution dominated by radial drift and turbulent fragmentation, respectively, for fiducial disk parameters (see text; Birnstiel et al. 2012b).

4.6 Summary

We have presented sensitive interferometric observations of the continuum emission from the disks of two multiple systems, AS 205 and UX Tau, at wavelengths of 0.88, 1.4, 8.0 and 9.9 mm and 0.88 and 7.3 mm, respectively, as part of the "Disks@EVLA" key project. By using simple parametric models of the disk structure, we have used these data to quantify the degree to which particle growth has occurred throughout the disk. The key conclusions from this work are as follows:

- Both the circumprimary and circumsecondary disk in the AS 205 system and the transition disk around UX Tau A exhibit thermal greybody emission that dominate the spatially-integrated spectra out to a wavelength of $\sim$1 cm, indicating significant grain evolution has occured in these disks, as compared to the grains of the interstellar medium.
- The continuum emission extent of the AS 205 A disk is resolved at all wavelengths and is found to be anti-correlated with wavelength. The structure of the UX Tau A disk shows no evidence for significant differences with wavelength.
- Through the use of parametric modeling, we measure the radial profiles of the optical depth at each wavelength and the profile of the slope of the opacity spectrum (i.e., the disk millimeter/radio colors) throughout both the AS 205 A and UX Tau A disks. We find that the emission becomes substantially redder with proximity to the host star for the AS 205 A disk, while there is no such color variation in the UX Tau A disk.
- We compare our results for the AS 205 A disk to calculations of opacity spectra; this comparison suggests that the maximum grain size varies by a factor of $\gtrsim 10$

throughout the disk. By using parameters describing the disk turbulence and dust properties, we are not able to decide on a dominant mechanism for what sets the particle size distribution, suggesting that these parameters vary from disk to disk.

Chapter 5

Concluding remarks

Dynamical effects from stellar companions represent a very common complication to the standard picture of planet formation. Theoretical arguments suggest that planet formation should be more difficult for a disk tidally affected by a companion as compared to a disk without a companion. The reasons are two-fold: (1) tidal forces tend to strip away material from the disk, leaving less mass and less time for planet formation (e.g., Artymowicz & Lubow 1994), and (2) the grain growth properties could be negatively impacted by the effect of the companion on the disk gas velocities (Zsom et al. 2011). Despite this, the question of how multiplicity affects disk structure and how disk solids evolve in the gaseous environment has received relatively little observational attention. This seems largely to be due to the high sensitivity and angular resolution required to perform resolved imaging studies of the disks in these systems. The development of sensitive, long-baseline millimeter/radio interferometers in the last few years has represented a huge breakthrough in the study of protoplanetary disks in general, and of protoplanetary disks in multiples in particular.

In this thesis, we have used these interferometers to study disks in multiple systems and found that, while companions do play a clear role in determining masses and lifetimes, their role in assisting or inhibiting grain growth is less clear. In the first part of the thesis (Chapter 2), we reported a large SMA survey of multiples in the Taurus-Auriga star forming region and examined the role stellar companions play in determining bulk disk properties, such as their masses/luminosities, radii, and lifetimes. We found results qualitatively consistent with theory: closer companions seem to strip more material away from disks. The high angular resolution of the survey has allowed us to go beyond what had been done previously. We conducted the first component resolved census of disks in these systems, and we found that of the individual components of multiples, less massive stars are likely to have less mass in disks. We then connected this fact to the known population of planets in multiples, which we suggested may reflect this disparity. Furthermore, by combining our results with those from previous surveys we were able to argue that the presence of a stellar companion is as important for setting the disk lifetime *as all other effects, environmental and intrinsic to the disk, combined*. Finally, we tested, for the first time, the quantitative theory of tidal truncation of circumstellar disks, and found thoroughly mixed results.

In the second part of this thesis, Chapters 3 and 4, we examined the detailed process of grain growth to centimeter sizes via spatially resolved observations. Through extensive modeling of multi-band interferometric data, we found significant spatial variation in the millimeter colors of the UZ Tau E circumbinary disk as well as the circumstellar disk AS 205 A. We interpreted the variation in the millimeter colors as reflecting an underlying variation in the size distribution of dust particles. By fitting the resolved millimeter/centimeter spectrum, we found evidence for a variation by up to a factor of

~ 10 in the sizes of solids throughout the disk, and we interpreted this in the light of models of radial transport, growth, and destruction of disk solids. A similar exercise applied to the UX Tau A transition disk uncovered no evidence for spatial variations in the grain size distribution.

These observations allow a first examination of the impact stellar companions have on the extent of grain growth in circumstellar disks. Figure 5.1 shows the profiles of the opacity spectral index β for the three disks discussed in this thesis, UZ Tau E, AS 205 A, and UX Tau A, as well as the profile for the disk around the isolated star AS 209 (Pérez et al. 2012). With the exception of the UX Tau A disk, each profile is broadly similar. Though the small sample and uncertain true stellar separation of the members of this sample prevent a definitive statement, the profiles suggest that multiplicity may *not* play a fundamental role in the determination of grain sizes in circumstellar disks.

The observations that have allowed us to draw the conclusions about these disks have only recently become possible with the advent of long-baseline, sensitive interferometers operating at millimeter and radio bands. These instruments, particularly the upgraded Karl G. Jansky Very Large Array and the Atacama Large Millimeter/submillimeter Array, will deliver observations of both the gas and dust content of protoplanetary disks with fantastic resolution and sensitivity in the future. To conclude this thesis, we comment on several potential avenues for investigation related to those presented here.

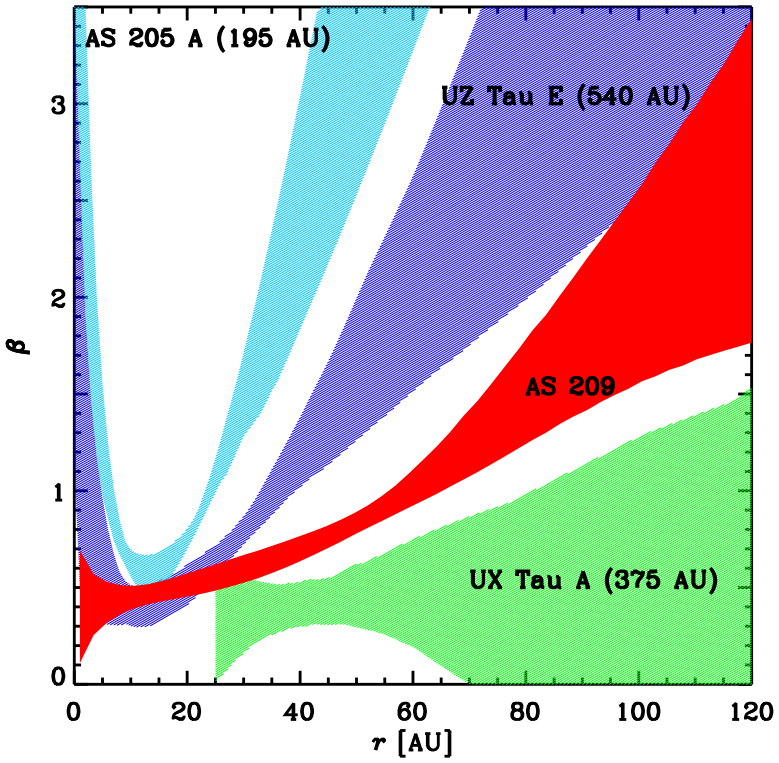

Figure 5.1: Comparisons of the 95% confidence regions for the radial profiles of the opacity spectral index β for the three disks discussed in this thesis, UZ Tau (Chapter 3), AS 205 A (Chapter 4), and UX Tau A (Chapter 4), as well as that for the isolated star AS 209 (from Pérez et al. 2012). For each system, the projected physical separation of the nearest companion (assuming $d \approx 145$ pc for Taurus and $d \approx 125$ pc for Ophiuchus) is indicated.

5.1 Future work

Grain Growth and Disk Physics in Tight Binaries

The huge increases in sensitivity and angular resolution at (sub)millimeter bands afforded by ALMA will be staggering. One of the immediate and most basic benefits of this combination of array characteristics as regards multiples is the opportunity to study close separation systems. Such systems – with projected separations down to 5 AU – offer a number exciting avenues for research, as they are wide enough to be spatially resolved by ALMA and yet close enough to have constrained orbits. Because the properties of planets in multiples seem to vary with separation (Duchêne 2010; Roell et al. 2012), and because it has been suggested that close companions preferentially inhibit grain growth (Zsom et al. 2011), multi-band imaging surveys of large samples of young multiples still retaining their disks seem prudent to determine robustly how multiplicity impacts grain growth to centimeter sizes. Surveys of tight multiples will allow us to answer the question first addressed in this thesis – whether multiplicity affects grain growth to cm sizes – but in a more interesting and, perhaps, relevant separation regime.

Such a survey will also be useful to address basic questions about the truncation of disks. In Chapter 2, we were obligated to test truncation models in a statistical sense. Testing these theories with observations of close ($a \lesssim 50$ AU) binaries with both constrained orbits and known circumstellar dust emission (e.g. FS Tau, DF Tau, FO Tau; Tamazian et al. 2002) is of particular interest. This kind of observation would allow a more precise test of truncation theory than possible before.

Second generation planet formation

While young stars inherit their disks from their natal environment, older binaries undergoing mass transfer can also have disks. Observations of planets orbiting cataclysmic variable stars suggest that these planets *may* form *in situ* (e.g., NN Ser; Beuermann et al. 2010). Mass transfer from an evolved star to a stellar companion through a wind can effectively establish a mass reservoir around a main-sequence star or white dwarf. This channel has recently been investigated by Perets & Kenyon (2012). In their theoretical work, they found that the accretor in these systems could retain a disk mass reservoir similar to that of protoplanetary disks ($\lesssim 2 \times 10^{-3}$ $M_\odot$) for $\sim 10^{5-6}$ years, comparable to the lifetimes of protoplanetary disks. Natural questions to ask are do these disks exist, and, if so, do they differ from 'true' protoplanetary disks in their grain growth properties? Observations with ALMA may resolve this question in the next few years.

References

Abt, H. A., & Levy, S. G. 1976, ApJS, 30, 273

Adams, F. C., Lada, C. J., & Shu, F. H. 1988, ApJ, 326, 865

Akeson, R. L., Koerner, D. W., & Jensen, E. L. N. 1998, ApJ, 505, 358

Akeson, R. L., Rice, W. K. M., Boden, A. F., et al. 2007, ApJ, 670, 1240

Altenhoff, W. J., Thum, C., & Wendker, H. J. 1994, A&A, 281, 161

Ambartsumian, V. A. 1937, AZh, 14, 207

Ambartsumian, V. A. 1957, in IAU Symposium, Vol. 3, Non-stable stars, ed. G. H. Herbig, 177–185

Andre, P., & Montmerle, T. 1994, ApJ, 420, 837

Andrews, S. M., Czekala, I., Wilner, D. J., et al. 2010, ApJ, 710, 462

Andrews, S. M., & Williams, J. P. 2005, ApJ, 631, 1134

—. 2007a, ApJ, 671, 1800

—. 2007b, ApJ, 659, 705

Andrews, S. M., Wilner, D. J., Espaillat, C., et al. 2011, ApJ, 732, 42

Andrews, S. M., Wilner, D. J., Hughes, A. M., Qi, C., & Dullemond, C. P. 2009, ApJ, 700, 1502

Andrews, S. M., Wilner, D. J., Hughes, A. M., et al. 2012, ApJ, 744, 162

Artymowicz, P., & Lubow, S. H. 1994, ApJ, 421, 651

Bai, X.-N. 2011, ApJ, 739, 50

Balbus, S. A., & Hawley, J. F. 1991, ApJ, 376, 214

Banzatti, A., Testi, L., Isella, A., et al. 2011, A&A, 525, A12

Baraffe, I., Chabrier, G., Allard, F., & Hauschildt, P. H. 1998, A&A, 337, 403

Barnard, E. E. 1895, Astronomische Nachrichten, 138, 211

Batalha, N. M., Rowe, J. F., Bryson, S. T., et al. 2013, ApJS, 204, 24

Bate, M. R., & Bonnell, I. A. 1997, MNRAS, 285, 33

Beall, J. H. 1987, ApJ, 316, 227

Beck, T. L. 2007, AJ, 133, 1673

Beckwith, S., Sargent, A. I., Scoville, N. Z., et al. 1986, ApJ, 309, 755

Beckwith, S., Skrutskie, M. F., Zuckerman, B., & Dyck, H. M. 1984, ApJ, 287, 793

Beckwith, S. V. W., & Sargent, A. I. 1991, ApJ, 381, 250

Beckwith, S. V. W., Sargent, A. I., Chini, R. S., & Guesten, R. 1990, AJ, 99, 924

Beuermann, K., Hessman, F. V., Dreizler, S., et al. 2010, A&A, 521, L60

Beust, H., & Dutrey, A. 2005, A&A, 439, 585

Bianchi, S., Gonçalves, J., Albrecht, M., et al. 2003, A&A, 399, L43

Bieging, J. H., Cohen, M., & Schwartz, P. R. 1984, ApJ, 282, 699

Birnstiel, T., Andrews, S. M., & Ercolano, B. 2012a, A&A, 544, A79

Birnstiel, T., Dullemond, C. P., & Brauer, F. 2009, A&A, 503, L5

—. 2010a, A&A, 513, A79

Birnstiel, T., Dullemond, C. P., & Pinilla, P. 2013, A&A, 550, L8

Birnstiel, T., Klahr, H., & Ercolano, B. 2012b, A&A, 539, A148

Birnstiel, T., Ormel, C. W., & Dullemond, C. P. 2011, A&A, 525, A11

Birnstiel, T., Ricci, L., Trotta, F., et al. 2010b, A&A, 516, L14

Blum, J., & Wurm, G. 2008, ARA&A, 46, 21

Boden, A. F., Torres, G., Sargent, A. I., et al. 2007, ApJ, 670, 1214

Bonavita, M., & Desidera, S. 2007, A&A, 468, 721

Bonnell, I. A., & Bate, M. R. 1994, MNRAS, 269, L45

Borucki, W. J., Koch, D. G., Basri, G., et al. 2011, ApJ, 728, 117

Brauer, F., Dullemond, C. P., & Henning, T. 2008a, A&A, 480, 859

Brauer, F., Henning, T., & Dullemond, C. P. 2008b, A&A, 487, L1

Carpenter, J. M., Wolf, S., Schreyer, K., Launhardt, R., & Henning, T. 2005, AJ, 129, 1049

Carrasco-González, C., Rodríguez, L. F., Anglada, G., & Curiel, S. 2009, ApJ, 693, L86

Chiang, E., Phillips, R. B., & Lonsdale, C. J. 1996, AJ, 111, 355

Chiang, E. I., & Goldreich, P. 1997, ApJ, 490, 368

Cieza, L. A., Padgett, D. L., Allen, L. E., et al. 2009, ApJ, 696, L84

Clarke, C. J., Gendrin, A., & Sotomayor, M. 2001, MNRAS, 328, 485

Cohen, M. 1974, MNRAS, 169, 257

Cohen, M., & Kuhi, L. V. 1979, ApJS, 41, 743

Correia, S., Zinnecker, H., Ratzka, T., & Sterzik, M. F. 2006, A&A, 459, 909

Daemgen, S., Correia, S., & Petr-Gotzens, M. G. 2012, A&A, 540, A46

Daemgen, S., Petr-Gotzens, M. G., Correia, S., et al. 2013, A&A, 554, A43

D'Alessio, P., Calvet, N., & Hartmann, L. 2001, ApJ, 553, 321

D'Alessio, P., Calvet, N., Hartmann, L., Franco-Hernández, R., & Servín, H. 2006, ApJ, 638, 314

de Geus, E. J., de Zeeuw, P. T., & Lub, J. 1989, A&A, 216, 44

Desidera, S., & Barbieri, M. 2007, A&A, 462, 345

Desidera, S., Carolo, E., Gratton, R., et al. 2011, A&A, 533, A90

Dittrich, K., Klahr, H., & Johansen, A. 2013, ApJ, 763, 117

Dominik, C., & Tielens, A. G. G. M. 1997, ApJ, 480, 647

Doyle, L. R., Carter, J. A., Fabrycky, D. C., et al. 2011, Science, 333, 1602

Draine, B. T. 2006, ApJ, 636, 1114

Duchêne, G. 2010, ApJ, 709, L114

Duchêne, G., Beust, H., Adjali, F., Konopacky, Q. M., & Ghez, A. M. 2006, A&A, 457, L9

Duchêne, G., Delgado-Donate, E., Haisch, Jr., K. E., Loinard, L., & Rodríguez, L. F. 2007, Protostars and Planets V, 379

Duchêne, G., Ghez, A. M., McCabe, C., & Weinberger, A. J. 2003a, ApJ, 592, 288

Duchêne, G., Ménard, F., Stapelfeldt, K., & Duvert, G. 2003b, A&A, 400, 559

Duchêne, G., McCabe, C., Pinte, C., et al. 2010, ApJ, 712, 112

Dullemond, C. P., & Dominik, C. 2005, A&A, 434, 971

Dupuy, T. J., & Liu, M. C. 2011, ApJ, 733, 122

Duquennoy, A., & Mayor, M. 1991, A&A, 248, 485

Dutrey, A., Guilloteau, S., Duvert, G., et al. 1996, A&A, 309, 493

Eggenberger, A., Udry, S., Chauvin, G., et al. 2007, A&A, 474, 273

Eisner, J. A., Hillenbrand, L. A., White, R. J., Akeson, R. L., & Sargent, A. I. 2005, ApJ, 623, 952

Elias, J. H. 1978, ApJ, 224, 453

Espaillat, C., Calvet, N., D'Alessio, P., et al. 2007, ApJ, 670, L135

Feigelson, E. D., & Montmerle, T. 1985, ApJ, 289, L19

Feigelson, E. D., & Nelson, P. I. 1985, ApJ, 293, 192

Finkbeiner, D. P., Davis, M., & Schlegel, D. J. 1999, ApJ, 524, 867

Fischer, D. A., & Marcy, G. W. 1992, ApJ, 396, 178

Flock, M., Henning, T., & Klahr, H. 2012, ApJ, 761, 95

Foreman-Mackey, D., Hogg, D. W., Lang, D., & Goodman, J. 2013, PASP, 125, 306

Ghez, A. M., Neugebauer, G., & Matthews, K. 1993, AJ, 106, 2005

Goldreich, P., & Tremaine, S. 1979, ApJ, 233, 857

—. 1980, ApJ, 241, 425

Goldsmith, P. F., Bergin, E. A., & Lis, D. C. 1997, ApJ, 491, 615

Goodman, J., & Weare, J. 2010, Commun. Appl. Math. Comput. Sci., 5, 65

Grasdalen, G. L., Strom, K. M., & Strom, S. E. 1973, ApJ, 184, L53

Grasdalen, G. L., Strom, S. E., Strom, K. M., et al. 1984, ApJ, 283, L57

Greene, T. P., Wilking, B. A., Andre, P., Young, E. T., & Lada, C. J. 1994, ApJ, 434, 614

Guilloteau, S., Dutrey, A., Piétu, V., & Boehler, Y. 2011, A&A, 529, A105

Guilloteau, S., Dutrey, A., & Simon, M. 1999, A&A, 348, 570

Gullbring, E., Hartmann, L., Briceno, C., & Calvet, N. 1998, ApJ, 492, 323

Güttler, C., Blum, J., Zsom, A., Ormel, C. W., & Dullemond, C. P. 2010, A&A, 513, A56

Harris, R. J., Andrews, S. M., Wilner, D. J., & Kraus, A. L. 2012, ApJ, 751, 115

Hartmann, L., Calvet, N., Gullbring, E., & D'Alessio, P. 1998, ApJ, 495, 385

Henning, T., Michel, B., & Stognienko, R. 1995, Planet. Space Sci., 43, 1333

Henning, T., & Stognienko, R. 1996, A&A, 311, 291

Herbig, G. H. 1950, ApJ, 111, 15

Herbig, G. H. 1957, in IAU Symposium, Vol. 3, Non-stable stars, ed. G. H. Herbig, 3

—. 1962, Advances in Astronomy and Astrophysics, 1, 47

Herbig, G. H., & Bell, K. R. 1988, Third Catalog of Emission-Line Stars of the Orion Population : 3 : 1988

Hildebrand, R. H. 1983, QJRAS, 24, 267

Ho, P. T. P., Moran, J. M., & Lo, K. Y. 2004, ApJ, 616, L1

Hughes, A. M., Wilner, D. J., Andrews, S. M., Qi, C., & Hogerheijde, M. R. 2011, ApJ, 727, 85

Hughes, A. M., Wilner, D. J., Qi, C., & Hogerheijde, M. R. 2008, ApJ, 678, 1119

Isella, A., Carpenter, J. M., & Sargent, A. I. 2009, ApJ, 701, 260

—. 2010, ApJ, 714, 1746

Itoh, Y., Hayashi, M., Tamura, M., et al. 2005, ApJ, 620, 984

Jensen, E. L. N., & Akeson, R. L. 2003, ApJ, 584, 875

Jensen, E. L. N., Dhital, S., Stassun, K. G., et al. 2007, AJ, 134, 241

Jensen, E. L. N., Koerner, D. W., & Mathieu, R. D. 1996a, AJ, 111, 2431

Jensen, E. L. N., & Mathieu, R. D. 1997, AJ, 114, 301

Jensen, E. L. N., Mathieu, R. D., Donar, A. X., & Dullighan, A. 2004, ApJ, 600, 789

Jensen, E. L. N., Mathieu, R. D., & Fuller, G. A. 1994, ApJ, 429, L29

—. 1996b, ApJ, 458, 312

Johansen, A., Klahr, H., & Henning, T. 2006, ApJ, 636, 1121

Johansen, A., Youdin, A., & Klahr, H. 2009, ApJ, 697, 1269

Jones, B. F., & Herbig, G. H. 1979, AJ, 84, 1872

Joy, A. H. 1945, ApJ, 102, 168

Joy, A. H., & van Biesbroeck, G. 1944, PASP, 56, 123

Kenyon, S. J., & Hartmann, L. 1987, ApJ, 323, 714

Kessler-Silacci, J. E., Hillenbrand, L. A., Blake, G. A., & Meyer, M. R. 2005, ApJ, 622, 404

Kitamura, Y., Momose, M., Yokogawa, S., et al. 2002, ApJ, 581, 357

Kley, W., & Lin, D. N. C. 1992, ApJ, 397, 600

Knott, G. 1891, The Observatory, 14, 97

Koerner, D. W., Sargent, A. I., & Beckwith, S. V. W. 1993, , 106, 2

Köhler, R., Ratzka, T., Herbst, T. M., & Kasper, M. 2008, A&A, 482, 929

Koresko, C. D. 2002, AJ, 124, 1082

Kóspál, Á., Salter, D. M., Hogerheijde, M. R., Moór, A., & Blake, G. A. 2011, A&A, 527, A96

Kraus, A. L., & Hillenbrand, L. A. 2009a, ApJ, 704, 531

—. 2009b, ApJ, 703, 1511

Kraus, A. L., Ireland, M. J., Hillenbrand, L. A., & Martinache, F. 2012, ApJ, 745, 19

Kraus, A. L., Ireland, M. J., Martinache, F., & Hillenbrand, L. A. 2011, ArXiv e-prints

Lada, C. J. 2006, ApJ, 640, L63

Lada, C. J., & Wilking, B. A. 1984, ApJ, 287, 610

Launhardt, R. 2004, in IAU Symposium, Vol. 221, Star Formation at High Angular Resolution, ed. M. G. Burton, R. Jayawardhana, & T. L. Bourke, 213

Leinert, C., Zinnecker, H., Weitzel, N., et al. 1993, A&A, 278, 129

Li, A., & Draine, B. T. 2001, ApJ, 554, 778

Lin, D. N. C., & Papaloizou, J. 1979a, MNRAS, 188, 191

—. 1979b, MNRAS, 186, 799

Loinard, L., Torres, R. M., Mioduszewski, A. J., et al. 2007, ApJ, 671, 546

Luhman, K. L., Allen, P. R., Espaillat, C., Hartmann, L., & Calvet, N. 2010, ApJS, 186, 111

Lynden-Bell, D., & Pringle, J. E. 1974, MNRAS, 168, 603

Mamajek, E. E., Meyer, M. R., Hinz, P. M., et al. 2004, ApJ, 612, 496

Mann, R. K., & Williams, J. P. 2010, ApJ, 725, 430

Mannings, V., & Emerson, J. P. 1994, MNRAS, 267, 361

Markwardt, C. B. 2009, in Astronomical Society of the Pacific Conference Series, Vol. 411, Astronomical Data Analysis Software and Systems XVIII, ed. D. A. Bohlender, D. Durand, & P. Dowler, 251

Massarotti, A., Latham, D. W., Torres, G., Brown, R. A., & Oppenheimer, B. D. 2005, AJ, 129, 2294

Massi, M., Forbrich, J., Menten, K. M., et al. 2006, A&A, 453, 959

Mathieu, R. D. 1994, ARA&A, 32, 465

Mathieu, R. D., Ghez, A. M., Jensen, E. L. N., & Simon, M. 2000, Protostars and Planets IV, 703

Mathieu, R. D., Martin, E. L., & Maguzzu, A. 1996, in Bulletin of the American Astronomical Society, Vol. 28, Bulletin of the American Astronomical Society, 920

Mathieu, R. D., Stassun, K., Basri, G., et al. 1997, AJ, 113, 1841

Mathis, J. S., Rumpl, W., & Nordsieck, K. H. 1977, ApJ, 217, 425

Mayor, M., Marmier, M., Lovis, C., et al. 2011, ArXiv e-prints

McCabe, C., Duchêne, G., Pinte, C., et al. 2011, ApJ, 727, 90

Melo, C. H. F., Covino, E., Alcalá, J. M., & Torres, G. 2001, A&A, 378, 898

Mendoza, E. E. 1966, ApJ, 143, 1010

—. 1968, ApJ, 151, 977

Miyake, K., & Nakagawa, Y. 1993, , 106, 20

Mizuno, H., Markiewicz, W. J., & Voelk, H. J. 1988, A&A, 195, 183

Moriarty-Schieven, G. H., Johnstone, D., Bally, J., & Jenness, T. 2006, ApJ, 645, 357

Motte, F., & André, P. 2001, A&A, 365, 440

Mugrauer, M., & Neuhäuser, R. 2009, A&A, 494, 373

Mundy, L. G., Looney, L. W., Erickson, W., et al. 1996, ApJ, 464, L169

Muzerolle, J., Hartmann, L., & Calvet, N. 1998, AJ, 116, 2965

Nagel, E., D'Alessio, P., Calvet, N., et al. 2010, ApJ, 708, 38

Natta, A., & Testi, L. 2004, in Astronomical Society of the Pacific Conference Series, Vol. 323, Star Formation in the Interstellar Medium: In Honor of David Hollenbach, ed. D. Johnstone, F. C. Adams, D. N. C. Lin, D. A. Neufeeld, & E. C. Ostriker, 279

Ochi, Y., Sugimoto, K., & Hanawa, T. 2005, ApJ, 623, 922

Okuzumi, S. 2009, ApJ, 698, 1122

Osterloh, M., & Beckwith, S. V. W. 1995, ApJ, 439, 288

Panagia, N., & Felli, M. 1975, A&A, 39, 1

Panić, O., Hogerheijde, M. R., Wilner, D., & Qi, C. 2009, A&A, 501, 269

Papaloizou, J., & Pringle, J. E. 1977, MNRAS, 181, 441

Pascucci, I., Apai, D., Hardegree-Ullman, E. E., et al. 2008, ApJ, 673, 477

Pascucci, I., Gorti, U., & Hollenbach, D. 2012, ApJ, 751, L42

Paszun, D., & Dominik, C. 2009, A&A, 507, 1023

Patience, J., Akeson, R. L., & Jensen, E. L. N. 2008, ApJ, 677, 616

Patience, J., White, R. J., Ghez, A. M., et al. 2002, ApJ, 581, 654

Pérez, L. M., Carpenter, J. M., & Chandler, C. J. 2012, ApJ, 751, 115

Pichardo, B., Sparke, L. S., & Aguilar, L. A. 2005, MNRAS, 359, 521

—. 2008, MNRAS, 391, 815

Piétu, V., Gueth, F., Hily-Blant, P., Schuster, K.-F., & Pety, J. 2011, A&A, 528, A81

Pinilla, P., Benisty, M., & Birnstiel, T. 2012a, A&A, 545, A81

Pinilla, P., Birnstiel, T., Ricci, L., et al. 2012b, A&A, 538, A114

Prato, L., Simon, M., Mazeh, T., Zucker, S., & McLean, I. S. 2002, ApJ, 579, L99

Pringle, J. E. 1981, ARA&A, 19, 137

Raghavan, D., Henry, T. J., Mason, B. D., et al. 2006, ApJ, 646, 523

Raghavan, D., McAlister, H. A., Henry, T. J., et al. 2010, ApJS, 190, 1

Reipurth, B., & Zinnecker, H. 1993, A&A, 278, 81

Ricci, L., Mann, R. K., Testi, L., et al. 2011a, A&A, 525, A81

Ricci, L., Testi, L., Natta, A., & Brooks, K. J. 2010a, A&A, 521, A66+

Ricci, L., Testi, L., Natta, A., et al. 2010b, A&A, 512, A15

Ricci, L., Testi, L., Williams, J. P., Mann, R. K., & Birnstiel, T. 2011b, ApJ, 739, L8

Richichi, A., Köhler, R., Woitas, J., & Leinert, C. 1999, A&A, 346, 501

Rodmann, J., Henning, T., Chandler, C. J., Mundy, L. G., & Wilner, D. J. 2006, A&A, 446, 211

Roell, T., Neuhäuser, R., Seifahrt, A., & Mugrauer, M. 2012, A&A, 542, A92

Rucinski, S. M. 1985, AJ, 90, 2321

Safronov, V. S. 1969, Evoliutsiia doplanetnogo oblaka.

Schaefer, G. H., Dutrey, A., Guilloteau, S., Simon, M., & White, R. J. 2009, ApJ, 701, 698

Schaefer, G. H., Simon, M., Beck, T. L., Nelan, E., & Prato, L. 2006, AJ, 132, 2618

Scholz, A., Jayawardhana, R., & Wood, K. 2006, ApJ, 645, 1498

Semenov, D., Henning, T., Helling, C., Ilgner, M., & Sedlmayr, E. 2003, A&A, 410, 611

Shakura, N. I., & Sunyaev, R. A. 1973, A&A, 24, 337

Shu, F. H., Adams, F. C., & Lizano, S. 1987, ARA&A, 25, 23

Simon, M., Chen, W. P., Howell, R. R., Benson, J. A., & Slowik, D. 1992, ApJ, 384, 212

Simon, M., Dutrey, A., & Guilloteau, S. 2000, ApJ, 545, 1034

Simon, M., & Prato, L. 1995, ApJ, 450, 824

Simon, M., Ghez, A. M., Leinert, C., et al. 1995, ApJ, 443, 625

Stognienko, R., Henning, T., & Ossenkopf, V. 1995, A&A, 296, 797

Strom, K. M., Strom, S. E., Edwards, S., Cabrit, S., & Skrutskie, M. F. 1989, AJ, 97, 1451

Tamazian, V. S., Docobo, J. A., White, R. J., & Woitas, J. 2002, ApJ, 578, 925

Tanaka, H., Takeuchi, T., & Ward, W. R. 2002, ApJ, 565, 1257

Taylor, G. B., Carilli, C. L., & Perley, R. A., eds. 1999, Astronomical Society of the Pacific Conference Series, Vol. 180, Synthesis Imaging in Radio Astronomy II

Tokovinin, A. A. 1998, Astronomy Letters, 24, 178

Torres, G. 1999, PASP, 111, 169

Torres, R. M., Loinard, L., Mioduszewski, A. J., & Rodríguez, L. F. 2007, ApJ, 671, 1813

—. 2009, ApJ, 698, 242

Uribe, A. L., Klahr, H., Flock, M., & Henning, T. 2011, ApJ, 736, 85

Urpin, V. A. 1984, Soviet Ast., 28, 50

Verrier, P. E., & Evans, N. W. 2008, MNRAS, 390, 1377

Vrba, F. J., Strom, K. M., Strom, S. E., & Grasdalen, G. L. 1975, ApJ, 197, 77

Ward, W. R. 1986, , 67, 164

Warren, S. G. 1984, Appl. Opt., 23, 1206

Weidenschilling, S. J. 1977, MNRAS, 180, 57

—. 1980, , 44, 172

Weidenschilling, S. J., & Cuzzi, J. N. 1993, in Protostars and Planets III, ed. E. H. Levy & J. I. Lunine, 1031–1060

Weintraub, D. A., Zuckerman, B., & Masson, C. R. 1989, ApJ, 344, 915

Welsh, W. F., Orosz, J. A., Carter, J. A., et al. 2012, Nature, 481, 475

Whipple, F. L. 1972, in From Plasma to Planet, ed. A. Elvius, 211

White, R. J., & Ghez, A. M. 2001, ApJ, 556, 265

White, R. J., Ghez, A. M., Reid, I. N., & Schultz, G. 1999, ApJ, 520, 811

White, R. J., & Hillenbrand, L. A. 2005, ApJ, 621, L65

Wilner, D. J., D'Alessio, P., Calvet, N., Claussen, M. J., & Hartmann, L. 2005, ApJ, 626, L109

Windmark, F., Birnstiel, T., Ormel, C. W., & Dullemond, C. P. 2012, A&A, 544, L16

Wurm, G., & Blum, J. 1998, , 132, 125

Xiang-Gruess, M., & Papaloizou, J. C. B. 2013, MNRAS, 431, 1320

Zahn, J.-P. 1977, A&A, 57, 383

Zahn, J.-P., & Bouchet, L. 1989, A&A, 223, 112

Zsom, A., Ormel, C. W., Güttler, C., Blum, J., & Dullemond, C. P. 2010, A&A, 513, A57

Zsom, A., Sándor, Z., & Dullemond, C. P. 2011, A&A, 527, A10+

Zubko, V. G., Mennella, V., Colangeli, L., & Bussoletti, E. 1996, MNRAS, 282, 1321